Distributed Control for Vision-based Convoying

by

Hien Khen Goi

A thesis submitted in conformity with the requirements
for the degree of Masters of Applied Science
Graduate Department of Electrical and Computer Engineering
University of Toronto

Abstract

Distributed Control for Vision-based Convoying

Hien Khen Goi

Masters of Applied Science

Graduate Department of Electrical and Computer Engineering

University of Toronto

2009

This thesis describes the design of a vision-based vehicle-following system that uses only on-board sensors to enable a convoy of follower vehicles to autonomously track the trajectory of a manually-driven lead vehicle. The tracking is done using the novel concept of a constant time delay, where a follower tracks the delayed trajectory of its leader. Two separate controllers, one linearized about a point ahead and the other linearized about a constant-velocity trajectory, were designed and tested in simulations and experiments. The experiments were conducted with full-sized military vehicles on a 1.3 km test track. Successful field trials with one follower for 10 laps and with two followers for 13.5 laps are presented.

Acknowledgements

First, I want to thank my co-supervisors: Professor Bruce Francis and Professor Tim Barfoot. Bruce, your attention to detail has helped significantly improve the clarity of my writing. Tim, your guidance throughout this thesis and especially during the first field trials has been invaluable to my development as an engineer. I am greatly indebted to you both.

I also want to thank Jared Giesbrecht and the technicians at Defence Research and Development Canada Suffield for all of their help in preparing the experimental vehicles and filming the field trials. Their expertise was crucial in getting the experiments to run smoothly. Finally, I want to thank my parents for their encouragement and support. It was their hard work and sacrifice that has enabled me to achieve my goals.

Contents

List of Tables

List of Figures

Chapter 1

Introduction

Motivating our research is a military situation in which a vehicle convoy traverses hostile territory to deliver supplies. Naturally, equipping every vehicle in the convoy with armour that will protect its occupants is expensive. To reduce the cost, autonomous unarmoured supply vehicles may be used, whereby each supply vehicle would autonomously follow the trajectory of its immediate leader. With this setup, the vehicle convoy would be comprised of autonomous unarmoured vehicles and manually-driven armoured vehicles. To follow its immediate leader, an autonomous vehicle can sometimes take advantage of a global positioning system (GPS), inter-vehicle communications, and/or lane markers/magnets. However, since the vehicle convoy is in hostile territory, GPS signals may be jammed, inter-vehicle communications may be intercepted, and the roads may be unstructured.

Based on this motivating example, we collaborated with Defence Research and Development Canada (DRDC) Suffield in the design and testing of a distributed control system to allow a convoy of full-sized autonomous vehicles with large inter-vehicle spacing to follow a manually-driven lead vehicle's trajectory without cutting corners on turns. To narrow the scope, we assumed all followers in the convoy are autonomous and focused our design for this scenario. DRDC Suffield provided the experimental vehicles, along

with the testing facility, while we designed the vehicle-following system that was implemented on each autonomous vehicle. The DRDC vehicles are MultiAgent Tactical Sentry (MATS) vehicles, and each MATS vehicle is equipped with a pan-tilt-zoom camera and a speed-and-steering control system. The camera measures the range and bearing to a specified target, and the speed-and-steering control system sets the vehicle's speed and steering based on commanded inputs. The MATS vehicle also has wheel encoders to measure the vehicle's current speed and steering. With the goal of implementing our system on the MATS vehicle, we formulated our problem based on the available sensors.

1.1 Problem Formulation

A vehicle convoy can be decomposed into identical leader-follower pairs, as shown in Figure 1.1. Since there are no inter-vehicle communications to relay the lead vehicle's

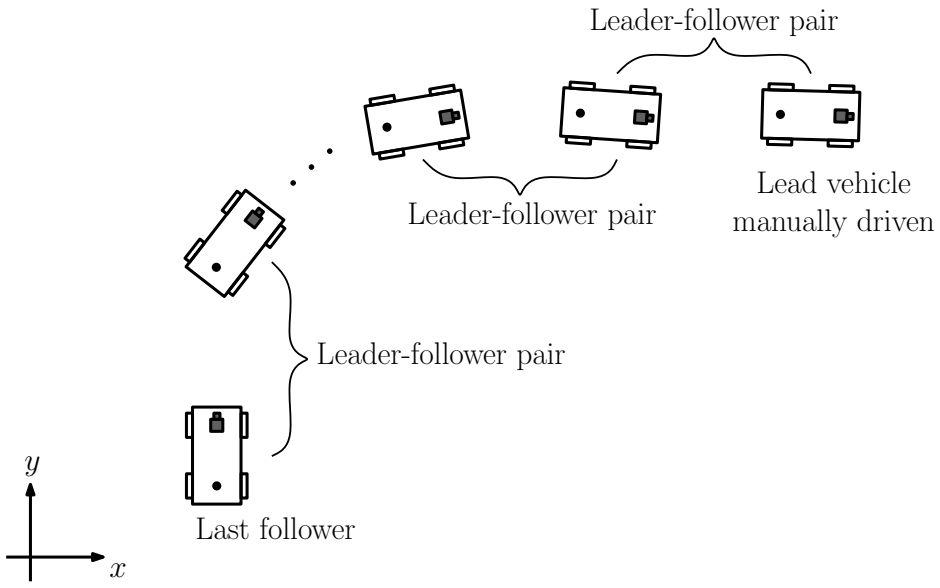

Figure 1.1: Vehicle convoy decomposed into identical leader-follower pairs.

position, the goal of an autonomous follower is to track the trajectory of its immediate leader. Focusing on one leader-follower pair, we have taken the novel approach of having the follower track the planar trajectory of its leader delayed by a constant time, τ, as

shown in Figure 1.2. Specifically, if $(x(t), y(t))$ is the position of the follower with respect to an inertial frame and $(x_0(t), y_0(t))$ is the position of the leader with respect to the same frame, then we want $(x(t), y(t))$ to track $(x_0(t-\tau), y_0(t-\tau))$. For brevity, we have defined the delayed leader position, $(x_0(t-\tau), y_0(t-\tau))$, as $(x_\mathrm{d}(t), y_\mathrm{d}(t))$. The novelty in our definition is that the tracking error for the follower is measured with respect to the leader's delayed position, while other definitions, e.g., *constant distance* and *constant headway*, measure the follower's tracking error with respect to the leader's current position.

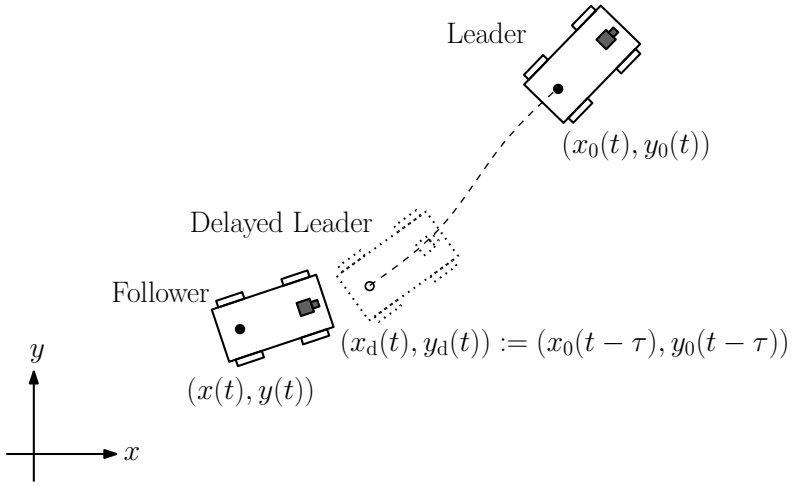

Figure 1.2: Leader, delayed leader, and follower in an inertial frame.

There are two main advantages to our approach: 1) tracking the delayed leader provides us with 'future' delayed-leader positions since we have measurements up to the leader's current position; and 2) the following distance varies based on the leader's speed. The first advantage allows the follower to track the leader's trajectory without having to directly measure the leader's speed or heading. Instead, the delayed leader's future positions are used to estimate its speed and heading. The second advantage naturally causes the following distance to be smaller when the leader slows down on difficult portions of the road, e.g., turns and rough terrain. The smaller following distance allows for more accurate measurements of the leader's position, which will help the tracking during those difficult portions.

1.2 Literature Review

For a follower vehicle to track its leader, a longitudinal spacing policy is required to separate the two vehicles. The most common spacing strategies are constant distance and constant headway. As the name suggests, the constant-distance policy implies that the inter-vehicle distance is constant. The policy's spacing error, ε, in 1-D, as defined by Swaroop and Hedrick [36], is

$$\varepsilon := x_0 - x - l,$$

where x_0 is the position of the leader, x is the position of the follower, and l is the desired constant following distance. In contrast, the spacing distance in the constant-headway policy is a function of the follower's speed, and the policy's spacing error, in 1-D, as defined by Swaroop and Rajagopal [37], is

$$\varepsilon := x_0 - x - hv,$$

where h is the constant headway time and v is the follower's speed. Note that a constant safety distance may also be added to the above equation to prevent the inter-vehicle spacing from being zero when the follower's speed is zero.

Once a spacing policy is chosen, different types of control systems on the follower may be used to track the leader. These systems can be categorized with respect to the reference frame used to estimate the leader's trajectory. The reference frame may be inertial (fixed to an initial position) or moving (implicitly with the follower). An inertial reference frame requires the follower to localize its current position relative to the reference point, while a moving reference frame does not.

1.2.1 Moving Reference Frame

When the vehicle-following system uses a moving reference frame, the reference frame for the leader's trajectory is implicitly attached to the follower. As a result, the system needs to interpolate the follower's trajectory to the leader. Such a system has been developed by the group from Texas A&M University (Kehtarnavaz et al. [21, 20, 22] and Griswold et al. [17]), who tested vehicle following on their autonomous vehicle, Binocular Autonomous Research Team (BART), which used a stereo camera to obtain the range and bearing to the leader. Experiments using heuristic control laws resulting in only small lateral deviations for speeds up to 8.9 m/s are reported in [21]. The experimental trials were performed on a test track that is approximately 1.5 km in length, and the desired following distance was set to 15 m. The experimental data in [21] is limited to two 5-minute trials and shows the range to the leader varying greatly from 7 m to 60 m. In [17] and [20], the heuristic control laws are replaced with a neural network controller and the experiments have a desired following distance of 21 m. The new controller seemed to have improved the longitudinal tracking as the range varied only from 7 m to 36 m. In [22], the group compares the neural network controller with a fuzzy logic controller and shows the latter works better in the presence of high noise; however, only simulation results are presented.

Fritz [13], Franke et al. [12], and Schneiderman et al. [33, 34] also present vehicle-following systems that used a moving reference frame and a camera to track the leader. Both Fritz and Franke et al. employed the constant-headway policy, used inter-vehicle communications to obtain the leader's speed and acceleration, and have commercial trucks as the testbed. Longitudinal tracking tests with speeds up to 20 m/s with tracking errors of less than 2 m are presented in [13]. Lateral tracking test results around a circular test track with an 80 m radius are also shown. The lateral errors in those tests were less than 0.3 m. However, the longitudinal experimental data shown is less than 200 s, and the length of the lateral tests is not given. Similarly, the experimental data

in [12] shows longitudinal errors of less than 1 m with vehicle speeds of up to 17 m/s, but the data is limited to 50 s and seems to suggest a straight test path. In contrast, Schneiderman et al. conducted long experimental trials with their military high-mobility multipurpose wheeled vehicle (HMMWV) to validate robustness. In [33], they report a top speed of 9.7 m/s with following distances of 5 m to 15 m. This performance is improved upon in [34] with a 33 km traverse and speeds of up to 21.8 m/s. However, only the steering was autonomous in their system, and the tracking errors in the experiments are not given.

An alternative to using a camera to detect the relative position of the leader is to use a laser scanner, which is employed by Papadimitriou et al. [32], Lu and Tomizuka [25, 26], and Wang et al. [43]. To test autonomous steering control, Papadimitriou et al. conducted low-speed experiments over short distances and report lateral errors that stayed under 0.13 m in [32] . Using the same test vehicle as Papadimitriou et al. [32], Lu and Tomizuka manually kept the follower's speed and inter-vehicle distance to be 8.9 m/s and 10 m, respectively, and report a maximum lateral deviation from the road centre of around 1 m in [25]. The maximum lateral error was improved to about 0.20 m when inter-vehicle communications were added to transmit the leader's deviation from the road centre, as reported in [26]. But, in both [25] and [26], the experimental data shown is only about 60 s. Dealing with robustness to system failure, Wang et al. [43] present two separate control systems for their vehicle's front and back wheels. Vehicle following was demonstrated in the presence of a failure from either system with an experiment that covered 270 m in 350 s. The desired following distance was 2.5 m, but the lateral tracking error is not given.

A known shortcoming of interpolating the leader's trajectory is that the follower may deviate from the leader's path [14]. This problem can be solved by storing the leader's trajectory, a process that requires the follower to have an inertial reference frame. Localizing the follower's position to the inertial frame is commonly done in two ways:

using on-board sensors, such as wheel encoders and a heading gyro, and using GPS.

1.2.2 Absolute Localization using On-board Sensors

Localization using on-board sensors is commonly done using dead reckoning, a method that has an unbounded accumulation of errors in the position estimates [5]. Despite the unbounded error growth, vehicle following is still possible as demonstrated by the vision-based vehicle-following systems of Benhimane et al. [2] and Daviet and Parent [7, 8]. Benhimane et al. conducted experiments on two small electric vehicles in which the follower tracked a virtual leader rigidly linked by a constant distance behind the actual leader. However, the experimental data shown is only 120 s and the maximum speed of the follower was only 1 m/s. Daviet and Parent also performed experiments on electric vehicles, but their vehicles traveled up to 10 m/s. The reported longitudinal and lateral tracking errors are impressive at under 0.3 m and 0.6 m, respectively, but the data shown is for only 30 s.

Another vehicle-following system that localized using dead reckoning is presented by Vasseur et al. [42]. The system used a laser scanner to measure the range and bearing to the leader. Based on these measurements, the follower was able to follow the leader on a 2 km traverse of flat roads at speeds of 8.3 m/s and a following distance of around 21 m. The maximum lateral error for the trip was 0.73 m. A different technique for localization using on-board sensors is visual odometry, which relies on detecting and matching features in the surrounding environment. This method is used by Avanzini et al. [1] in their experiments with two electric vehicles on a 250 m U-shaped path. With a desired following distance of 6 m and a leader speed of 1 m/s, the follower was able to maintain a distance that varied from 5.6 m to 6.8 m when using only visual odometry. This longitudinal error was improved to less than 0.1 m when a laser scanner was added to the leader to take measurements of the surrounding that were transmitted to the follower to calibrate image distortions in the visual odometry.

Although some of the above vehicle-following systems had impressive results, they did not store the leader's trajectory. As a result, there is a potential for large lateral errors if the following distance gets very large or if the roads have sharp turns. This potential problem is not an issue for the systems developed by Sukthankar [35] and Gehrig and Stein [14], as both systems store the leader's trajectory. In contrast to all of the previously-mentioned works, Sukthankar focused on vehicle following at night by designing a camera system that tracks illuminated tail lights. Using localization from dead reckoning and range and bearing measurements from the camera system, the leader's trajectory was calculated and stored. The vehicle-following system then tracked the leader's trajectory at a constant distance ahead of the follower's current position. Using a look-ahead distance of 15 m, the follower was able to track the leader along a city street at 8.9 m/s. However, the length of the test and the tracking errors are not given. Similarly, Gehrig and Stein advocated storing the leader's trajectory and tracking a constant distance ahead of the follower's position in their autonomous steering algorithm, control using trajectory (CUT). They conducted experiments on a circular path with and without CUT at speeds of 10 m/s and a following distance of 25 m. The resulting maximum lateral errors for the two experiments were 0.7 m and 1.4 m, respectively, but the experimental data shown seems to suggest that the experiments lasted only 15 s.

1.2.3 Absolute Localization using GPS

In contrast to using on-board sensors, localization using GPS does not suffer from an unbounded accumulation of errors. However, depending on the types of GPS and receivers used and on the signal strength, GPS accuracy may be in the metres [44], an accuracy level that is not suitable for vehicle following on roads that are only metres wide. This issue was not a problem for the group from the University of Clermont-Ferrand (Thuilot et al. [41] and Bom et al. [3, 4]), whose laser-scanner-equipped electric vehicles use real-time kinetic (RTK) GPS that has an accuracy of 0.02 m. In [41], they report experiments with

speeds of 1 m/s to 3.4 m/s along a 80 m straight path and speeds of 1 m/s to 2.3 m/s along a 80 m curved path. The longitudinal errors for the straight-path experiments had standard deviations of less than 0.044 m, and the data shown suggests the lateral errors stayed under 0.25 m during the turns in the curved-path experiments. Inter-vehicle communications were added to transmit the leader's position for the experiments presented in [3] and [4]. The experiment shown in [3] has a desired following distance of 8 m and vehicle speeds of around 1 m/s, and the follower was able to maintain the desired distance with an error of 0.007 ± 0.047 m (mean±standard deviation) during a 130 s test. The experiments shown in [4] also have vehicle speeds of 1 m/s and seem to be less than 190 s long.

To overcome the potential GPS inaccuracy, Ng et al. [30] and Jaczkowski [18] fuse GPS measurements with on-board sensor data in their vehicle-following systems. The system employed by Ng et al. was designed to track a virtual kinematic off-hooked trailer attached to the leader, and experiments were conducted with a follower equipped with a laser scanner on both paved and unpaved roads. An electric vehicle was used as the follower in the paved-road test, and a truck is was used as the follower in the unpaved-road test. In both cases, the vehicles speeds were around 6.9 m/s. Tracking errors are also presented; however, the method used to calculate the tracking error does not seem standard. On top of using GPS for localization, Jaczkowski also used a sensor suite to generate high-resolution local maps on both the leader and the follower. The leader would then send its maps, along with its position, to the follower to help in the trajectory tracking. Experiments were conducted with military vehicles on a 15.9 km road course and a 3.0 km cross-country course. On the road tests, the speeds varied from 8.3 m/s to 18.3 m/s and the desired following distance varied from 50 m to 150 m, while on the cross-country tests, the speed was 5.6 m/s and the desired distance varied from 50 m to 100 m. The resulting maximum lateral errors for the two sets of tests were 0.45 m and 7 m, respectively.

Similar to Jaczkowski [18], Davis et al. [9] present experiments with military vehicles on a long test track, a 19 km course consisting of paved and unpaved roads. In these experiments, the follower was equipped with two vehicle-following systems: one that tracks the leader based on only camera and radar measurements, and the other that uses GPS waypoints transmitted from the leader, along with measurements from the camera and a laser scanner. Although the second system was the default during sharp turns, it was used less than 1% of the time during the experiments. In total, 36 trial runs were conducted with the vehicle speeds varying from 5.6 m/s to 11.1 m/s on unpaved roads and from 11.1 m/s to 16.7 m/s on paved roads. The resulting lateral error was 0.81 ± 0.60 m, but the follower needed to be manually realigned back onto the course an average of 5.6 times during each trial.

1.3 Contributions of Thesis

As is evident from the literature review, there is a lack of reported research on fully autonomous vehicle following that has extensive experimental trials without using GPS, inter-vehicle communications, or road marker/magnets. Furthermore, to our knowledge, experiments with two autonomous followers using only on-board sensors have not been done before. When more than one follower is used, previous experiments have used GPS, inter-vehicle communications, and/or road markers/magnets, e.g., Kato et al. [19], Tan et al. [38], and Thorpe et al. [40].

This thesis has filled the above experimental gap as extensive experimental trials are conducted with one and two autonomous full-sized follower vehicles using only on-board sensors in a difficult test environment. In addition, the thesis contributes the novel concept of tracking a leader vehicle delayed by a constant time. This new approach creates a delayed leader and allows a unique technique of using past, present, and future position measurements to estimate the delayed leader's speed and heading. Two separate

controllers are also designed and compared in the context of tracking the delayed leader, and the results are detailed in the following chapters.

Chapter 2

System Architecture and Design

The development of our vehicle-following system involved the following stages:

1. Model the leader-follower pair scenario
2. Design the controller and observer for the system
3. Conduct simulations to validate the design, making refinements when necessary
4. Field test the vehicle-following system, making refinements when necessary

In this chapter, the first two stages are detailed. The last two stages are presented in Chapters 3 and 4, respectively.

The design goal is for a follower asymptotically track a constant-velocity delayed leader using the on-board sensors available on the MATS vehicles, i.e., camera and speed and steering sensors. Since DRDC Suffield had three MATS vehicles available at the time of this thesis, the system was required to work for a convoy of all three vehicles: one manually-driven lead vehicle and two autonomous followers. Based on the setup of the MATS vehicle, the block diagram for the vehicle-following system of an autonomous follower is shown in Figure 2.1, where the positions and heading are relative to an inertial frame. The follower's camera outputs the measured range, ρ_{m}, and measured bearing, ϕ_{m}, to the leader, and wheel encoders output the measured speed, v_{m}, and measured steering, γ_{m}, of the follower. These measurements are the inputs to the vehicle-following system,

which outputs the commanded speed, v_c, and commanded steering, γ_c into the follower. To design the vehicle-following system, a vehicle model is needed for the follower; this is examined in the next section.

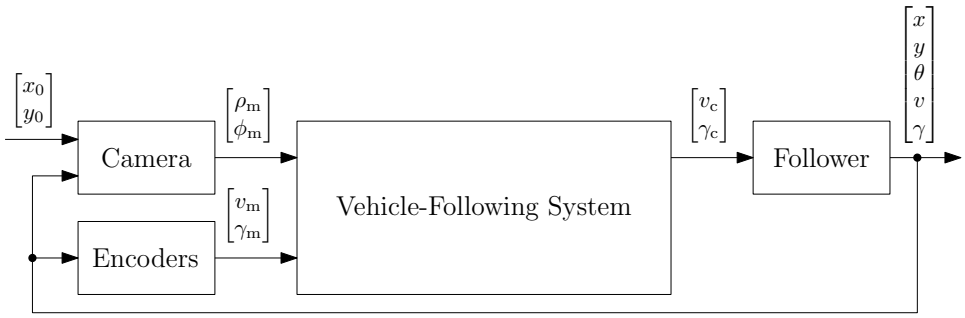

Figure 2.1: Block diagram of vehicle-following system of an autonomous follower.

2.1 Vehicle Model

For the follower vehicle's kinematics, the bicycle model, shown in Figure 2.2, is used. The states of the model are the position of the back wheel, (x, y), and its heading, θ.

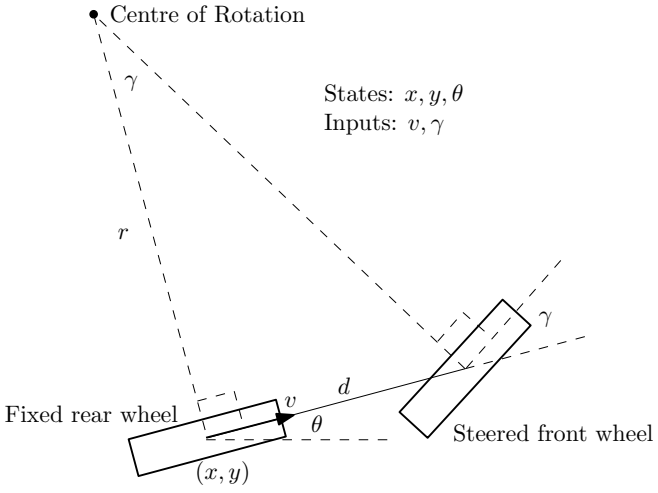

Figure 2.2: Bicycle model kinematics.

The inputs to the model are the translational speed of its rear wheel, v, and the turning angle of its front wheel, γ. The distance between the front and rear wheels is denoted by

d. Hence, the model equations are given by

$$\dot{x} = v\cos\theta$$

$$\dot{y} = v\sin\theta$$

$$\dot{\theta} = \frac{v}{d}\tan\gamma.$$

The equation for $\dot{\theta}$ can be seen by observing the right triangle formed by the centre of the rear wheel, the centre of rotation, and the centre of the front wheel in Figure 2.2. Noting that the turning radius is denoted by r,

$$\tan\gamma = \frac{d}{r}.$$

Since

$$\dot{\theta} = \frac{v}{r},$$

substituting for r gives

$$\dot{\theta} = \frac{v}{d}\tan\gamma.$$

Since the MATS vehicle has a speed-and-steering control system that sets the vehicle speed and steering according to the commanded inputs, we assumed a two-tier architecture for the vehicle model, shown in Figure 2.3a, where the speed-and-steering control system regulates the vehicle dynamics, while our vehicle-following system regulates the kinematics. With this architecture, the reference and output signals of the inner loop are the commanded speed and steering, (v_c, γ_c), and the actual speed and steering, (v, γ), respectively. Taking advantage of the regulated inner loop, we designed the vehicle-following system by treating the inner loop as a unity gain, as shown in Figure 2.3b. When we validated our design in simulation, we placed the inner loop back in using system-identification techniques, which is further explained in Chapter 3. At this point,

as a result of the unity-gain inner-loop assumption, the vehicle model for the follower is

$$\dot{x} = v_{\mathrm{c}} \cos\theta$$

$$\dot{y} = v_{\mathrm{c}} \sin\theta$$

$$\dot{\theta} = \frac{v_{\mathrm{c}}}{d} \tan\gamma_{\mathrm{c}}.$$

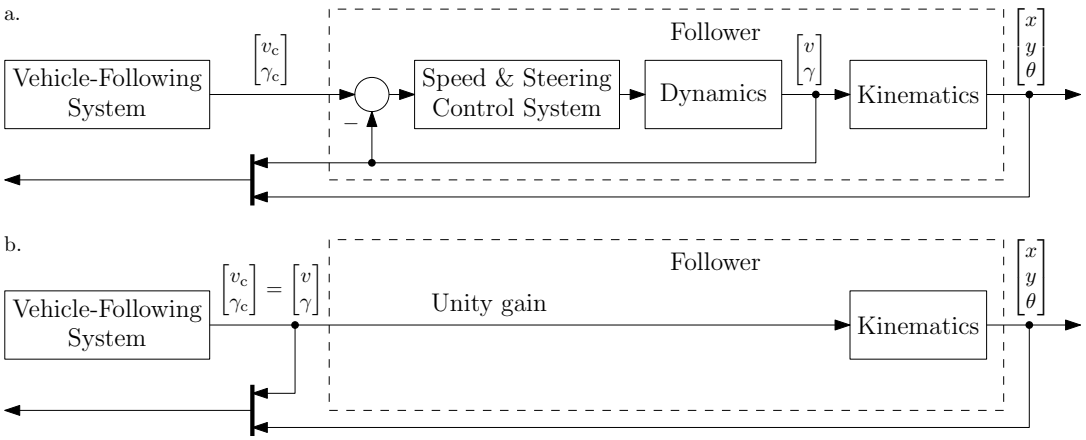

Figure 2.3: (a) Inner/outer loop architecture for the follower. (b) The outer-loop controller is designed by assuming the inner loop is a unity gain.

The vehicle-following system is still to be determined. However, it is obvious that control laws are required in the system. Based on the bicycle kinematics, we designed two separate controllers for the follower vehicle. The first controller is designed based on linearizing the bicycle model about a point ahead, an idea that can be found in [11] by Francis. The second controller is designed by linearizing about a constant-velocity trajectory. The next sections examine the two controller designs.

2.2 Point-ahead Controller

To derive the point-ahead controller, the following definitions are required:

$$\mathbf{z} := \begin{bmatrix} x \\ y \end{bmatrix}, \ \mathbf{r} := \begin{bmatrix} \cos\theta \\ \sin\theta \end{bmatrix}, \ \mathbf{J} := \begin{bmatrix} 0 & -1 \\ 1 & 0 \end{bmatrix},$$

where $\mathbf{z}$ is the position vector, $\mathbf{r}$ is the unit heading vector, and $\mathbf{J}$ is the rotation matrix of $\frac{\pi}{2}$. The point ahead, $\mathbf{p}$, is defined as

$$\mathbf{p} := \mathbf{z} + \kappa\mathbf{r},$$

where $\kappa > 0$ is the actual distance ahead in metres. Differentiating $\mathbf{p}$ yields

$$\dot{\mathbf{p}} = \dot{\mathbf{z}} + \kappa\dot{\mathbf{r}} = v_\mathrm{c}\mathbf{r} + \frac{\kappa v_\mathrm{c}}{d}\tan\gamma_\mathrm{c}\,\mathbf{J}\mathbf{r}.$$

Defining a new input, $\tilde{\mathbf{u}}$, as

$$\tilde{\mathbf{u}} := v_\mathrm{c}\mathbf{r} + \frac{\kappa v_\mathrm{c}}{d}\tan\gamma_\mathrm{c}\,\mathbf{J}\mathbf{r},$$

gives

$$\dot{\mathbf{p}} = \tilde{\mathbf{u}}.$$

Hence, the kinematic bicycle can be treated as an integrator, as shown by the linearized controller diagram in Figure 2.4. The bicycle model is now a two-input two-output decoupled system with integrators on the diagonal. Since the follower should asymptotically track its constant-velocity delayed leader with zero steady-state error, $\mathbf{p}_\mathrm{d}$ is nominally a ramp and proportional-integral (PI) control can be used with

$$\tilde{\mathbf{C}}(s) = \left(k_\mathrm{p} + \frac{k_\mathrm{i}}{s}\right)\mathbf{I}_2,$$

where $\mathbf{I}_2$ is the 2x2 identity matrix.

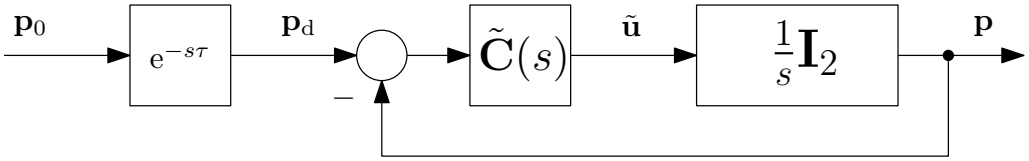

Figure 2.4: Linearized point-ahead controller diagram.

However, the real inputs into the bicycle model are v_c and γ_c. Thus, v_c and γ_c need to be computed from $\tilde{\mathbf{u}}$. By defining

$$\psi := \frac{\kappa v_c}{d} \tan \gamma_c$$

so that

$$\tilde{\mathbf{u}} = v_c \mathbf{r} + \psi \mathbf{J}\mathbf{r},$$

and using the fact that $\mathbf{r}$ and $\mathbf{J}\mathbf{r}$ are orthogonal vectors, v_c and ψ can be obtained immediately:

$$v_c = \mathbf{r}^{\mathrm{T}} \tilde{\mathbf{u}}$$
$$\psi = (\mathbf{J}\mathbf{r})^{\mathrm{T}} \tilde{\mathbf{u}}.$$

Subsequently, γ_c can be obtained from ψ and v_c through

$$\gamma_c = \tan^{-1}\left(\frac{\psi d}{\kappa v_c}\right).$$

Since γ_c is undefined for $v_c = 0$, a minimum positive v_c needs to be specified. Furthermore, because γ_c is a function of v_c, linearizing about a point ahead results in coupled speed and steering commands.

2.2.1 Setting Gains using Pole Placement

To pick the controller gains, we used pole placement. The rationale for using pole placement is that the pole locations in our system are directly related with the size of the gains; the further left the poles, the larger the gains. Thus, placing poles gives a systematic way of finding the largest set of gains that still yields stable follower behaviour. In our case, this largest set results in the best follower performance.

From Figure 2.4, the characteristic polynomial of the linearized system is

$$s^2 + k_\mathrm{p} s + k_\mathrm{i}. \tag{2.1}$$

To avoid oscillatory effects, the closed-loop poles are placed on the negative real axis. Let a and b be the pole locations; then, the desired characteristic polynomial is

$$(s - a)(s - b) = s^2 - (a + b)s + ab. \tag{2.2}$$

By comparing (2.1) with (2.2), algebraic equations for the gains in terms of the pole locations are obtained:

$$k_\mathrm{p} = -(a + b).$$

$$k_\mathrm{i} = ab$$

2.3 Decoupled Controller

Because the speed and steering commands in the point-ahead controller are coupled, tuning the gains to achieve good tracking behavior is not intuitive. As a result, we designed another controller that is decoupled in the longitudinal and lateral directions and, thus, is more intuitive to tune. The decoupled controller is designed by linearizing the bicycle model about a constant-velocity trajectory, which decouples the vehicle model

and allows the use of decoupled control laws. The derivation of the decoupled vehicle model begins with the definition of the longitudinal and lateral tracking errors, $(\varepsilon_1, \varepsilon_2)$:

$$\begin{bmatrix} \varepsilon_1 \\ \varepsilon_2 \end{bmatrix} := \begin{bmatrix} \cos\theta_\mathrm{d} & \sin\theta_\mathrm{d} \\ -\sin\theta_\mathrm{d} & \cos\theta_\mathrm{d} \end{bmatrix} \begin{bmatrix} x_\mathrm{d} - x \\ y_\mathrm{d} - y \end{bmatrix}, \tag{2.3}$$

where θ_d is the heading of the delayed leader. Note that $(\varepsilon_1, \varepsilon_2) \longrightarrow 0$ if and only if $(x_\mathrm{d} - x, y_\mathrm{d} - y) \longrightarrow 0$. As a result, if $(\varepsilon_1, \varepsilon_2)$ is regulated to zero, then we have achieved our goal of tracking a constant-velocity delayed leader.

Continuing with the vehicle-model derivation, the follower is assumed to be perfectly tracking a constant-velocity delayed leader (i.e., speed and heading are constant), and a variation about that trajectory is considered:

$$\begin{aligned} x(t) &= x_\mathrm{d}(t) + \delta x(t) \\ y(t) &= y_\mathrm{d}(t) + \delta y(t) \\ \theta(t) &= \theta_\mathrm{d} + \delta\theta(t) \\ v_\mathrm{c}(t) &= v_\mathrm{d} + \delta v_\mathrm{c}(t) \\ \gamma_\mathrm{c}(t) &= \gamma_\mathrm{d} + \delta\gamma_\mathrm{c}(t) = \delta\gamma_\mathrm{c}(t). \end{aligned}$$

Similarly, variations in the tracking errors about the same trajectory are

$$\begin{aligned} \varepsilon_1(t) &= 0 + \delta\varepsilon_1(t) = \delta\varepsilon_1(t) \\ \varepsilon_2(t) &= 0 + \delta\varepsilon_2(t) = \delta\varepsilon_2(t). \end{aligned}$$

Substituting the variations into (2.3) gives

$$\begin{aligned}
\delta\varepsilon_1 &= (x_\mathrm{d} - x_\mathrm{d} - \delta x)\cos\theta_\mathrm{d} + (y_\mathrm{d} - y_\mathrm{d} - \delta y)\sin\theta_\mathrm{d} \\
&= -\cos\theta_\mathrm{d}\delta x - \sin\theta_\mathrm{d}\delta y \\
\delta\varepsilon_2 &= -(x_\mathrm{d} - x_\mathrm{d} - \delta x)\sin\theta_\mathrm{d} + (y_\mathrm{d} - y_\mathrm{d} - \delta y)\cos\theta_\mathrm{d} \\
&= \sin\theta_\mathrm{d}\delta x - \cos\theta_\mathrm{d}\delta y.
\end{aligned}$$

Taking derivatives yields

$$\delta\dot{\varepsilon}_1 = -\cos\theta_\mathrm{d}\delta\dot{x} - \sin\theta_\mathrm{d}\delta\dot{y} \tag{2.4}$$

$$\delta\dot{\varepsilon}_2 = \sin\theta_\mathrm{d}\delta\dot{x} - \cos\theta_\mathrm{d}\delta\dot{y}. \tag{2.5}$$

In addition, substituting the variations into the bicycle model and keeping only first-order effects gives

$$\delta\dot{x} = \cos\theta_\mathrm{d}\delta v_\mathrm{c} - v_\mathrm{d}\sin\theta_\mathrm{d}\delta\theta \tag{2.6}$$

$$\delta\dot{y} = \sin\theta_\mathrm{d}\delta v_\mathrm{c} + v_\mathrm{d}\cos\theta_\mathrm{d}\delta\theta \tag{2.7}$$

$$\delta\dot{\theta} = \frac{v_\mathrm{d}}{d}\delta\gamma_\mathrm{c}. \tag{2.8}$$

Plugging (2.6) and (2.7) into (2.4) and (2.5) yields

$$\begin{aligned}
\delta\dot{\varepsilon}_1 &= -\cos\theta_\mathrm{d}(\cos\theta_\mathrm{d}\delta v_\mathrm{c} - v_\mathrm{d}\sin\theta_\mathrm{d}\delta\theta) - \sin\theta_\mathrm{d}(\sin\theta_\mathrm{d}\delta v_\mathrm{c} + v_\mathrm{d}\cos\theta_\mathrm{d}\delta\theta) \\
&= -\delta v_\mathrm{c} \qquad (2.9) \\
\delta\dot{\varepsilon}_2 &= \sin\theta_\mathrm{d}(\cos\theta_\mathrm{d}\delta v_\mathrm{c} - v_\mathrm{d}\sin\theta_\mathrm{d}\delta\theta) - \cos\theta_\mathrm{d}(\sin\theta_\mathrm{d}\delta v_\mathrm{c} + v_\mathrm{d}\cos\theta_\mathrm{d}\delta\theta) \\
&= -v_\mathrm{d}\delta\theta. \qquad (2.10)
\end{aligned}$$

By defining the heading error, ε_3, as

$$\varepsilon_3 := \theta_\mathrm{d} - \theta = \delta\theta =: \delta\varepsilon_3, \tag{2.11}$$

(2.8)–(2.11) are combined to give our local kinematic model:

$$\begin{aligned}
\delta\dot{\varepsilon}_1 &= -\delta v_\mathrm{c} \\
\delta\dot{\varepsilon}_2 &= v_\mathrm{d}\delta\varepsilon_3 \\
\delta\dot{\varepsilon}_3 &= -\frac{v_\mathrm{d}}{d}\delta\gamma_\mathrm{c}.
\end{aligned}$$

From the variation definitions, our local model, as a function of the actual tracking errors and control signals (i.e., dropping the δ's), is equivalently

$$\begin{aligned}
\dot{\varepsilon}_1 &= v_\mathrm{d} - v_\mathrm{c} \\
\dot{\varepsilon}_2 &= v_\mathrm{d}\varepsilon_3 \\
\dot{\varepsilon}_3 &= -\frac{v_\mathrm{d}}{d}\gamma_\mathrm{c}.
\end{aligned} \tag{2.12}$$

This completes the derivation of the vehicle model.

To perfectly track a constant-velocity delayed leader, v_c and γ_c should be chosen such that $(\varepsilon_1, \varepsilon_2) \longrightarrow 0$ as $t \longrightarrow \infty$ in (2.12). Noting that (2.12) is decoupled in the longitudinal and lateral directions, we chose

$$v_\mathrm{c} = v_\mathrm{d} + k_{\mathrm{p},1}\varepsilon_1, \tag{2.13}$$

for the commanded speed. The corresponding longitudinal closed-loop system is

$$\dot{\varepsilon}_1 = -k_{\mathrm{p},1}\varepsilon_1,$$

which is asymptotically stable for all positive $k_{\mathrm{p},1}$. For the commanded steering, we chose

$$\gamma_{\mathrm{c}} = k_{\mathrm{p},2}\varepsilon_2 + k_{\mathrm{p},3}\varepsilon_3. \tag{2.14}$$

The corresponding lateral closed-loop system is

$$\begin{bmatrix} \dot{\varepsilon}_2 \\ \dot{\varepsilon}_3 \end{bmatrix} = \begin{bmatrix} 0 & v_{\mathrm{d}} \\ -k_{\mathrm{p},2} & -k_{\mathrm{p},3} \end{bmatrix} \begin{bmatrix} \varepsilon_2 \\ \varepsilon_3 \end{bmatrix},$$

which is asymptotically stable for all positive v_{d}, $k_{\mathrm{p},2}$, and $k_{\mathrm{p},3}$. Hence, with these choices for v_{c} and γ_{c}, a constant-velocity delayed leader can be tracked with zero steady-state error.

2.3.1 Look-ahead Feature

After some initial field trials, we discovered that the follower was turning wide, which caused a large lateral error. We hypothesized that the wide turns were caused by low gains in our controller and delays in the vehicle's steering dynamics. To compensate, we added a look-ahead feature for the lateral controller, a feature that is commonly used in autonomous vehicles (e.g., Gehrig and Stein [14], Marshall et al. [28], and Papadimitriou et al. [32]). However, unlike others that use a constant-distance look-ahead, our look-ahead feature is based on a constant time, which allows for consistent follower behaviour across different speeds. Our look-ahead point is defined as

$$(x_{\mathrm{l}}(t), y_{\mathrm{l}}(t)) := (x_0(t-\tau+l), y_0(t-\tau+l)), \quad 0 \le l \le \tau,$$

where l is a constant, but configurable, look-ahead time. With a look-ahead time defined, the heading error is computed by

$$\varepsilon_3 = \theta_{\mathrm{l}} - \theta,$$

where θ_{l} is the heading of the look-ahead point. Note that the look-ahead feature does not have an effect when the leader is traveling in a straight trajectory.

2.3.2 Integral Terms

Also through early field trials using (2.13) and (2.14) as our control laws, we discovered that the longitudinal tracking error was not going to zero on straightaways and that there was a constant lateral tracking error when there was a constant side slope on the road. For the longitudinal error, we hypothesized that there may be a model uncertainty, δ_1, introduced through linearizing about a constant-velocity trajectory. As a result, our longitudinal model may, in actuality, be

$$\dot{\varepsilon}_1 = v_{\mathrm{d}} - v_{\mathrm{c}} + \delta_1.$$

Assume δ_1 is relatively slow-varying so that it can be treated as a constant; if (2.13) is applied to the above longitudinal model, then the closed-loop system becomes

$$\dot{\varepsilon}_1 = -k_{\mathrm{p},1}\varepsilon_1 + \delta_1,$$

which is asymptotically stable with equilibrium at $\varepsilon_1 = \frac{\delta_1}{k_{\mathrm{p},1}}$. To make sure $\varepsilon_1 \longrightarrow 0$, an integral term on ε_1 was added to the commanded speed:

$$v_{\mathrm{c}} = v_{\mathrm{d}} + k_{\mathrm{p},1}\varepsilon_1 + k_{\mathrm{i},1}\int_0^t \varepsilon_1(q)dq.$$

As a result, the corresponding longitudinal closed-loop system is

$$\dot{\varepsilon}_1 = -k_{\mathrm{p},1}\varepsilon_1 - k_{\mathrm{i},1}\int_0^t \varepsilon_1(q)dq + \delta_1.$$

Let temporary variables $(z_1, z_2) := (\int_0^t \varepsilon_1(q)dq, \varepsilon_1)$; the longitudinal closed-loop system is equivalently

$$\begin{bmatrix} \dot{z}_1 \\ \dot{z}_2 \end{bmatrix} = \begin{bmatrix} 0 & 1 \\ -k_{\mathrm{i},1} & -k_{\mathrm{p},1} \end{bmatrix} \begin{bmatrix} z_1 \\ z_2 \end{bmatrix} + \begin{bmatrix} 0 \\ \delta_1 \end{bmatrix},$$

which is asymptotically stable with equilibrium at $(z_1, z_2) = (\frac{\delta_1}{k_{\mathrm{i},1}}, 0)$. Hence, adding the integral term helps make $\varepsilon_1 \longrightarrow 0$ in the presence of a slow-varying model uncertainty.

For the constant lateral error on a constant side slope, we believe the slope introduces a constant bias, δ_2, into the steering of our lateral vehicle model, resulting in

$$\begin{aligned} \dot{\varepsilon}_2 &= v_d \varepsilon_3 \\ \dot{\varepsilon}_3 &= -\frac{v_{\mathrm{d}}}{d}(\gamma_{\mathrm{c}} + \delta_2). \end{aligned}$$

The justification for this additive bias is to imagine trying to drive straight on a road with a constant side slope. In this situation, to keep the vehicle's heading from changing, the steering wheel must be kept at a constant angle in the opposite direction of the slope. Using the same argument for tracking a constant-velocity trajectory, the change in the follower's heading error, $\dot{\varepsilon}_3$, should be zero only when γ_{c} correctly compensates for the bias, δ_2, introduced by the constant side slope. Under this assumption, applying (2.14) would result in the following closed-loop system:

$$\begin{bmatrix} \dot{\varepsilon}_2 \\ \dot{\varepsilon}_3 \end{bmatrix} = \begin{bmatrix} 0 & v_{\mathrm{d}} \\ -\frac{v_{\mathrm{d}}}{d} k_{\mathrm{p},2} & -\frac{v_{\mathrm{d}}}{d} k_{\mathrm{p},3} \end{bmatrix} \begin{bmatrix} \varepsilon_2 \\ \varepsilon_3 \end{bmatrix} + \begin{bmatrix} 0 \\ -\frac{v_{\mathrm{d}}}{d}\delta_2 \end{bmatrix},$$

which is asymptotically stable with equilibrium $(\varepsilon_2, \varepsilon_3) = (\frac{-\delta_2}{k_{\mathrm{p},2}}, 0)$. Similar to the longitudinal control, adding an integral term on ε_2 would ensure $\varepsilon_2 \longrightarrow 0$. Thus, the control law becomes

$$\gamma_{\mathrm{c}} = k_{\mathrm{p},2}\varepsilon_2 + k_{\mathrm{i},2} \int_0^t \varepsilon_2(q)dq + k_{\mathrm{p},3}\varepsilon_3.$$

Let temporary variables $(z_3, z_4, z_5) := (\int_0^t \varepsilon_2(q)dq, \varepsilon_2, \varepsilon_3)$; the corresponding closed-loop system is

$$\begin{bmatrix} \dot{z}_3 \\ \dot{z}_4 \\ \dot{z}_5 \end{bmatrix} = \underbrace{\begin{bmatrix} 0 & 1 & 0 \\ 0 & 0 & v_\mathrm{d} \\ -\frac{v_\mathrm{d}}{d}k_{\mathrm{i},2} & -\frac{v_\mathrm{d}}{d}k_{\mathrm{p},2} & -\frac{v_\mathrm{d}}{d}k_{\mathrm{p},3} \end{bmatrix}}_{\mathbf{A}} \begin{bmatrix} z_3 \\ z_4 \\ z_5 \end{bmatrix} + \begin{bmatrix} 0 \\ 0 \\ -\frac{v_\mathrm{d}}{d}\delta_2 \end{bmatrix}. \tag{2.15}$$

Picking values of $k_{\mathrm{p},2}$, $k_{\mathrm{i},2}$, and $k_{\mathrm{p},3}$ such that the eigenvalues of the above $\mathbf{A}$ matrix are in the open-left-half plane ensures that the above system is asymptotically stable with equilibrium at $(z_3, z_4, z_5) = (\frac{-\delta_2}{k_{\mathrm{i},2}}, 0, 0)$. Hence, adding the integral term on the lateral control law eliminates the constant lateral error associated with a constant side slope.

2.3.3 Pole Placement and Lateral Gain Scheduling

Similar to the point-ahead controller, we used pole placement to find the largest set of gains that still yields stable follower behaviour. For the longitudinal control, the characteristic polynomial is

$$s^2 + k_{\mathrm{p},1}s + k_{\mathrm{i},1}. \tag{2.16}$$

To avoid oscillatory effects, the closed-loop poles are placed on the negative real axis. Let a and b be the pole locations; then, the desired characteristic polynomial is

$$(s-a)(s-b) = s^2 - (a+b)s + ab. \tag{2.17}$$

By comparing (2.16) with (2.17), we get algebraic equations for the gains in terms of the pole locations:

$$k_{\mathrm{p},1} = -(a+b)$$

$$k_{\mathrm{i},1} = ab.$$

The lateral control is more involved. From (2.15), it is obvious that the eigenvalues of the **A** matrix are dependent on v_d. As a result, the closed-loop dynamics of the lateral control may vary greatly over a range of different speeds. To keep the closed-loop dynamics consistent, pole placement is used for gain scheduling across different speeds. This approach yields consistent lateral gains across all speeds, which is not possible with a fixed set of gains.

The lateral gain scheduling is done by comparing the characteristic polynomial of (2.15) with the characteristic polynomial from the desired pole locations. The characteristic polynomial of (2.15) is

$$s^3 + \frac{v_\mathrm{d}}{d}k_{\mathrm{p},3}s^2 + \frac{v_\mathrm{d}^2}{d}k_{\mathrm{p},2}s + \frac{v_\mathrm{d}^2}{d}k_{\mathrm{i},2}. \tag{2.18}$$

Again, let the real pole locations be a, b, and c; then, the desired characteristic polynomial is

$$(s-a)(s-b)(s-c) = s^3 - (a+b+c)s^2 + (ab+ac+bc)s - abc. \tag{2.19}$$

By comparing (2.18) with (2.19), algebraic equations for the gains in terms of the pole locations are obtained:

$$\begin{aligned} k_{\mathrm{p},2} &= d\frac{ab+ac+bc}{v_\mathrm{d}^2} \\ k_{\mathrm{i},2} &= -d\frac{abc}{v_\mathrm{d}^2} \\ k_{\mathrm{p},3} &= -d\frac{a+b+c}{v_\mathrm{d}}. \end{aligned}$$

Based on the above equations, lateral gains can be continuously calculated for any $v_\mathrm{d} > 0$. To avoid the $v_\mathrm{d} = 0$ case, a minimum positive v_d is required.

2.4 Nonlinear Observer

To implement the point-ahead controller, the positions and headings of the follower and the delayed leader are required to estimate $\mathbf{p}_\mathrm{d} - \mathbf{p}$. For the decoupled controller, in addition to the positions and headings of both vehicles, the delayed leader's speed and the heading of the look-ahead point are also required. Hence, the inputs to the point-ahead controller are a subset of the inputs to the decoupled controller, as shown in Figure 2.5. The MATS vehicle's on-board sensors do not measure any of the required signals directly. Instead, a nonlinear observer is implemented to estimate the required inputs.

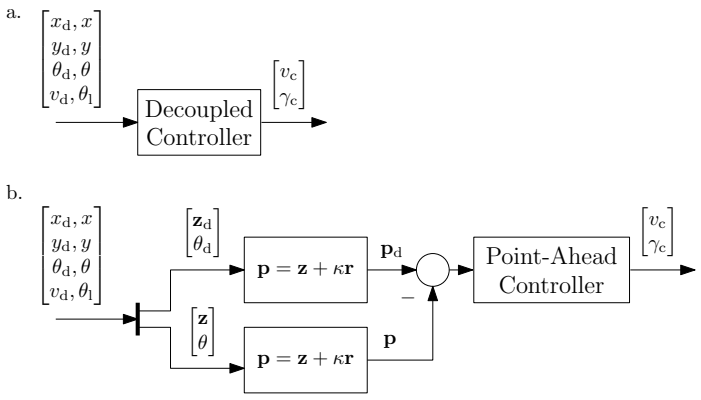

Figure 2.5: (a) Decoupled controller diagram. (b) Point-ahead controller diagram. Note that the inputs to the point-ahead controller are a subset of the inputs to the decoupled controller.

The inputs to the nonlinear observer are the outputs of the follower's measurement sensors, as shown in Figure 2.6. Recall that the sensors consist of a camera and wheel encoders. The camera measures the range and bearing to the leader vehicle, and the wheel encoders measure the follower's speed and steering. From these measurements, the nonlinear observer estimates the inputs required for the point-ahead and decoupled controllers. The controllers are represented by a generic 'controller' box in Figure 2.6.

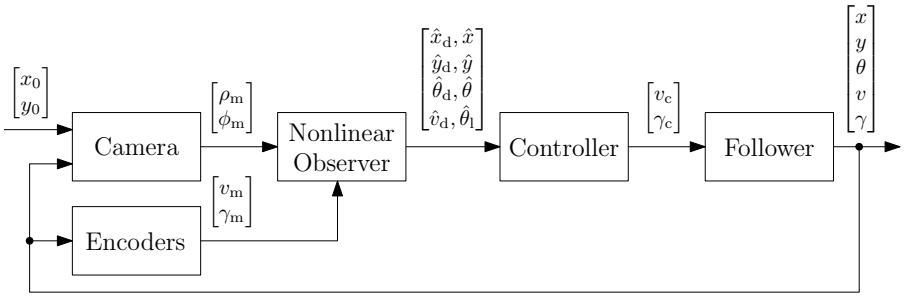

Figure 2.6: Top-level diagram of overall system.

2.4.1 Dead Reckoning

The follower's position is estimated using dead reckoning. From the vehicle kinematics,

$$\dot{x} = v_\mathrm{c} \cos\theta$$
$$\dot{y} = v_\mathrm{c} \sin\theta$$
$$\dot{\theta} = \frac{v}{d} \tan\gamma,$$

the follower's position and heading can be estimated from the measured speed and steering using

$$\hat{\theta}(t) = \int_0^t \frac{v_\mathrm{m}(q)}{d} \tan\gamma_\mathrm{m}(q) dq + \theta(0)$$
$$\hat{x}(t) = \int_0^t v_\mathrm{m}(q) \cos\hat{\theta}(q) dq + x(0)$$
$$\hat{y}(t) = \int_0^t v_\mathrm{m}(q) \sin\hat{\theta}(q) dq + y(0).$$

Clearly, initial values for the position and heading are required, but these can easily be set to zero or be initialized to the DGPS measurement values. Although this setup works in simulation, it did not work on the MATS vehicle. The reason is that the steering sensor is located on the steering column, rather than the front wheels. Since there is significant 'play' between the steering wheel and the front wheels, the steering measurements do not accurately represent the direction of the front wheels, especially on sloped roads. As

a result, the heading estimate is highly inaccurate, causing the position estimates to be even worse. An detailed example is given in Section 4.2. To fix this problem, we added a heading gyro to the MATS vehicle, which measures the vehicle's heading. Note that the gyro actually measures the vehicle's turning rate and integrates to obtain the vehicle's heading. However, since the gyro outputs the heading, for simplicity, we assumed the heading to be the measurement.

The overall system diagram is updated with the heading gyro in Figure 2.7. Now, the follower's heading is measured by the gyro instead of being estimated from the steering measurement. Hence, the follower's steering, γ, no longer appears in the follower's output. The follower's position estimates are now obtained using

$$\hat{x}(t) = \int_0^t v_{\mathrm{m}}(q)\cos\theta_{\mathrm{m}}(q)dq + x(0)$$
$$\hat{y}(t) = \int_0^t v_{\mathrm{m}}(q)\sin\theta_{\mathrm{m}}(q)dq + y(0).$$

A block diagram of this new dead-reckoning process is shown in Figure 2.8.

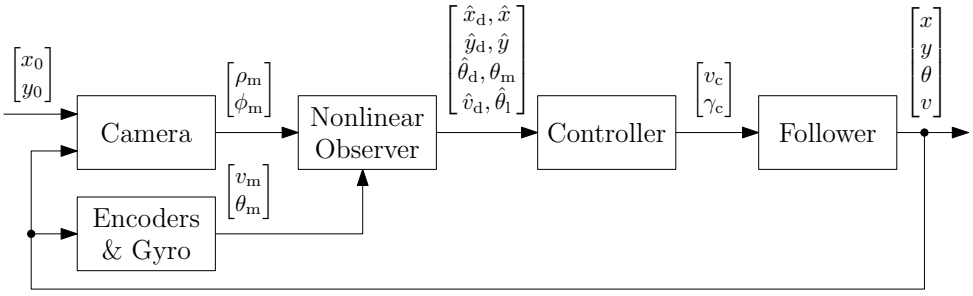

Figure 2.7: Updated top-level diagram of overall system with heading gyro.

As previously mentioned in Section 1.2.2, the uncertainty in the position estimates using dead reckoning grows unbounded with time [5]. One necessary condition for our design to work is that the uncertainty in the input to the controller must be bounded. This may not be obvious since the follower's position is estimated through dead reckoning. However, proofs of the uncertainty in both the point-ahead and decoupled controllers' inputs being bounded are given in Appendix A.

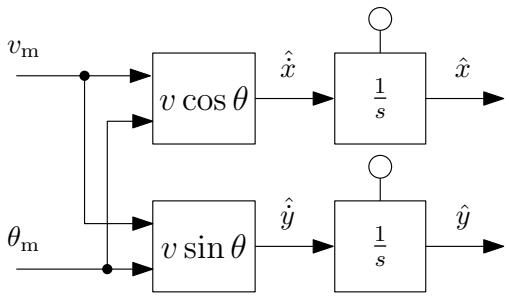

Figure 2.8: Dead-reckoning process using measured speed and heading as inputs.

2.4.2 Delayed Leader and Look-Ahead Point Estimations

The remaining controller inputs to be estimated in Figure 2.7 are the delayed leader's position, heading, and speed, along with the heading of the look-ahead point. As shown in Figure 2.9, the leader's position can be estimated from the range and bearing and the follower's estimated position and measured heading. Specifically,

$$\hat{x}_0(t) = \hat{x}(t) + \rho_\mathrm{m}(t)\cos(\theta_\mathrm{m}(t) + \phi_\mathrm{m}(t))$$
$$\hat{y}_0(t) = \hat{y}(t) + \rho_\mathrm{m}(t)\sin(\theta_\mathrm{m}(t) + \phi_\mathrm{m}(t)).$$

Note that the offsets between the camera and the follower's rear axle and between the target and the leader's rear axle need to be taken into consideration, but is left out for simplicity of explanation. From its definition, the delayed leader estimated position is obtained by

$$\hat{x}_\mathrm{d}(t) = \hat{x}_0(t - \tau)$$
$$\hat{y}_\mathrm{d}(t) = \hat{y}_0(t - \tau),$$

and, similarly, the estimated look-ahead point is

$$\hat{x}_\mathrm{l}(t) = \hat{x}_0(t - \tau + l)$$
$$\hat{y}_\mathrm{l}(t) = \hat{y}_0(t - \tau + l).$$

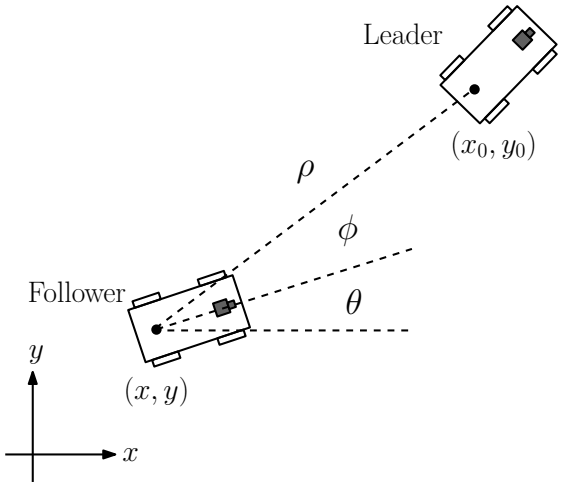

Figure 2.9: Obtaining the leader's position from the range and bearing and the follower's position and heading.

Since the above positions are in continuous time, we can differentiate to obtain $(\dot{\hat{x}}_\mathrm{d}, \dot{\hat{y}}_\mathrm{d})$ and $(\dot{\hat{x}}_\mathrm{l}, \dot{\hat{y}}_\mathrm{l})$, the derivatives of the estimated positions. Again, using the vehicle kinematics, the delayed leader's speed and heading can be estimated with

$$\hat{v}_\mathrm{d} = \sqrt{\dot{\hat{x}}_\mathrm{d}^2 + \dot{\hat{y}}_\mathrm{d}^2}$$
$$\hat{\theta}_\mathrm{d} = \mathrm{atan2}(\dot{\hat{x}}_\mathrm{d}, \dot{\hat{y}}_\mathrm{d}),$$

where atan2 is the four-quadrant arctangent. Likewise, the estimated look-ahead point's heading is

$$\hat{\theta}_\mathrm{l} = \mathrm{atan2}(\dot{\hat{x}}_\mathrm{l}, \dot{\hat{y}}_\mathrm{l}).$$

However, in implementation, the signals are not continuous-time, but are discrete-

time. Consequently, differentiating to obtain $(\dot{\hat{x}}_{\mathrm{d}}, \dot{\hat{y}}_{\mathrm{d}})$ and $(\dot{\hat{x}}_{\mathrm{l}}, \dot{\hat{y}}_{\mathrm{l}})$ is not straight forward. Furthermore, there is noise associated with sensor measurements, making signal estimation more difficult. The following section details the implementation of the vehicle-following system, along with handling noise and possible data dropout.

2.5 Implementation

In the actual implementation of our vehicle-following system on the MATS vehicle, the measured signals are sampled and the commanded speed and steering are held, as shown in Figure 2.10. The S is the sampler, the H is the hold, and the dashed lines represent discrete-time signals. From the vehicle-following system's perspective, there is only one sampling rate. Although the sensor measurements are sensed at different rates, the measurements are passed synchronously into the nonlinear observer. The diagrams for the sampler and hold are shown in Figure 2.11. The output of the sampler takes on the value of the input at every kT, where T is the sampling period and $k \in \mathbb{N}_0$. The output of the hold is

$$u(t) = u(kT), \quad kT \leq t < (k+1)T.$$

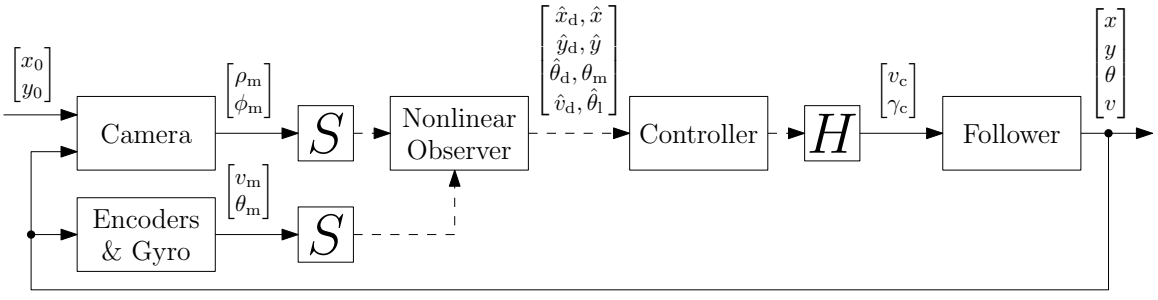

Figure 2.10: Top-level diagram of overall sampled-data system.

From Figure 2.10, it is obvious that we need discrete-time equivalents of the nonlinear observer and controller blocks. For the controller block, its discrete-time equivalent

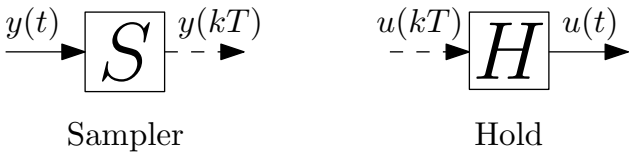

Figure 2.11: Sampler and hold diagrams.

is fairly straight forward since both the point-ahead and decoupled controllers are PI controllers. As a result, the controller conversion requires only discretizing the integrator for which we used the trapezoidal rule. The discrete-time equivalent of the nonlinear observer is more complex since the range and bearing are expected to be noisy and differentiation (to estimate the delayed leader's speed and heading) in discrete time is inherently difficult.

A diagram of the discrete-time nonlinear observer is shown in Figure 2.12. The dead reckoning is the same as the continuous-time version except the integrators are replaced with their discrete-time equivalents using the trapezoidal rule. The dead reckoning outputs the follower's estimated position and measured heading, which are also outputs of the nonlinear observer. The follower's position and heading are buffered to match smoothed range and bearing measurements to produce a 'window' of leader positions. The follower's position and heading do not need to be smoothed because they are produced from integration processes, which naturally smooth the signals (the heading is produced from the gyro integrating the follower's turning rate). However, the range and bearing are expected to be noisy and thus are smoothed. Once the window of leader positions is obtained, separate lines are fitted to the x_0 and y_0 positions centred around $t - \tau$. The resulting slopes are used as estimates of $\dot{x}_\mathrm{d}$ and $\dot{y}_\mathrm{d}$, which allows $\hat{v}_\mathrm{d}$ and $\hat{\theta}_\mathrm{d}$ to be computed. A similar process is used to compute $\hat{\theta}_\mathrm{l}$. The details of smoothing the range and bearing and estimating the delayed leader's speed and heading are provided in the following sections.

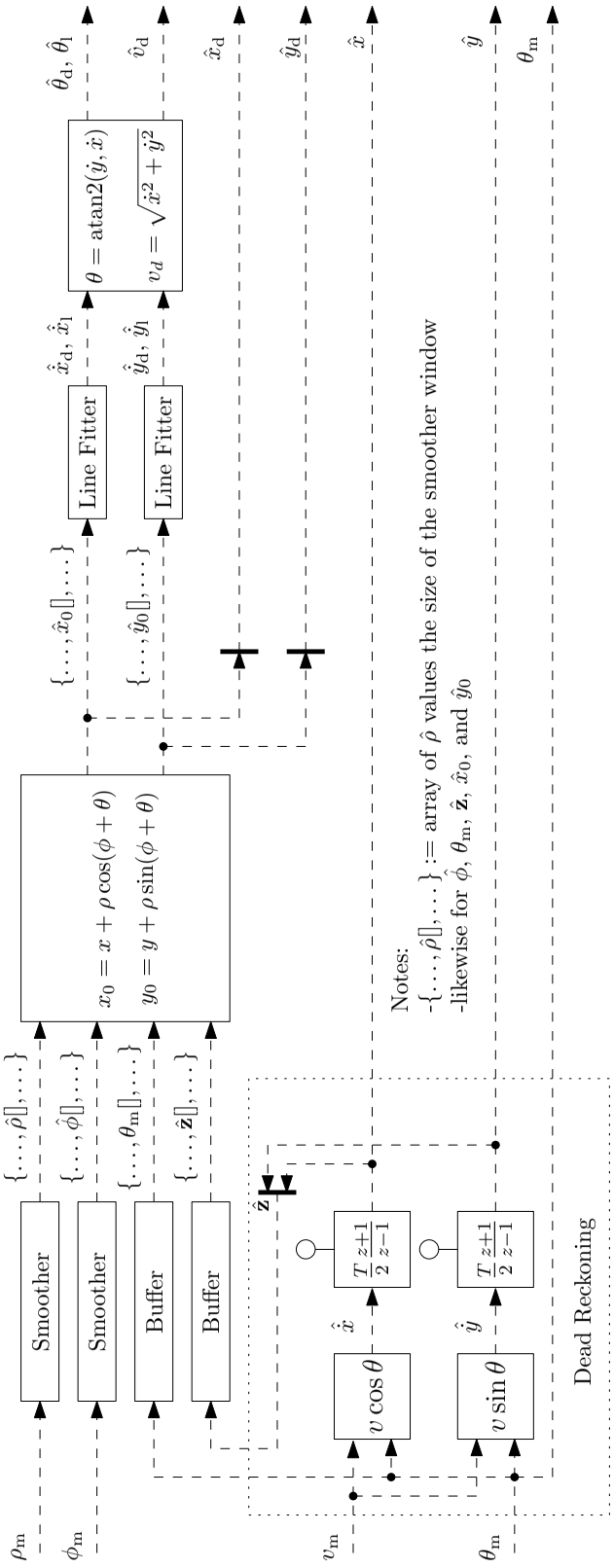

Figure 2.12: Discrete-time nonlinear observer.

2.5.1 Smoothing the Range and Bearing Measurements

The range and bearing measurements are expected to be noisy. Our approach to deal with the noise is the same for both the range and bearing measurements. Henceforth, we will discuss only the range measurements.

To calculate the delayed leader's position, $\rho(t-\tau)$ is needed. There are range measurements from time 0 to t, so future measurements can be used to smooth the estimate at $t-\tau$. We took the approach of using cubic splines to fit a curve to the measurements. These piecewise polynomials have the advantage of continuous first and second derivatives and minimize the curvature of the fitted curved [24]. The continuous first derivative is helpful as the derivative of the range is implicitly used in the derivative of the delayed leader's position, which is used to calculate the delayed leader's speed and heading. The property of minimum curvature gives the curve a smooth appearance.

A window of measurements centred around $t-\tau$ is used to estimate $\rho(t-\tau)$. This window size, n, is configurable, but, of course, needs to be less than or equal to 2τ since we have measurements up to only time t. Note that if a positive look-ahead time, l, is specified, then n needs to be less than or equal to $2(\tau-l)$. A diagram of the smoother is shown in Figure 2.13. The smoother can handle occasional data dropouts, which may occur with a camera on moving vehicles. The splines, S_{j}, used to fit the data are identical, separated by a configurable q seconds, and set to be $4q$ in width. The number of splines is determined by n and q, and only splines affected by the data points are considered, meaning there are splines located outside the smoother window. The fitted curve in the summation of the splines, which are scaled by the coefficients, c_{j}, respectively.

In more detail, the splines used in the smoother are a shifted version of the spline

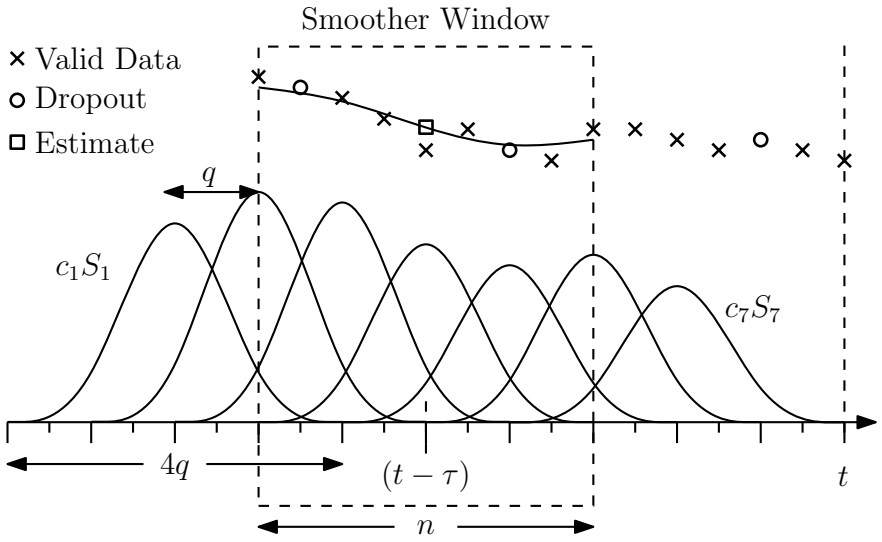

Figure 2.13: Smoother using cubic splines.

given by Constable and Parker [6]:

$$S(t) = \begin{cases} (2+t)^3, & -2 \le t \le -1 \\ 4 - 6t^2 - 3t^3, & -1 \le t \le 0 \\ 4 - 6t^2 + 3t^3, & 0 \le t \le 1 \\ (2-t)^3, & 1 \le t \le 2. \end{cases}$$

Let $S_{\rm j}(t)$, $j = 1, \ldots, p$ be the jth cubic spline, and given p splines, a curve $f(t)$ can be constructed by

$$f(t) = \sum_{\rm j=1}^{p} c_{\rm j} S_{\rm j}(t),$$

where $c_{\rm j}$ is the coefficient used to scale its corresponding spline. To fit a curve to a window of range measurements, we need to find the $c_{\rm j}$'s.

Similar to Teanby [39], $f(t)$ is sampled to create a vector and least squares is used to solve for the $c_{\rm j}$'s. Since, in the n-second smoother window, there are $m := \frac{n}{T}$ range measurements from $t_1 := t - \tau - \frac{n}{2}$ to $t_{\rm m} := t - \tau + \frac{n}{2}$, $f(t)$ can be written as

$$\mathbf{f} = \mathbf{A}\mathbf{c}, \tag{2.20}$$

where $\mathbf{f}$ is the n-dimensional vector with $f_i = f(t_i)$, $\mathbf{A}$ is the $n \times p$ matrix with $A_{ij} = S_j(t_i)$, and $\mathbf{c}$ is the p-dimensional vector of coefficients. The optimal $\mathbf{c}$ in the least-squares sense is obtained by minimizing the following objective function:

$$\begin{aligned}\Phi &= \frac{1}{2}\sum_{i=1}^{n}(\mathbf{w}-\mathbf{f})^2 \\ &= \frac{1}{2}\sum_{i=1}^{n}(\mathbf{w}-\mathbf{A}\mathbf{c})^2\end{aligned}$$

where $\mathbf{w}$ is m-dimensional vector with $w_i = \rho_m(t_i)$. Differentiating Φ with respect to $\mathbf{c}$ and setting the derivative equal to zero results in the standard least-squares solution:

$$\mathbf{c} = (\mathbf{A}^T\mathbf{A})^{-1}\mathbf{A}^T\mathbf{w}. \tag{2.21}$$

Hence, $\mathbf{f}$ is computed using (2.20) and $f(t-\tau)$ is used as the estimate for $\rho_m(t-\tau)$.

2.5.2 Handling Data Dropouts

With a camera on a moving vehicle on bumpy roads, invalid range and/or bearing measurements may be common. Detecting these dropouts is first done on the camera system and then is relayed to the smoother by setting the range and bearing to known invalid values. In our vehicle-following system, an invalid range is a number greater than or equal to 1000, and an invalid bearing is greater than or equal to π. The smoother ignores any invalid values and fits a curve only to the valid data.

Since the smoother uses cubic splines that are finite in width, it can only handle up to a finite number of consecutive dropouts. Specifically, at least one valid data point is required in the time period covered by each spline to avoid a singularity in (2.21). Because there are splines located outside the smoother window where the first and last splines only cover q seconds each (similar to the setup shown in Figure 2.13), the number of consecutive dropouts must be less than $\frac{q}{T}$.

2.5.3 Discrete-time Speed and Heading Estimations

By fitting curves to the range and bearing measurements, respectively, estimates $\hat{\rho}(t_1), \ldots, \hat{\rho}(t_\mathrm{m})$ and $\hat{\phi}(t_1), \ldots, \hat{\phi}(t_\mathrm{m})$ are obtained. These estimates are combined with the follower's estimated position and measured heading over the same time period using

$$\hat{x}_0(t) = \hat{x}(t) + \hat{\rho}(t)\cos(\theta_\mathrm{m}(t) + \hat{\phi}(t))$$
$$\hat{y}_0(t) = \hat{y}(t) + \hat{\rho}(t)\sin(\theta_\mathrm{m}(t) + \hat{\phi}(t))$$

to get estimates of the leader's position from t_1 to t_m. To estimate $\dot{x}_\mathrm{d}$, a line is fitted over a window of $\hat{x}_0(t)$ values centred around $t-\tau$ and the slope is used as $\hat{\dot{x}}_\mathrm{d}$, the estimate of $\dot{x}_\mathrm{d}$. This is shown in Figure 2.14. The line-fitting window size is configurable, but must be less than or equal to the size of the smoother window.

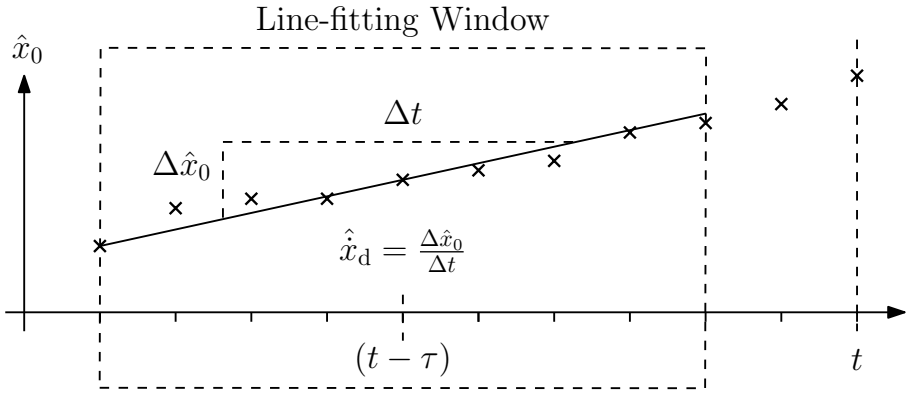

Figure 2.14: Line fitting to estimate $\dot{x}_\mathrm{d}$.

Again, least squares is used to fit the line. Assume the line-fitting window is the same size as the smoother window, i.e., all the $\hat{x}_0(t)$ values from t_1 to t_m are used; then the fitted line over the windowing period can be written in vector form as

$$\mathbf{x}_0 = \mathbf{B}\mathbf{d}, \tag{2.22}$$

where $\mathbf{x}_0$ is the m-dimensional vector with the i^{th} row being the value of the line at t_i,

$\mathbf{B}$ is the $m \times 2$ matrix with $B_{\mathrm{i},1} = 1$ and $B_{\mathrm{i},2} = t_{\mathrm{i}}$, and $\mathbf{d} := (d_1, d_2)$, where d_1 is the line constant and d_2 is the slope of the line. The optimal $\mathbf{d}$ in the least-squares sense is obtained by minimizing the following objective function:

$$\begin{aligned}\Psi &= \frac{1}{2}\sum_{\mathrm{i}=1}^{n}\left(\hat{\mathbf{x}}_0 - \mathbf{x}_0\right)^2 \\ &= \frac{1}{2}\sum_{\mathrm{i}=1}^{n}\left(\hat{\mathbf{x}}_0 - \mathbf{B}\mathbf{d}\right)^2,\end{aligned}$$

where $\hat{\mathbf{x}}_0$ is m-dimensional vector with $\hat{x}_{0,\mathrm{i}} = \hat{x}_0(t_{\mathrm{i}})$. Differentiating Ψ with respect to $\mathbf{d}$ and setting the derivative equal to zero results in the standard least-squares solution:

$$\mathbf{d} = (\mathbf{B}^{\mathrm{T}}\mathbf{B})^{-1}\mathbf{B}^{\mathrm{T}}\hat{\mathbf{x}}_0. \tag{2.23}$$

Hence, d_2 is used as the estimate for $\dot{x}_{\mathrm{d}}$.

The same method is used to estimate $\dot{y}_{\mathrm{d}}$. Once $\hat{\dot{x}}_{\mathrm{d}}$ and $\hat{\dot{y}}_{\mathrm{d}}$ are computed, the delayed leader's estimated speed and heading are calculated using

$$\begin{aligned}\hat{v}_{\mathrm{d}} &= \sqrt{\hat{\dot{x}}_{\mathrm{d}}^2 + \hat{\dot{y}}_{\mathrm{d}}^2} \\ \hat{\theta}_{\mathrm{d}} &= \mathrm{atan2}(\hat{\dot{x}}_{\mathrm{d}}, \hat{\dot{y}}_{\mathrm{d}}).\end{aligned}$$

This line-fitting technique is also used to estimate the look-ahead point's heading, θ_{l}.

2.5.4 Starting and Stopping

Since the follower is tracking the delayed leader, if the leader is not moving, then the follower will want to be at the exact same position as the leader. This condition occurs during starting and stopping situations. To handle the startup situation, the follower has a startup mode where it waits for the leader to move before it moves. This is done by storing the initial range to the leader and checking subsequent range measurements to

the initial measurement to ensure that the leader has moved. An initial range tolerance is used to avoid false starts due to measurement noise.

For the stopping situation, the follower's current range to the leader is again used. This time, the range is compared with a safety distance that is a function of the follower's speed and the time delay. The safety distance is given by

$$d_{\text{safe}} = \lambda_{\text{safe}} v_{\text{m}} \tau + \rho_{\text{safe}},$$

where λ_{safe} is a configurable percentage and ρ_{safe} is a configurable constant safety distance. If the current range is smaller than d_{safe}, then the follower stops, stores the current range as the initial range, and returns to startup mode.

Another issue with tracking the delayed leader is that the smoothers and buffers for the range, bearing, position, and heading are not populated when the vehicle-following system first starts up. To avoid this problem, the smoothers and buffers data are populated with initial range, bearing, position, and heading values, respectively. Although unnecessary, initial position and heading values are obtained by DGPS measurements so that the estimate values can be easily be compared with the DGPS ground truth[1] after the trial.

2.5.5 Bumpless Transfer and Anti-Windup

During startup, the follower is positioned behind the leader, which causes a large longitudinal error between the delayed leader and the follower. Since both the point-ahead and decoupled controllers are designed to regulate the tracking errors to zero, the commanded speed will be large at the start, which is undesirable. Since both controllers have integral terms, initial integral values can be set such that there is a 'bumpless transfer' between

[1]DGPS measurements (except heading) are the most accurate measurements we employ and hence serves as ground truth for other sensor measurements.

the commanded speed and the initial speed of zero.

For the point-ahead controller, since

$$v_{\mathrm{c}} = \mathbf{r}^{\mathrm{T}}\tilde{\mathbf{u}},$$

$\tilde{\mathbf{u}}$ being zero ensures v_{c} equals zero. Given

$$\begin{aligned}\tilde{\mathbf{u}} &= k_{\mathrm{p}}(\mathbf{p}_{\mathrm{d}} - \mathbf{p}) + k_{\mathrm{i}} \int_0^t (\mathbf{p}_{\mathrm{d}} - \mathbf{p})(q)dq \\ &=: k_{\mathrm{p}}(\mathbf{p}_{\mathrm{d}} - \mathbf{p}) + k_{\mathrm{i}}\tilde{\mathbf{I}},\end{aligned}$$

where $\tilde{\mathbf{I}}$ represents the integral term, initializing

$$\tilde{\mathbf{I}} = -\frac{k_{\mathrm{p}}(\mathbf{p}_{\mathrm{d}} - \mathbf{p})}{k_{\mathrm{i}}}$$

will ensure the commanded speed starts off at zero.

For the decoupled controller,

$$\begin{aligned}v_{\mathrm{c}} &= v_{\mathrm{d}} + k_{\mathrm{p},1}\varepsilon_1 + k_{\mathrm{i},1} \int_0^t \varepsilon_1(q)dq \\ &=: v_{\mathrm{d}} + k_{\mathrm{p},1}\varepsilon_1 + k_{\mathrm{i},1}I_1,\end{aligned}$$

where I_1 represents the integral term. Thus, initializing

$$I_1 = -\frac{v_{\mathrm{d}} + k_{\mathrm{p},1}\varepsilon_1}{k_{\mathrm{i},1}}$$

will ensure a bumpless transfer to the initial commanded speed.

Another implementation issue with integral terms is 'windup', which occurs when the follower's speed or steering hits its physical limits and saturates. When the follower's speed or steering saturates, it can no longer execute the commanded speed or steering,

causing the tracking errors to continuously increase and the integral terms to continuously accumulative those errors, hence, winding up. Thus, the saturation limits need to be taken into account and checks are required to ensure that the integral terms stop accumulating when a saturation limit is hit.

Chapter 3

Simulation Model

To validate our design, we created a simulation environment in Simulink, a MathWorks product that allows for the simulation of mathematical models. The simulation block diagram for a leader-follower pair is shown in Figure 3.1. This diagram is similar to the top-level diagram shown in Figure 2.10 except that the leader vehicle is included. The reason for including the leader vehicle is that we wanted the leader's path to be created by the same model used to represent the follower.

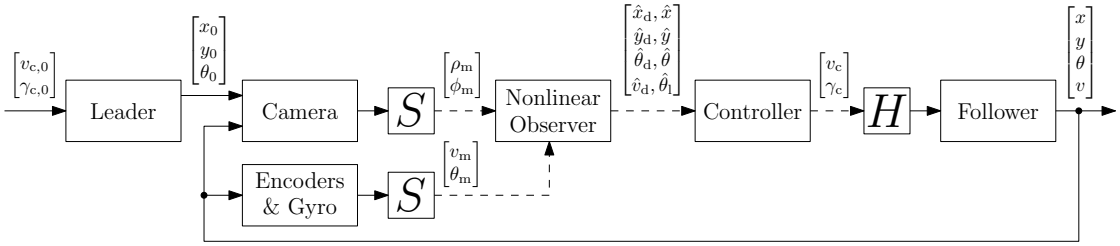

Figure 3.1: Simulation block diagram for a leader-follower pair.

The simulation environment consists of hardware components (the leader, the follower, the camera, and the encoders and gyro) and software components (the nonlinear observer and the controller), and its objective is to test the software by emulating the behaviour of the hardware components. This emulation is done by using mathematical models to represent the physical components.

3.1 Vehicle Model

To simulate realistic vehicles, the vehicle model needs to include both dynamics and kinematics. From our controller design, the kinematics are represented by the bicycle model. The throttle and steering dynamics are represented by separated transfer functions obtained using system identification. Since both the leader and the follower are MATS vehicles, we assumed both vehicle's throttle and steering dynamics will be similar. Hence, we used the same transfer functions to represent the dynamics of both vehicles. A more detailed view of the vehicle model is shown in Figure 3.2.

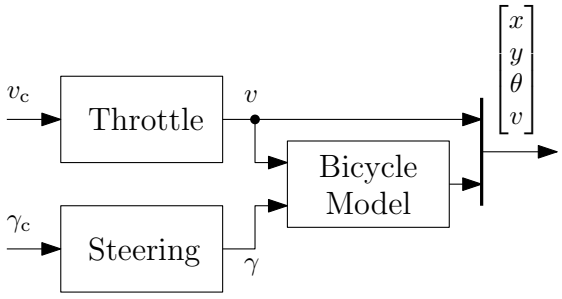

Figure 3.2: Vehicle model block diagram with throttle and steering dynamics and bicycle kinematics.

To fit transfer functions to the throttle and steering, we gathered test data from a MATS vehicle and compared the commanded inputs with the measured outputs. As shown in Figure 3.3, the throttle step response is similar to that of an underdamped second-order system of the form

$$T(s) = \frac{\omega_n^2}{s^2 + 2\zeta\omega_n + \omega_n^2},$$

where ω_n is the natural frequency and ζ is the damping ratio, while the steering response[1]

[1]The steering 'drift' from 0.59 rad and -0.54 rad was caused by a mechanical issue that has, subsequently, been fixed.

is similar to that of a first-order system of the form

$$S(s) = \frac{1}{\tau_\gamma s + 1},$$

where τ_γ is the time constant.

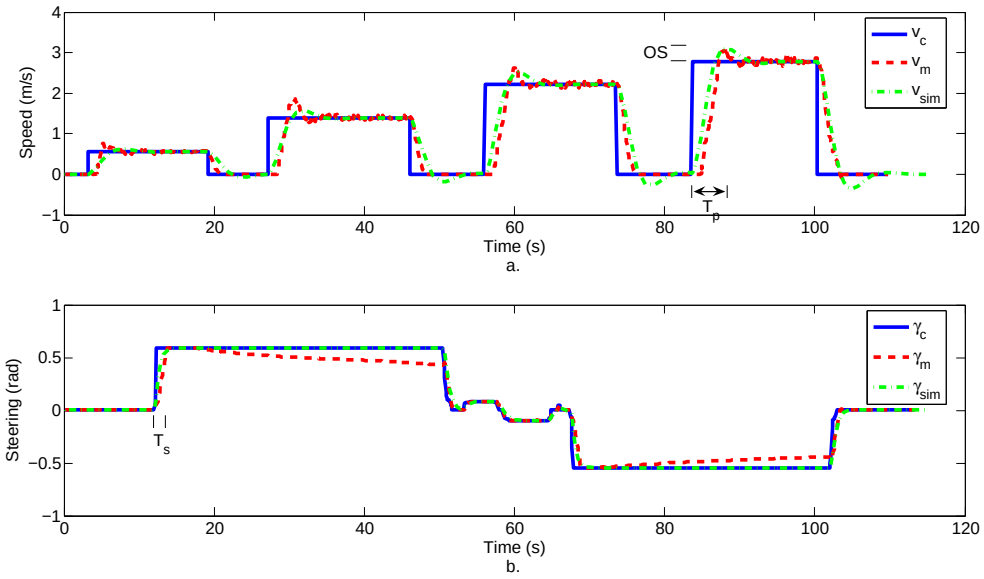

Figure 3.3: (a) Commanded speed, measured speed, and simulated speed output. (b) Commanded steering, measured steering, and simulated steering output.

The damping ratio and the natural frequency for the second-order system can be calculated from the percent overshoot, %OS, and the time-to-peak, T_p:

$$\zeta = \sqrt{\frac{\ln^2\left(\frac{\%OS}{100}\right)}{\pi^2 + \ln^2\left(\frac{\%OS}{100}\right)}},\ \omega_\mathrm{n} = \frac{\pi}{T_\mathrm{p}\sqrt{1-\zeta^2}}.$$

The time constant for the first-order system can be calculated from the settling time, T_s:

$$\tau_\gamma = \frac{T_\mathrm{s}}{4}.$$

From the experimental data, ζ, ω_n, and τ_γ, were found to be 0.55, 0.83 rad/s, and 0.45 s, respectively. This technique for modeling the throttle and steering dynamics worked

reasonably well as the same commanded speed and steering inputs produced similar simulated and measured outputs, as shown in Figure 3.3.

3.2 Camera Model

The goal of creating the camera model is to emulate the range and bearing measured by the camera, $(\rho_{\mathrm{m}}, \phi_{\mathrm{m}})$, using the positions and headings of a leader-follower pair, $(x_0, y_0, \theta_0, x, y, \theta)$. For the MATS vehicle, there is an offset, o_{c}, between the camera and the rear axle of the follower and an offset, o_{t}, between the target located on the back of the leader vehicle and its rear axle. As a result, the range and bearing to centre point of the camera, $(\rho_{\mathrm{c}}, \phi_{\mathrm{c}})$, is not the range and bearing between the rear axles of both vehicles, as depicted in Figure 3.4. From geometry, the camera's position, $(x_{\mathrm{c}}, y_{\mathrm{c}})$, and the target's position, $(x_{\mathrm{t}}, y_{\mathrm{t}})$, can be computed using

$$
\begin{aligned}
x_{\mathrm{c}} &= x + o_{\mathrm{c}} \cos\theta \\
y_{\mathrm{c}} &= y + o_{\mathrm{c}} \sin\theta \\
x_{\mathrm{t}} &= x_0 - o_{\mathrm{t}} \cos\theta_0 \\
y_{\mathrm{t}} &= y_0 - o_{\mathrm{t}} \sin\theta_0.
\end{aligned}
$$

Hence, given the camera and target offsets, the range and bearing to camera's centre point can be computed from the leader's and follower's positions and headings using

$$
\begin{aligned}
\rho_{\mathrm{c}} &= \sqrt{(x_{\mathrm{t}} - x_{\mathrm{c}})^2 + (y_{\mathrm{t}} - y_{\mathrm{c}})^2} \\
\phi_{\mathrm{c}} &= \operatorname{atan2}(y_{\mathrm{t}} - y_{\mathrm{c}}, x_{\mathrm{t}} - x_{\mathrm{c}}) - \theta.
\end{aligned}
$$

In addition to the camera and target offsets, the DefendIR 5000 camera used by the

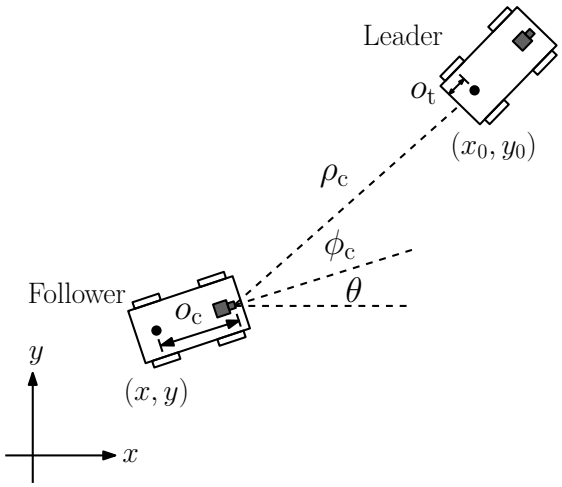

Figure 3.4: The range and bearing to centre point of the camera is not the range and bearing between the rear axles of both vehicles.

MATS vehicle has a lens offset created by the monocular camera being located left of the camera's centre, which is shown in Figure 3.5. This lens offset, o_l, causes the actual range and bearing to the camera's lens, (ρ_a, ϕ_a), to be different from the range and bearing to the camera's centre. However, the relationship behind the two ranges and bearings is easily derived using the diagram in Figure 3.5:

$$\rho_a = \sqrt{(\rho_c \cos\phi_c)^2 + (\rho_c \sin\phi_c - o_l)^2}$$

$$\phi_a = \text{atan2}(\rho_c \sin\phi_c - o_l, \rho_c \cos\phi_c).$$

Figure 3.5: DefendIR 5000 camera used by the MATS vehicle.

Finally, there are many sources of noise that affect the camera's range and bearing measurements, $(\rho_{\mathrm{m}}, \phi_{\mathrm{m}})$, e.g., vehicle vibration, road bumps, and lighting conditions. To test our system's robustness to the expected noise, we modeled the measured range and bearing as the actual range and bearing to the camera lens plus additive zero-mean white Gaussian noises:

$$\rho_{\mathrm{m}} = \rho_{\mathrm{a}} + n_{\rho}$$

$$\phi_{\mathrm{m}} = \phi_{\mathrm{a}} + n_{\phi},$$

where $n_{\rho} \sim N(0, \sigma_{\rho}^2)$ and $n_{\phi} \sim N(0, \sigma_{\phi}^2)$ are uncorrelated noises on the range and bearing with variances σ_{ρ}^2 and σ_{ϕ}^2, respectively. The variances were chosen based on comparing actual camera measurements from a test trial with the DGPS ground truth. An example is shown in Figure 3.6, where σ_{ρ}^2 is computed from the range error and σ_{ϕ}^2 is computed from the bearing error. For the example, $\sigma_{\rho}^2 = 0.18$ m^2 and $\sigma_{\phi}^2 = 8.3 \times 10^{-4}$ rad^2.

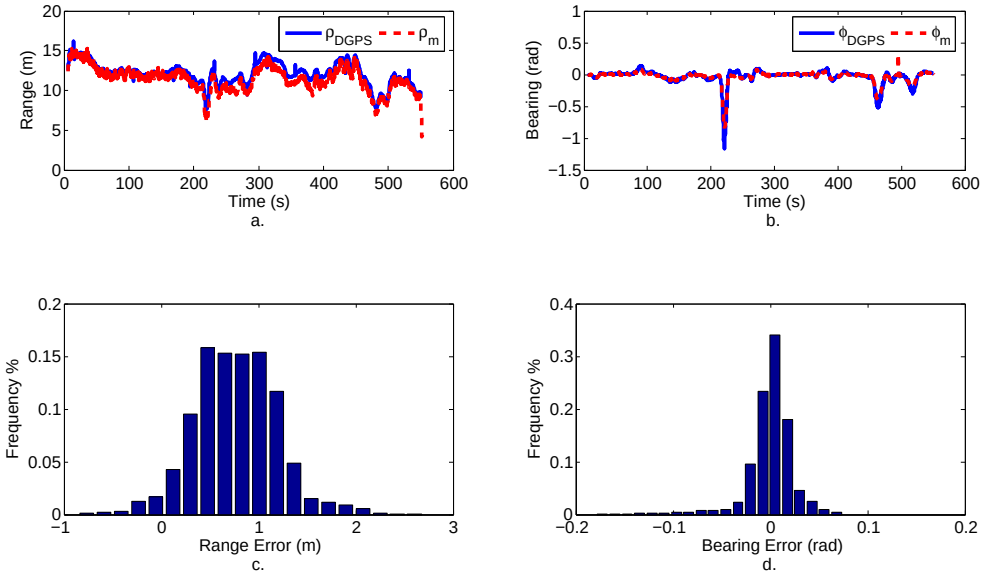

Figure 3.6: (a) Ranges from DGPS and camera measurements. (b) Bearings from DGPS and camera measurements. (c) Histogram of range error between DGPS and camera. (d) Histogram of bearing error between DGPS and camera.

In Figure 3.6c, where the range errors are shown, it is interesting to note that the

errors have a non-zero mean. This non-zero mean would later prove to be a source for non-zero longitudinal tracking errors in the experiments. It is also important to note that although the range and bearing errors may not actually be Gaussians as we have modeled, our goal was not to accurately model the noise, but to get a sense of its magnitude, so we could test the robustness of our design.

3.3 Encoder and Gyro Models

Similar to the camera measurements, the speed measurement from the wheel encoders and the heading measurement from the heading gyro are expected to be noisy. Thus, we also modeled these measurements as the actual values being corrupted with zero-mean white Gaussian noises:

$$v_{\mathrm{m}} = v + n_{\mathrm{v}}$$

$$\theta_{\mathrm{m}} = \theta + n_{\theta},$$

where $n_{\mathrm{v}} \sim N(0, \sigma_{\mathrm{v}}^2)$ and $n_{\phi} \sim N(0, \sigma_{\theta}^2)$ are uncorrelated noises on the speed and heading with variances σ_{v}^2 and σ_{θ}^2, respectively. Using the same approach as the camera model, we chose the speed and heading variances by comparing sample vehicle measurements with the DGPS ground truth. An example is shown in Figure 3.7, where σ_{v}^2 is computed from the speed error and σ_{θ}^2 is computed from the heading error. For the example, $\sigma_{\mathrm{v}}^2 = 0.0070$ m^2/s^2 and $\sigma_{\theta}^2 = 0.0055$ rad^2. It should be noted that accuracy of the heading gyro is probably higher than the accuracy of the DGPS heading. The reason is that the latter updates only at 1 Hz, while the vehicle-following system is expecting data at 4 Hz. As a result, the DGPS heading has a lag and seems 'jagged' around sharp turns. This problems is examined in more detail in Section 4.3.3. Hence, we do not have reliable ground truth for heading measurements; however, we still treat the DGPS heading as ground truth to remain consistent with the other measurements.

In light of the above fact, the variance of the actual heading noise is probably lower than 0.0055 rad^2. Nevertheless, simulating with higher noise levels only further validates the robustness of our design. It should also be noted that the above heading model represents a heading gyro with a magnetometer, which is employed by the gyro on the MATS vehicle. With the magnetometer on, the gyro's heading is corrected to magnetic north, thus preventing the measured heading from drifting from the true heading over time.

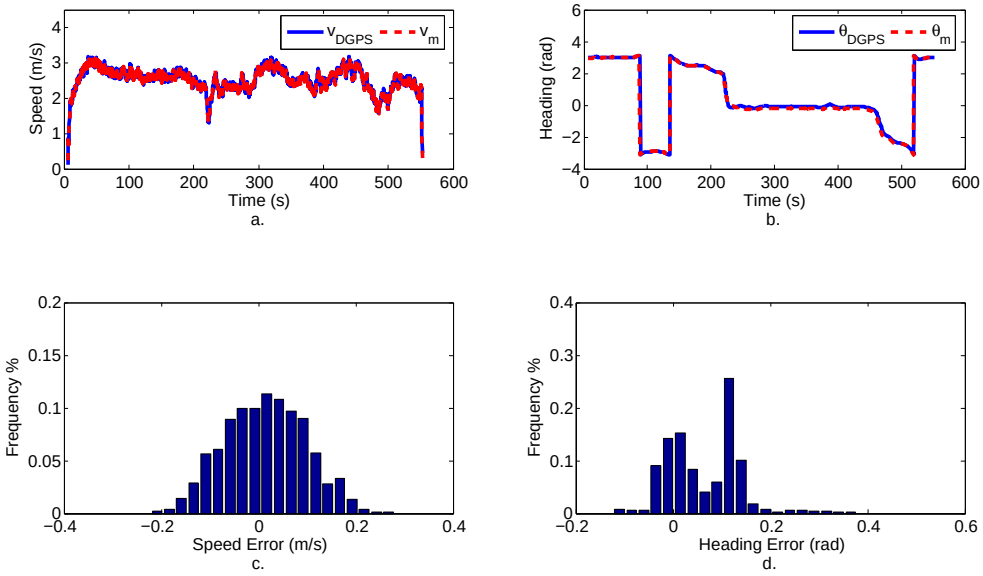

Figure 3.7: (a) Speeds from DGPS and encoder measurements. (b) Headings from DGPS and gyro measurements. (c) Histogram of speed error between DGPS and encoder. (d) Histogram of heading error between DGPS and gyro.

3.4 Software Implementation

The main vehicle code that operates the camera and communicates with the speed-and-steering control system, which drives and steers the MATS vehicle, is written in C++. To simplify the integration with the vehicle code, we implemented the nonlinear observer and controller in a single C++ class named `Controller`. The Controller class has two methods: `reset` and `update`. The reset method reads in and initializes the

class's configurable parameters such as the constant time delay, the look-ahead time, and the smoother-window size. The update method takes the sensor measurements as inputs and provides the commanded speed and steering as outputs. The following pseudocode shows the how the main vehicle uses the Controller class:

Create a new `Controller` instance

Call `reset`

while vehicle is running **do**

Read in camera, encoder, and gyro measurements

Call `update`

Apply commanded speed and steering to vehicle

end while

To integrate the Controller class with the simulation environment, we used a Simulink S-function. The S-function is a wrapper for code written in various programming languages, including C++, allowing the code to read inputs from and provide outputs to the Simulink environment. The simulation block diagram is updated to show the S-function in Figure 3.8. With this setup, we were able to test the exact same code that will be implemented on the MATS vehicle, thus reducing the possible sources of error during integration with the vehicle code.

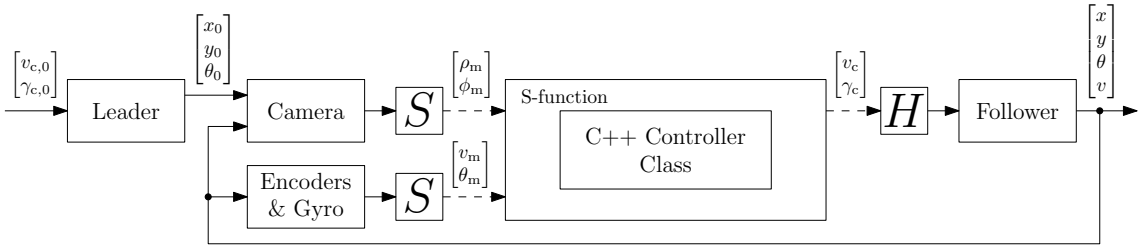

Figure 3.8: Simulation block diagram with C++ Controller class.

3.5 Review of System Parameters

Throughout Chapters 1, 2, and 3, important parameters for the vehicle-following system have been detailed and explained. This section summarizes these parameters, along with parameters that are needed for simulation. In Table 3.1, the configurable parameters are shown, along with values that were used in simulation trials. Note that the smoother and line-fitting window sizes were assumed to be same. Even though the line-fitting window may be smaller, we used the same sizes for the two windows in the simulations and experiments that we have conducted. The constant parameters for the vehicle-following system are shown in Table 3.2, and the parameters used only in simulations are shown in Table 3.3. Note that the discrete sampling period, T, is the period at which the `Controller` code's `update` method is called. Since the MATS vehicle's vehicle code runs at 4 Hz, T is set to 0.25 s.

Table 3.1: Configurable parameters for vehicle-following system, along with values that were used in simulation trials.

Description	**Symbol**	**Values Used**
Constant time delay	τ	6 s
Point-ahead controller pole locations		-0.2, -0.2
Length of point ahead	κ	5 m
Minimum commanded speed	$v_{\mathrm{c,min}}$	0.2 m/s
Decoupled controller longitudinal pole locations		-0.08, -0.08
Decoupled controller lateral pole locations		-0.24, -0.24, -0.24
Minimum estimated delayed leader's speed	$\hat{v}_{\mathrm{d,min}}$	1.2 m/s
Constant look-ahead time	l	1.75 s
Smoother/line fitting window sizes	n	8 s
Spline separation in smoother	q	2 s
Starting range threshold (to determine if leader has started moving)	ρ_{InitTol}	2 m
Stopping minimum range threshold ($d_{\mathrm{safe}} = \lambda_{\mathrm{safe}} v_{\mathrm{m}} \tau + \rho_{\mathrm{safe}}$)	ρ_{Safe}	3.5 m
Stopping percentage	λ_{Safe}	20%

Table 3.2: Constant parameters for vehicle-following system.

Description	**Symbol(s)**	**Value**
Discrete sampling period	T	0.25 s
Distance between MAT's front and rear axles	d	1.87 m
Offset between camera and rear axle	o_{c}	0.76 m
Offset between target and leader's rear axle	o_{t}	0.55 m
Offset between camera lens and vehicle centre	o_{l}	0.10 m

Table 3.3: Parameters used only in simulations.

Description	**Symbol**	**Value**
Noise variance on range	σ_ρ^2	0.18 m^2
Noise variance on bearing	σ_ϕ^2	8.3×10^{-4} rad^2
Noise variance on speed	σ_{v}^2	0.0070 $\mathrm{m}^2/\mathrm{s}^2$
Noise variance on heading	σ_θ^2	0.0055 rad^2
Natural frequency of throttle transfer function	ω_{n}	0.83 rad/s
Damping ratio of throttle transfer function	ζ	0.54
Time constant of steering transfer function	τ_γ	0.45 m

3.6 Simulations

In preparation for experimental field trials, we performed simulations with one and two followers to verify our design. We simulated a manually-driven lead vehicle by specifying its commanded speed and steering. The commanded speed was set to a constant 2 m/s (which is the expected MATS vehicle's speed during turns) for 200 s, and the commanded steering was chosen so that the lead vehicle makes a 90-degree left turn around the 100 s mark, as shown in Figure 3.9.

3.6.1 Smoother and Estimation Simulation Results

Figure 3.10 shows the results of the smoother. In Figure 3.10a, the measured range delayed by τ is shown with the estimated range, while in Figure 3.10b, the measured bearing delayed by τ is shown with the estimated bearing. The differences between the measured and estimated ranges and bearings are shown in Figure 3.10c and Figure 3.10d, respectively. Not surprisingly, the differences seem Gaussian since the measured range and

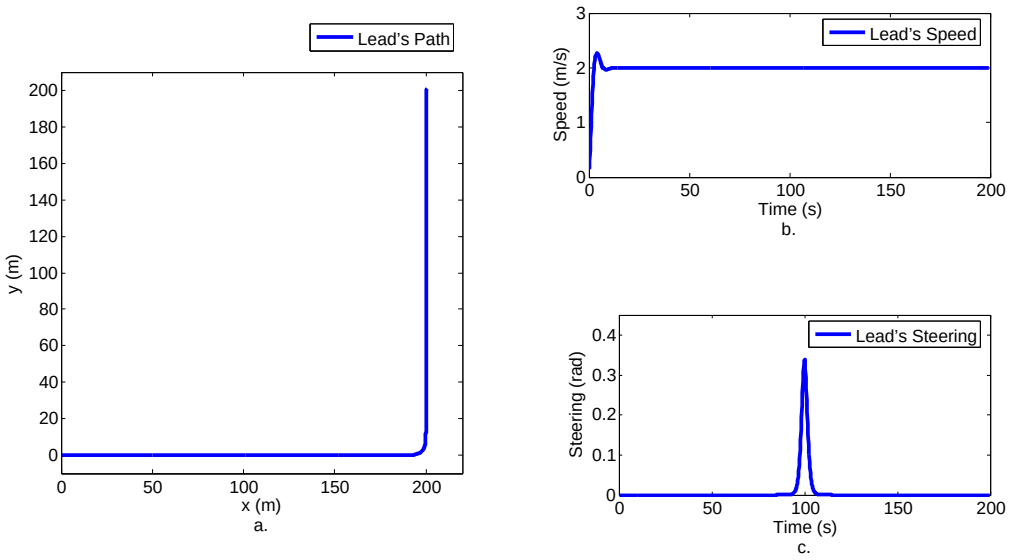

Figure 3.9: Simulation test setup: (a) Lead vehicle's path. (b) Lead vehicle's speed. (c) Lead vehicle's steering.

bearing values are modeled as the actual values corrupted with zero-mean white Gaussian noises. The variances of the differences are 0.17 m^2 and 0.0011 rad^2, respectively, compared with injected noise variances of 0.18 m^2 and 8.3×10^{-4} rad^2.

Figure 3.11 shows the results of the line fitter that estimates the delayed leader's speed and heading. In Figure 3.11a, the delayed leader's actual and estimated speeds are shown, while in Figure 3.11b, the delayed leader's actual and estimated headings are shown. The error between the actual and estimated speeds and headings are shown in Figure 3.11c and Figure 3.11d, respectively. For the most part, the errors are close to zero, but may be large on occasion due to the simulated additive noise and difficulties in estimation as the leader turns.

3.6.2 Point-ahead Controller Simulations

For the point-ahead controller, the configurable parameters are the length of the point ahead, κ, and the locations of the closed-loop poles, which determines the controller gains, (k_p, k_i). At first pass, a natural choice for the point-ahead's length would be the

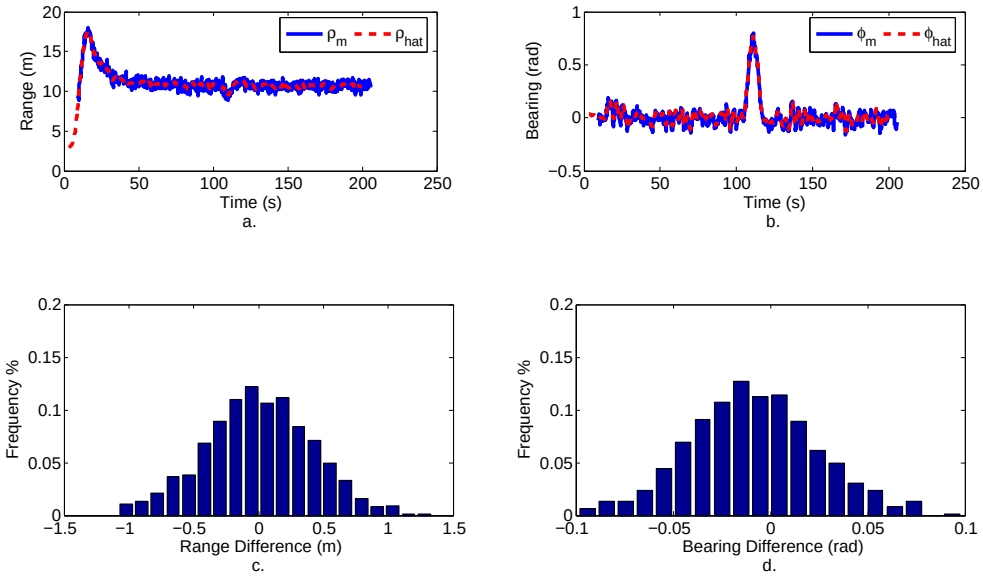

Figure 3.10: (a) Simulated ranges from camera measurement and from smoother. (b) Simulated bearings from camera measurement and from smoother. (c) Histogram of range difference between camera and smoother. (d) Histogram of bearing difference between camera and smoother.

length of the wheelbase, $d = 1.87$ m. However, that length seems to cause oscillatory steering behaviour as shown in Figure 3.12. The reason is that the commanded steering is inversely related to the length of the point ahead.

For closed-loop pole locations, we chose to place both poles at the same location on the negative real axis and moved the poles as far left as possible before we see oscillatory behaviour with the commanded speed. Note that oscillatory effects will occur first in the speed because the transfer function fitted to the throttle has a much lower bandwidth than the transfer function fitted to the steering. Furthermore, oscillatory effects on steering may be reduced by increasing κ. Also note that with this pole-placement method, any subsequent followers would use the same gains as the first follower since higher gains are not stable and lower gains would result in worse tracking.

Using the pole-placement technique, we found poles at -0.2 ($k_\mathrm{p} = 0.4$ s^{-1}, $k_\mathrm{i} = 0.04$ s^{-1}) to be the limit before large oscillatory speed behaviour. Plots for this test case, with $\kappa = 5$ m, are shown in Figure 3.13. Note that the large lateral error during the

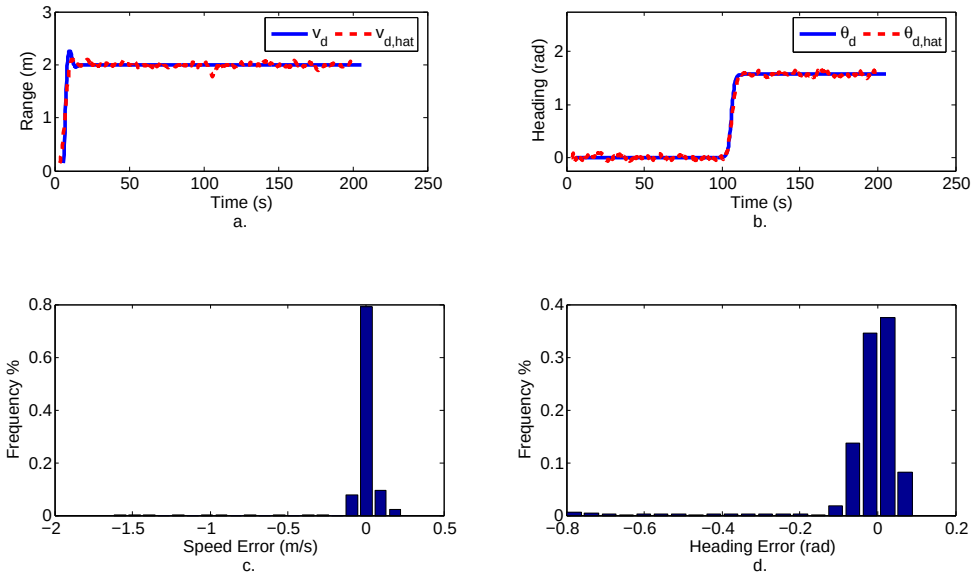

Figure 3.11: (a) Simulated delayed leader's actual and estimated speeds. (b) Simulated delayed leader's actual and estimated headings. (c) Histogram of error between actual and estimated speeds. (d) Histogram of error between actual and estimated headings.

turn (after 100 s) in Figure 3.13b suggests that the gains are low. However, we see that there are already minor oscillatory effects in the speeds in Figure 3.13c, which suggests that the gains are high. These contradictory indicators show the limitations of having coupled speed and steering commands.

A method to possibly reduce the large lateral error during the 90-degree turn is to have separate lengths for the leader's and follower's points ahead. The rationale is with a shorter leader's point ahead, the follower would turn earlier. The tradeoff would be a constant longitudinal error equal to the difference between the lengths of the points ahead. However, this strategy is only mildly successful as shown by Figure 3.14, where the length of the follower's point ahead, κ_f, is set to 5 m and the length of its leader's point ahead, κ_l, is set to 0 m. Although follower 1's lateral error during the turn has been reduced, the follower 2's lateral error is still very large. Note that follower 2's lateral error is with respect to the lead vehicle's path not follower 1's path. Evidently, the point-ahead controller is unlikely to yield good tracking results. Hence, we developed the decoupled controller.

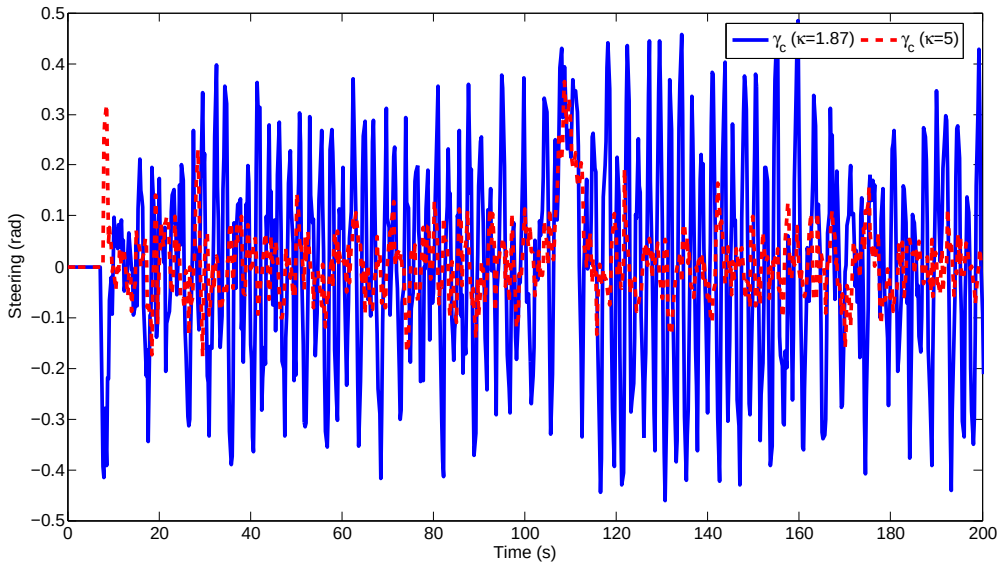

Figure 3.12: Commanded steering values for $\kappa = 1.87$ m and $\kappa = 5$ m using point-ahead controller.

3.6.3 Decoupled Controller Simulations

For the decoupled controller, the configurable parameters are the locations of the closed-loop poles and the length of the look-ahead time. Again, we chose to place the closed-loop poles at the same location on the negative real axis and move them left until speed or steering oscillations occurred. However, this time, the longitudinal poles are placed separately from the lateral poles. Using this method, the optimal longitudinal poles were found to be -0.08 and the optimal lateral poles were found to be -0.24. The corresponding longitudinal gains are $k_{\mathrm{p},1} = 0.16$ s^{-1} and $k_{\mathrm{i},1} = 0.0064$ s^{-1}, and the corresponding lateral gains at $v_{\mathrm{d}} = 2$ m/s are $k_{\mathrm{p},2} = 0.081$ s^{-1}, $k_{\mathrm{i},2} = 0.0065$ s^{-1}, and $k_{\mathrm{p},3} = 0.67$.

The results for the above test case, with the look-ahead time, l, equals 0, are much better than those of the point-ahead controller and are shown in Figure 3.15 and Figure 3.16. Figure 3.15a shows the paths of the lead vehicle and the two followers, and Figure 3.15b shows a close-up of the paths around the turn. The longitudinal and lateral tracking errors are shown in Figure 3.16a and Figure 3.16b, and the actual speeds

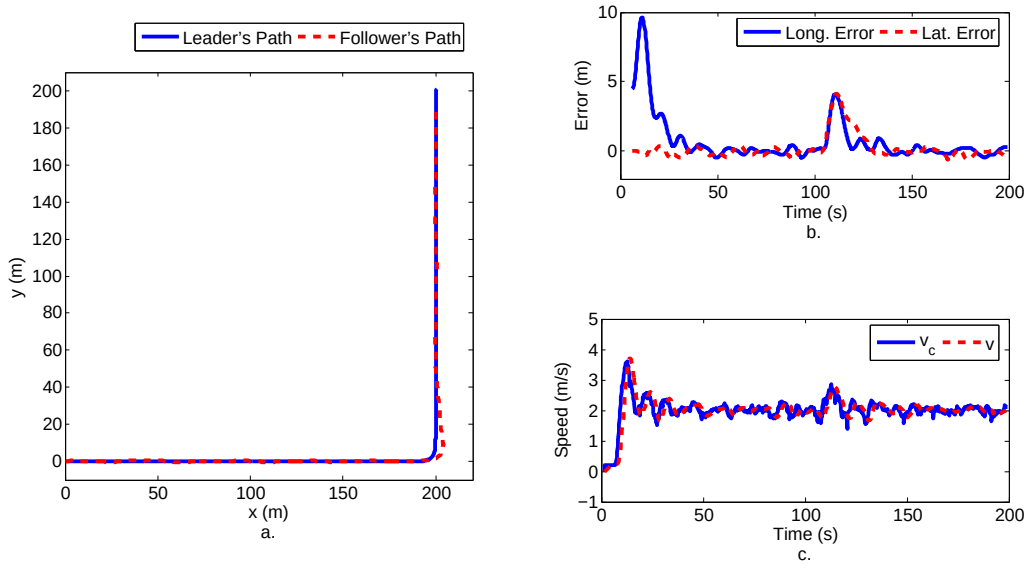

Figure 3.13: Point-ahead controller with poles at -0.2: (a) Leader's and follower's paths. (b) Follower's longitudinal and lateral tracking errors. (c) Follower's commanded and actual speeds.

and steering for both followers are shown in Figure 3.16c and Figure 3.16d. Notice in Figure 3.16b that the lateral errors of both followers are 'larger' in the positive direction than the negative direction during the turn. This can be compensated for by specifying a positive look-ahead time.

Through experimentation, the best look-ahead time was found to be 1.75 s. The results for this test case is shown in Figure 3.17. Notice that the lateral errors in Figure 3.17c are more evenly distributed during the turn.

For our experimental field trials, the MATS vehicle's maximum allowable speed during autonomous operations is expected to be 4.2 m/s. To validate that our design works for this speed, a simulation of the same path with the lead vehicle's speed increased to 4.2 m/s was conducted. The results of that this test case are shown in Figure 3.18 and Figure 3.19. Even at 4.2 m/s around the turn, the maximum absolute lateral for the second follower in Figure 3.18b is around only 2 m. Given these results, we were confident that our vehicle-following system would work on the MATS vehicle.

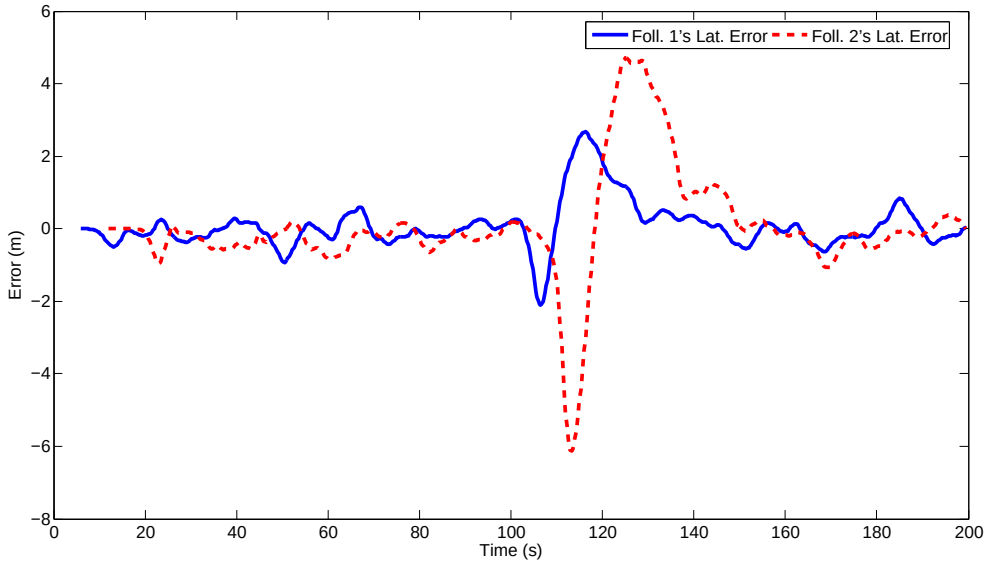

Figure 3.14: Follower 1's and follower 2's lateral errors using point-ahead controller with poles at -0.2 and $\kappa_{\mathrm{f}} = 5$ m and $\kappa_{\mathrm{l}} = 0$ m.

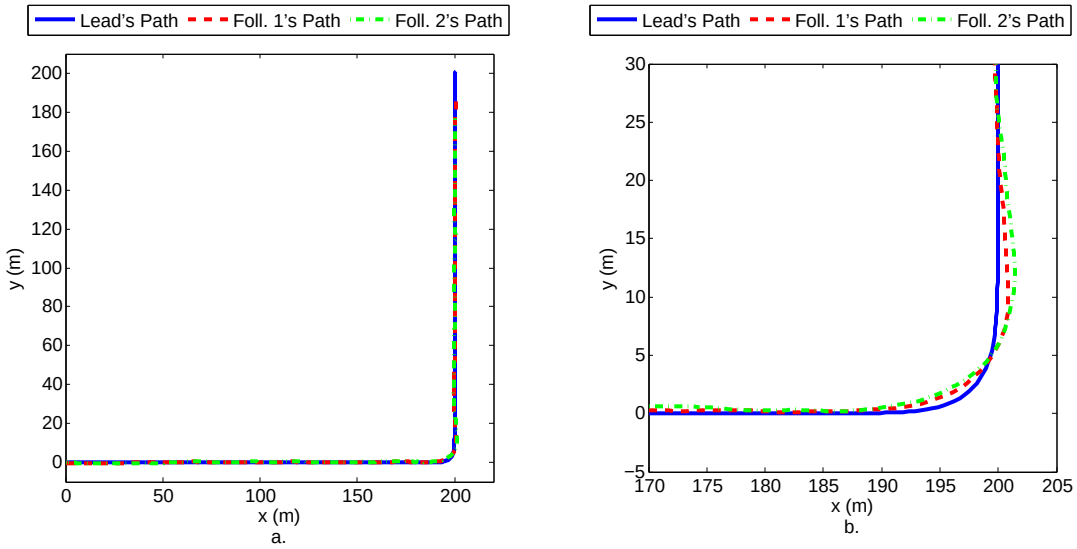

Figure 3.15: Decoupled controller with longitudinal poles at -0.08 and lateral poles at -0.24 and look-ahead time of 0 s: (a) Lead vehicle's, follower 1's, and follower 2's paths. (b) Close-up of the paths around the turn.

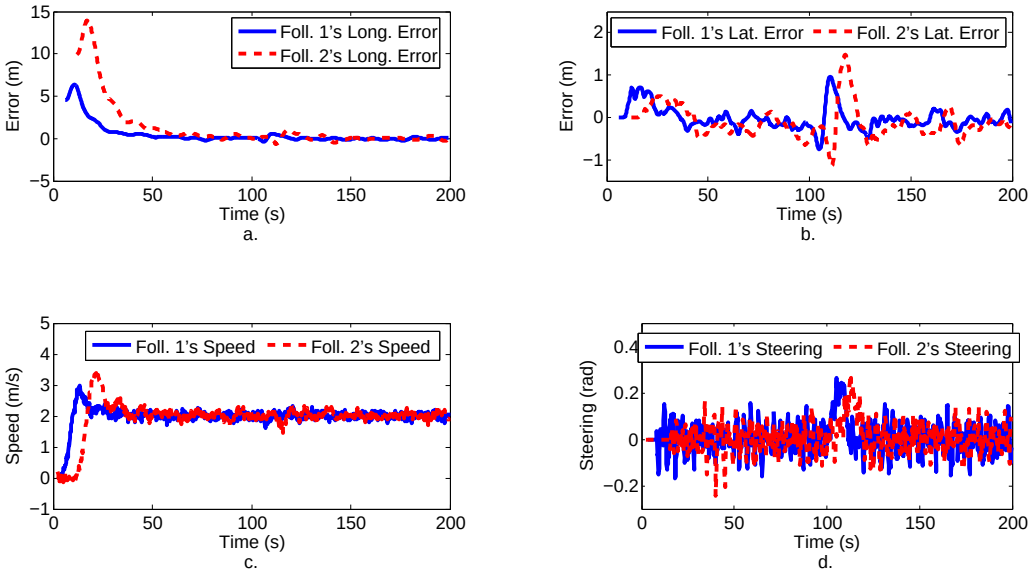

Figure 3.16: Decoupled controller with longitudinal poles at -0.08 and lateral poles at -0.24 and look-ahead time of 0 s: (a) Follower 1's and follower 2's longitudinal errors. (b) Follower 1's and follower 2's Lateral errors. (c) Follower 1's and follower 2's speeds. (d) Follower 1's and follower 2's steering.

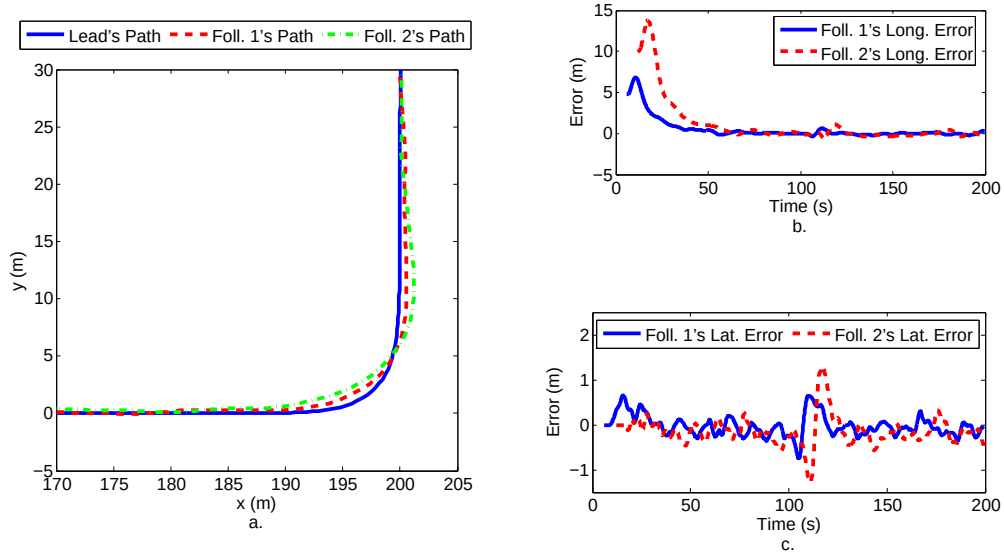

Figure 3.17: Decoupled controller with longitudinal poles at -0.08 and lateral poles at -0.24 and look-ahead time of 1.75 s: (a) Close-up of the paths around the turn. (b) Follower 1's and follower 2's longitudinal errors. (c) Follower 1's and follower 2's Lateral errors.

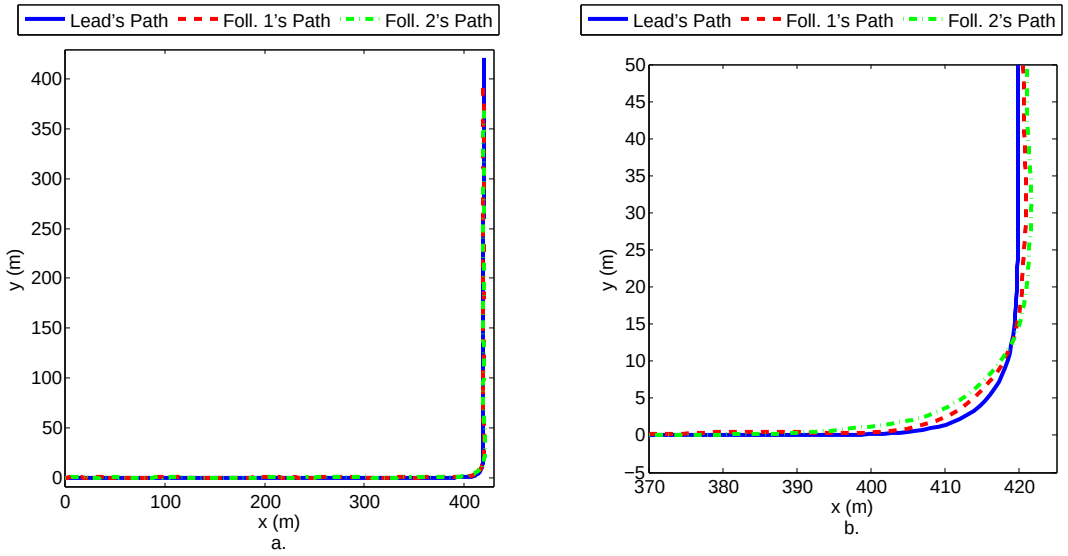

Figure 3.18: Lead vehicle traveling at 4.2 m/s and followers using decoupled controller with a look-ahead time of 1.75 s: (a) Leader's, follower 1's, and follower 2's paths. (b) Close-up of the paths around the turn.

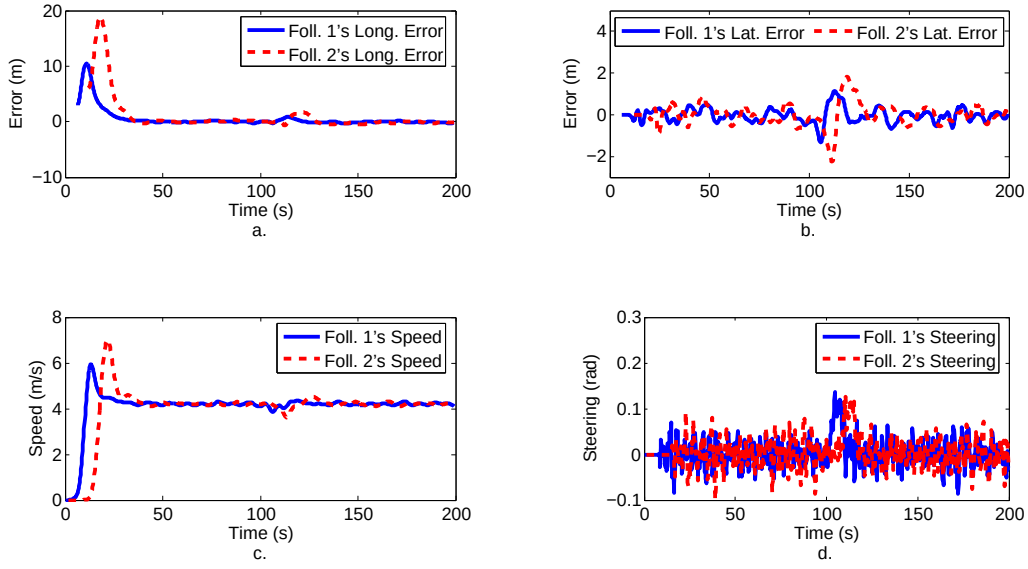

Figure 3.19: Lead vehicle traveling at 4.2 m/s and followers using decoupled controller with a look-ahead time of 1.75 s: (a) Follower 1's and follower 2's longitudinal errors. (b) Follower 1's and follower 2's Lateral errors. (c) Follower 1's and follower 2's speeds. (d) Follower 1's and follower 2's steering.

Chapter 4

Experimental Field Trials

Experimental field trials were conducted during the periods of November 17$^{\text{th}}$–28$^{\text{th}}$, 2008, and May 25$^{\text{th}}$–June 4$^{\text{th}}$, 2009, at the DRDC Suffield Experimental Proving Ground in Suffield, Alberta, Canada. The main test track used for the experiments is shown in Figure 4.1. The test track is a gravel road, 1.3 km long, approximately 7 m wide, and the most difficult portions of the track are the hairpin and U-turn. The test track is also slightly crowned with noticeable side slopes near its edges. The U-turn, which predominantly slopes inwards along the track, proved to be the most difficult for the final version of our vehicle-following system.

Figure 4.1: Test track for experimental field trials.

A picture of a leader MATS vehicle used in the experimental trials is shown in Fig-

ure 4.2. The red-coloured target is used by a follower's camera system to measure the range and bearing to the leader. Each MATS vehicle is equipped with an on-board computer, a pan-tilt-zoom monocular camera, a GPS antenna, and a data link to a ground station to receive DGPS corrections. The DGPS has an accuracy of about 0.05 m and serves to provide ground truth for the trials.

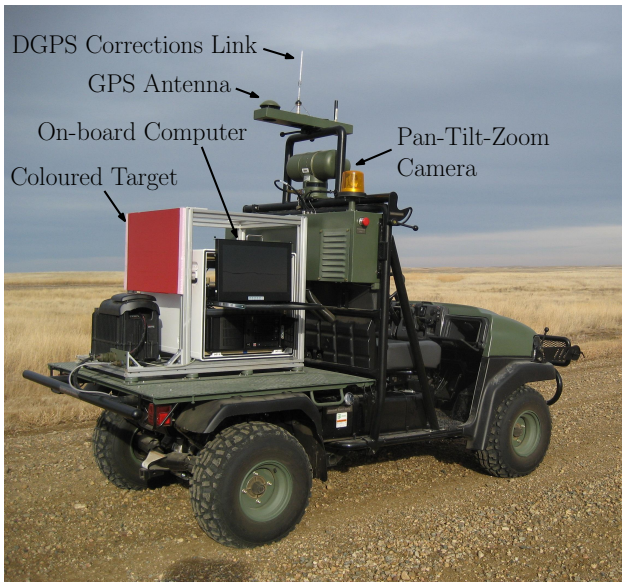

Figure 4.2: A leader MATS vehicle.

4.1 Camera Limitations

One of the main limitations of our implementation is that a follower relies solely on one camera to obtain the range and bearing to its immediate leader. Consequently, if the camera were to fail, then the follower would lose tracking of its leader. Through the trials, we discovered two main sources of camera failure: lighting and road dust.

To track a target, the camera uses colour segmentation, a technique that is described in detail in [15] and [16]. As a result, for the camera to track successfully, the target's colour properties (e.g., brightness and distinctness from its surroundings) should remain relatively consistent throughout a trial run. However, if the sun is low in the sky, the

target may look different when the camera is facing away from the sun and facing into the sun. This difference is enough to cause the camera to lose tracking and is unavoidable with a low sun on a circular test track. When the camera loses the target, it sends consecutive dropouts to the vehicle-following system, eventually causing the system to fail. To minimize the chance of camera failure due to lighting, trials around the test track were conducted when the sun was higher in the sky or during cloudy days.

Because the test track is a gravel road, dust may kick up behind a leader vehicle and obscure its target, causing its follower's camera to lose tracking. An example is shown in Figure 4.3 where dust is kicked up by the two leader vehicles, partially obscuring their targets. To alleviate this problem, the manually-driven lead vehicle is driven more slowly on dusty portions of the road, thus causing less dust to kick up and decreasing the inter-vehicle distance, which further helps the camera tracking.

Figure 4.3: Dust is kicked up by the two leader vehicles, partially obscuring their targets.

4.2 Nonlinear Observer Results

As discussed in Section 2.5.3, the nonlinear observer produces estimates of a follower's and its delayed leader's positions and headings, along with an estimate of the delayed leader's speed. The follower's position and heading are estimated using dead reckoning, and the delayed leader's position, heading, and speed are estimated by combining the follower's position and heading estimates with the camera measurements.

4.2.1 Dead Reckoning

During the November 2008 trials, the follower's position and heading were estimated using its speed and steering measurements as inputs. However, on the MATS vehicle, the encoder that measures the steering angle is located on the steering column. Since there is significant play between the steering column and the front wheels, the measured steering angle does not accurately represent the direction of the front wheels, especially on sloped roads. This causes the vehicle's heading estimated from the steering measurement to be highly inaccurate. Figure 4.4 shows the results of using the steering measurement to estimate the follower's heading and, subsequently, the follower's path. In the figure, the follower is going straight on the right side of a crowned road, which causes the steering measurement to indicate the follower is veering left (since the steering wheel must turn left to compensate for the road slope). As a result, the estimated heading and path shows the follower driving a circle instead of driving straight.

To solve this problem, we added a heading gyro to the MATS vehicle in preparation for the May/June 2009 trials. The heading gyro measures the vehicle's turning rate, which is integrated to estimate the vehicle's heading. The gyro also contains a magnetometer, which corrects the estimated heading to magnetic north, preventing the heading from drifting from the true heading over time. Figure 4.5 shows the results of dead reckoning with the gyro's heading to estimate the follower's path around the test track. Clearly, the

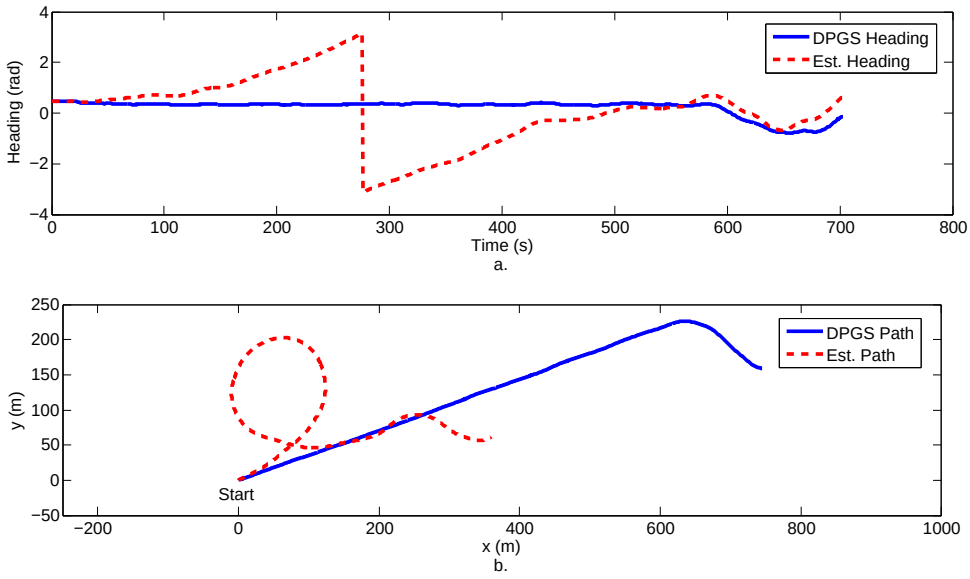

Figure 4.4: (a) Follower's DGPS heading and estimated heading using steering measurements. (b) Follower's DGPS path and estimated path using dead reckoning with steering measurements.

results are much better than the path estimate using the steering measurements. With this setup, we were able to successfully conduct field trials using only on-board sensors for feedback (i.e., no GPS for feedback).

4.2.2 Smoother and Line-fitting Window Results

Similar to the simulated results, the smoother and line-fitting window worked well in the experiments. Figure 4.6 shows a typical plot of the range and bearing from the camera versus the range and bearing from the smoother. Although there are dropouts (indicated by 1000 m and π rad for the range and bearing, respectively, by the camera), the smoother is able to ignore them. It is also interesting to note the two outliers shown in Figure 4.6b; the smoother is able to ignore the first, at the 250 s mark, since it is outside a configurable tolerance for valid bearing measurements (set to $\frac{\pi}{2}$ rad for the trials), but the smoother is not able to ignore the second outlier, at the 300 s mark, since it is within the tolerance for valid measurements. However, since the smoother uses a window of measurements, the effect of the second outlier is minimal.

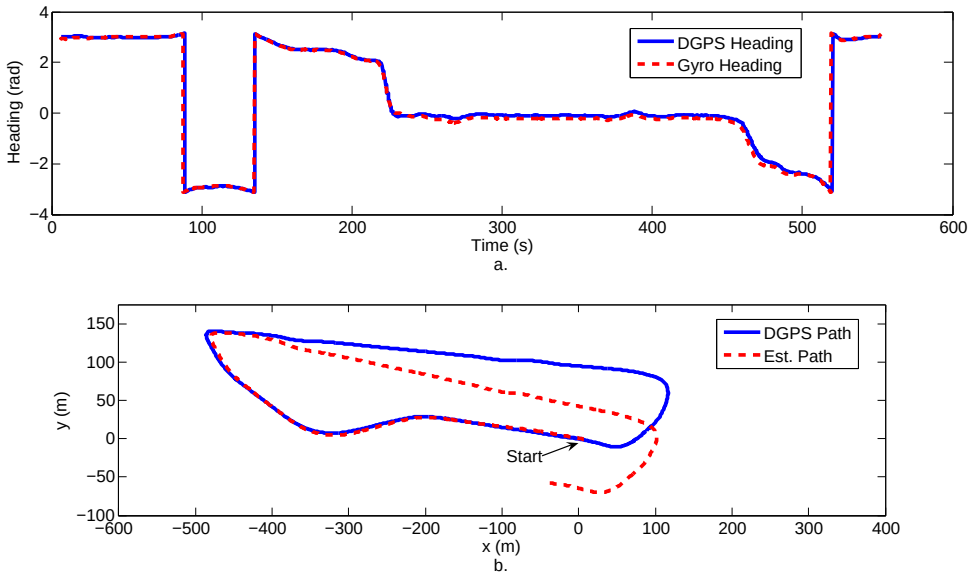

Figure 4.5: (a) Follower's DGPS heading and gyro heading. (b) Follower's DGPS path and estimated path created from dead reckoning with gyro heading.

Figure 4.7 shows a typical plot of delayed leader's DGPS and estimated speeds and headings. As is evident from Figure 4.7c and Figure 4.7d, estimating the speed and heading using line-fitting windows works reasonably well.

4.3 November 17th–28th, 2008, Trials

At the time of the November 2008 field trials, our vehicle-following system was still in development; the decoupled controller was implemented only half-way through the trials, the pole-placement technique had not been considered for tuning the controller gains, and the heading gyro had not been installed. The controller gains were tuned experimentally using the same idea of increasing the gains until oscillatory behaviour occurs. Given the poor path estimate from dead reckoning with steering measurements, we decided to use the DGPS to measure the follower's position and heading instead. Although using DGPS is not our project goal, this setup allowed us to field test the other components of our design, i.e., the smoother, the delayed-leader estimations, and the point-ahead and decoupled controllers. Note that the speed limit for the MATS vehicle in autonomous

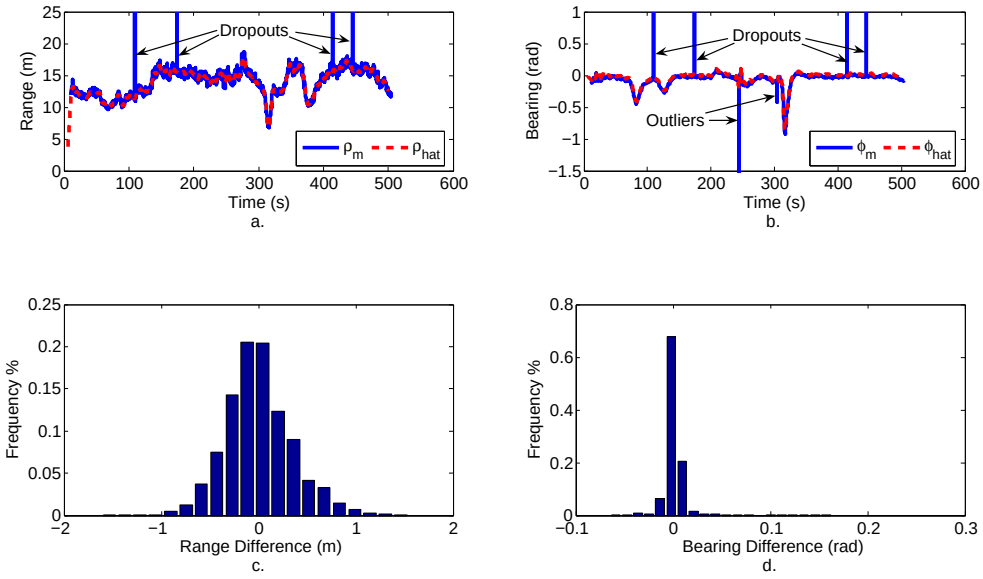

Figure 4.6: (a) Range measurement from camera and estimated range from smoother. (b) Bearing measurement from camera and estimated bearing from smoother. (c) Histogram of range difference between camera and smoother. (d) Histogram of bearing difference between camera and smoother.

operation was set to 2.8 m/s for these trials.

4.3.1 Point-ahead Controller

Similar to the simulations, experiments with the point-ahead controller validated its poor-tracking performance due to its coupled speed and steering gains. Figure 4.8 shows the best trial run with the point-ahead controller in which the manually-driven leader is moving side-to-side on a straight path at about 1.5 m/s. As is evident in Figure 4.8b, the follower's longitudinal error is starting to oscillate, implying the gains are high; however, the lateral error is still large, suggesting the gains are low.

The controller parameters for this trial are shown in Table 4.1. We used a time delay of 8 s, instead of the 6 s used in simulation, because at this stage of the trials, the vehicles were going fairly slowly; hence, we needed a larger time delay to achieve a larger inter-vehicle distance as a safety precaution. It is interesting to note that the gains used ($k_\mathrm{p} = 0.12$ s^{-1}, $k_\mathrm{i} = 0.02$ s^{-1}) are lower than the gains found in simulation ($k_\mathrm{p} = 0.4$ s^{-1},

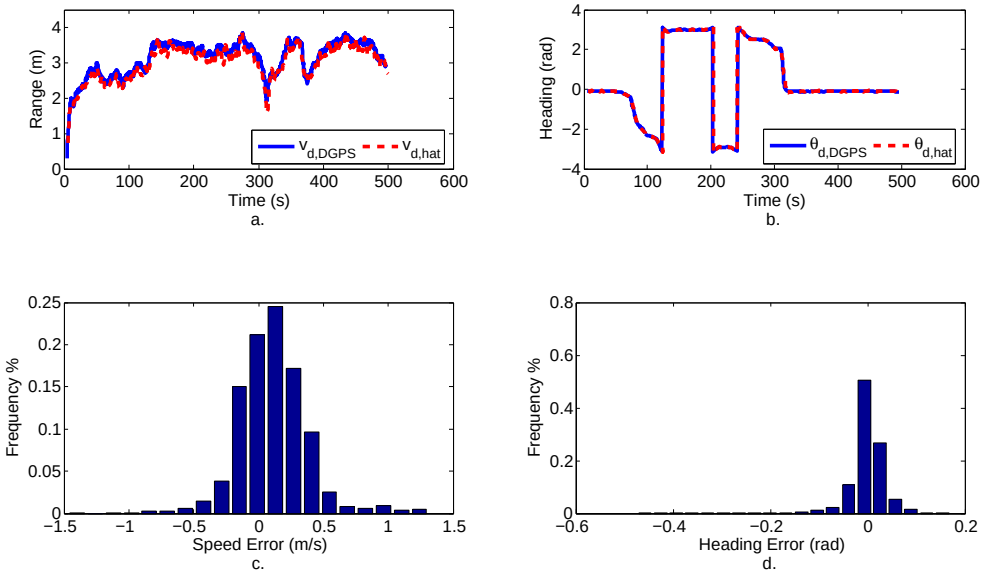

Figure 4.7: (a) Delayed leader's DGPS and estimated speeds. (b) Delayed leader's DGPS and estimated headings. (c) Histogram of error between DGPS and estimated speeds. (d) Histogram of error between DGPS and estimated headings.

$k_\mathrm{i} = 0.04\ \mathrm{s}^{-1}$). The reason for the lower gains is explained is Section 4.3.3.

Table 4.1: Parameters for best point-ahead controller trial.

Description	**Symbol**	**Value**
Time delay	τ	8 s
Proportional gain	k_p	$0.12\ \mathrm{s}^{-1}$
Integral gain	k_i	$0.02\ \mathrm{s}^{-1}$
Length of follower's point ahead	l_f	5 m
Length of leader's point ahead	l_l	3 m

4.3.2 Decoupled Controller

The decoupled controller was implemented midway through the trials after the point-ahead controller proved ineffective. However, the implemented controller is slightly different from the controller detailed in Section 2.3, which was the controller tested in the May/June 2009 trials. The differences are in the use of the look-ahead feature and the definition of the tracking error that is fed back to the controller. Furthermore, adding gain scheduling and integral terms to the control laws had not been considered.

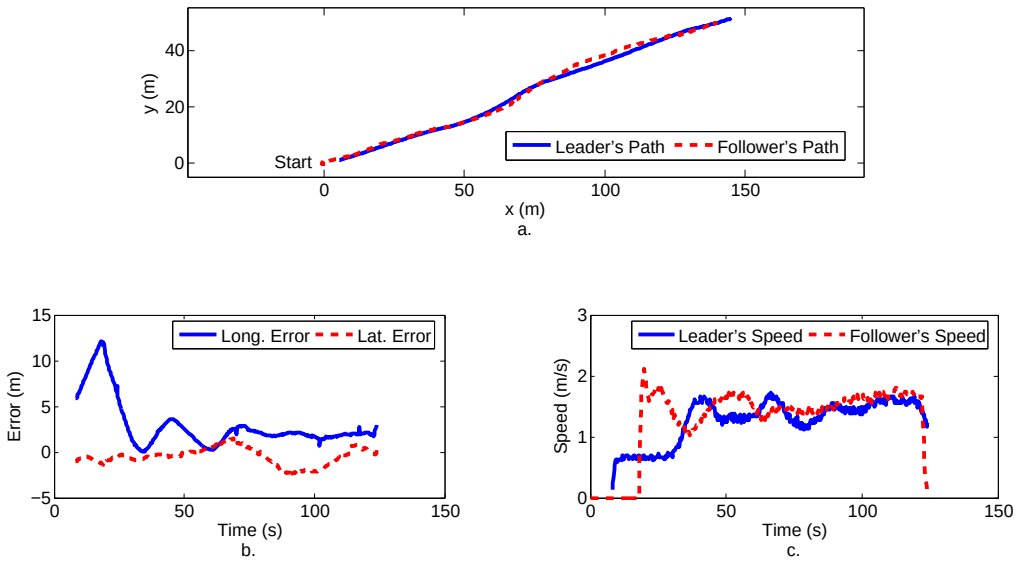

Figure 4.8: Best trial run with point-ahead controller: (a) Leader's and follower's paths. (b) Longitudinal and lateral tracking errors. (c) Leader's and follower's speeds.

For this first version of the decoupled controller, the tracking error that is fed back, (e_1, e_2), is defined to be

$$\begin{bmatrix} e_1 \\ e_2 \end{bmatrix} := \begin{bmatrix} \cos\theta & \sin\theta \\ -\sin\theta & \cos\theta \end{bmatrix} \begin{bmatrix} x_\mathrm{d} - x \\ y_\mathrm{d} - y \end{bmatrix}.$$

This defines the tracking error in the follower's frame instead of the delayed leader's frame since the rotation matrix uses θ instead of θ_d. We later decided to change to the delayed leader's frame since defining the error with respect to the reference vehicle (in this case the delayed leader) is more standard; however, the controller implemented for the November trials used the above definition. The difference between the follower's and delayed leader's frames is shown in Figure 4.9.

The other difference between this first-version decoupled controller from the one described in Section 2.3 is that, in this version, the lateral tracking error, e_2, is calculated from the look-ahead point. Hence, when a positive look-ahead time, l, is specified, e_2 is

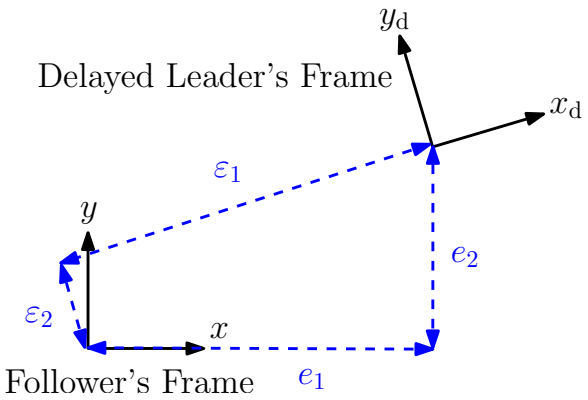

Figure 4.9: Tracking errors in the follower's frame, (e_1, e_2), compared with tracking errors in the delayed leader's frame, $(\varepsilon_1, \varepsilon_2)$.

calculated as

$$e_2 = -(x_l - x)\sin\theta + (y_l - y)\cos\theta,$$

where (x_l, y_l) is the look-ahead point. In the later version of the decoupled controller, only the heading error is calculated from the look-ahead point. The rationale for the change is that we wanted to regulate the lateral error to the delayed leader to zero, not the lateral error to the look-ahead point. However, calculating e_2 from the look-ahead point allows the follower to turn even earlier, which was helpful with this controller version, where the gains were quite low.

Again, using the method of manually increasing the gains until speed or steering oscillations are visible, the parameters in Table 4.2 were found to work well for this decoupled-controller version. Note that the gains used, ($k_{p,1} = 0.08$ s^{-1}, $k_{p,2} = 0.04$ s^{-1}, $k_{p,3} = 0.04$), are again lower than the gains used in simulations, ($k_{p,1} = 0.16$ s^{-1}, $k_{p,2} = 0.081$ s^{-1}, $k_{p,3} = 0.67$) with $v_d = 2$ m/s. The main reason for the lower gains is explained is Section 4.3.3. With the setup shown in Table 4.2, one follower was able to successfully track its manually-driven leader for 10 laps of the 1.3 km test track. A summary of the test results is shown in Table 4.3. The mean follower speed for the entire traverse was 2.2 m/s, and the mean following distance was 18.9 m. The mean lateral error was 0.07 m with a standard deviation of 0.46 m. The maximum absolute lateral error was

2.73 m, which occurred during one of the turns at the hairpin. Since it is more natural to calculate an error with respect to the reference, the tracking errors here are calculated in the delayed leader's frame.

Table 4.2: Parameters for best first-version decoupled controller trial.

Description	**Symbol**	**Value**
Time delay	τ	8 s
Look-ahead time	l	3 s
Proportional longitudinal gain	$k_{\mathrm{p},1}$	0.08 s^{-1}
Proportional lateral gain	$k_{\mathrm{p},2}$	0.04 s^{-1}
Proportional heading gain	$k_{\mathrm{p},3}$	0.04

Figure 4.10 shows ground truth plots for a typical lap for the 10-lap run. Figure 4.10a shows the leader's and follower's paths, while a close-up of the hairpin turn is shown in Fig. 4.10b. The longitudinal and lateral errors in the delayed leader's frame are shown in Fig. 4.10c. The large error increases around the 50 s and 400 s marks correspond to the U-turn and the hairpin turn, respectively. The large longitudinal error increase at the hairpin was later found to be largely contributed by the speed-and-steering controller, which limits the vehicle speed to be around 1 m/s around sharp turns. This discovery was made during the May/June 2009 trials. In Fig. 4.10d, the delayed leader's speed is compared with the follower's speed. Although the speed profiles are similar, the follower's speed is always higher than the delayed leader's speed. The reason for this is that the

Table 4.3: Test results for 10 laps around 1.3 km test track with first-version decoupled controller.

Description	**Symbol**	**Value**
Mean Follower Speed	v	2.2 m/s
Maximum Follower Speed	$\max_t v$	2.8 m/s
Minimum Following Distance		5.8 m
Mean Following Distance		18.9 m
Maximum Following Distance		26.0 m
Mean Lateral Error±Standard Deviation	$\frac{1}{t_\mathrm{f}} \int_0^{t_\mathrm{f}} \varepsilon_2(q) dq$	0.07 ± 0.46 m
Maximum Absolute Lateral Error	$\max_t \lvert\varepsilon_2(t)\rvert$	2.73 m

longitudinal error was always positive and our control law is $v_c = v_d + k_{p,1}e_1$. Evidently, from Fig. 4.10c., having a follower's speed that is higher than the delayed leader's speed does not guarantee the longitudinal error will go to zero since the follower may deviate from the leader's path.

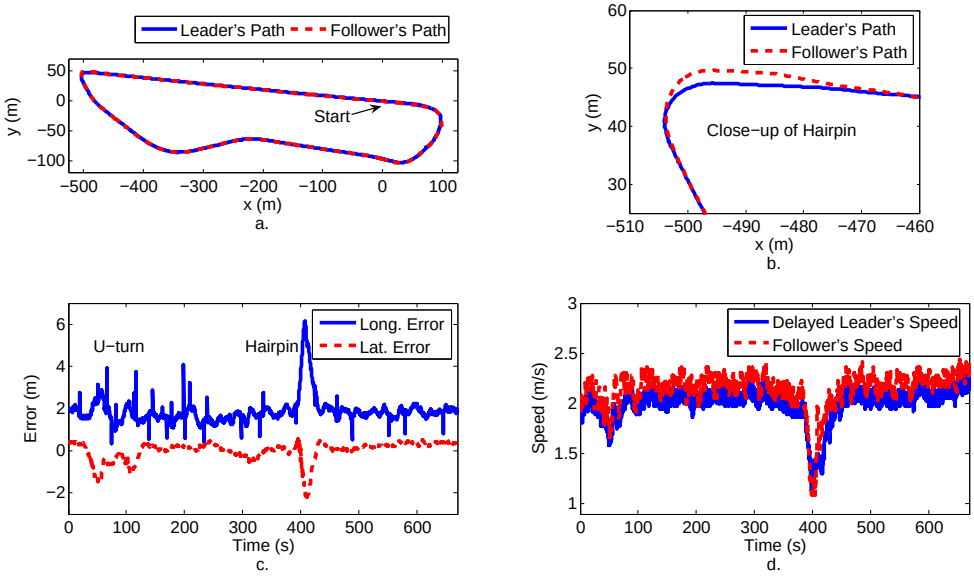

Figure 4.10: Typical lap for first-version decoupled controller: (a) Leader's and follower's paths. (b) Close-up of hairpin turn. (c) Longitudinal and lateral tracking errors. (d) Delayed leader's and follower's speeds.

4.3.3 Problem with DGPS Heading

The main reason for the low gains used in these trials was the DGPS heading, which updates at only 1 Hz. In contrast, our vehicle-following system was running at 4 Hz during the field trials. As a result, the DGPS heading seems jagged around sharp turns, such as the hairpin, as shown in Figure 4.11b. Since the delayed leader's path is estimated using this heading, the estimated path after the turn is 'zigzaggy' as shown Figure 4.11a. In this situation, if the controller gains are too high, the steering will oscillate while attempting to track the zigzag path. The DGPS heading may be filtered to alleviate the zigzag path estimates; however, filtering adds more lag to the heading, which creates a path estimate that is wide of the actual path. An example is given in Section 4.4.5.

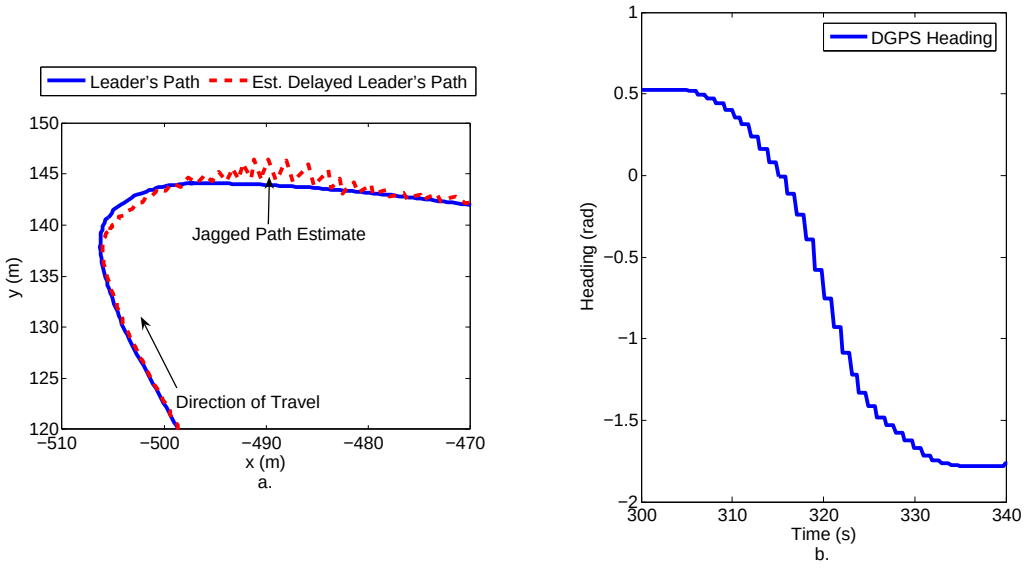

Figure 4.11: Path estimation with unfiltered DGPS heading: (a) Leader's path compared with estimated delayed leader's path during hairpin. (b) Follower's DGPS heading during hairpin.

4.4 May 25th–June 4th, 2009, Trials

After data was analyzed from the first set of trials, improvements were made to the decoupled controller and the MATS vehicle. The improvements include the following:

- Lateral gain scheduling
- Control laws with integral terms
- Adding the heading gyro
- Increasing the MATS vehicle's speed limit to 4.2 m/s

In addition, as given in Section 2.3.1, the look-ahead feature was changed to affect only the heading error, and the tracking error was redefined to be in the delayed leader's frame. Although we tried to anticipate the problems that would be encountered, e.g., road slope, camera offsets, and speed-dependent lateral poles, we still discovered challenges as trials were conducted.

4.4.1 Dealing with Side Slope

We have shown that adding integral terms to the decoupled control laws would help the follower overcome a constant side slope. However, the speed at which the follower overcomes the slope depends on the ratios between the lateral-controller gains, specifically, the ratios of the proportional heading-error gain to the proportional and integral lateral-error gains.

Recall the characteristic polynomial of the lateral closed-loop system, given in (2.18), is

$$s^3 + \frac{v_\mathrm{d}}{d} k_{\mathrm{p},3} s^2 + \frac{v_\mathrm{d}^2}{d} k_{\mathrm{p},2} s + \frac{v_\mathrm{d}^2}{d} k_{\mathrm{i},2}. \tag{4.1}$$

The strategy we used in simulation was to place the three poles at the same location on the negative real axis. Let p be that location; then, the resulting desired characteristic polynomial is

$$(s-p)^3 = s^3 - 3ps^2 + 3p^2 s - p^3. \tag{4.2}$$

Comparing 4.1 with 4.2, we get

$$\begin{aligned} k_{\mathrm{i},2} &= -d\frac{p^3}{v_\mathrm{d}^2} \\ k_{\mathrm{p},2} &= d\frac{3p^2}{v_\mathrm{d}^2} \\ k_{\mathrm{p},3} &= -d\frac{3p}{v_\mathrm{d}} \end{aligned}$$

and

$$\begin{aligned} \frac{k_{\mathrm{p},3}}{k_{\mathrm{p},2}} &= -\frac{v_\mathrm{d}}{p} \\ \frac{k_{\mathrm{p},3}}{k_{\mathrm{i},2}} &= \frac{3v_\mathrm{d}}{p^2}. \end{aligned}$$

Since, in implementation, $-0.26 < p < 0$ and usually $v_\mathrm{d} > 1$, we see that $k_{\mathrm{p},3}$ is typically

much larger than $k_{\mathrm{p},2}$ and $k_{\mathrm{i},2}$. Consequently, if there were a small lateral error but no heading error, the follower would take a while to overcome the lateral error since a large $k_{\mathrm{p},3}$ works to keep the heading error zero. This situation is exacerbated by a side slope, where wheel slip also works against correcting the lateral error. The follower will only eliminate the lateral error once the proportional and integral lateral-error terms are large enough to overcome heading-error term and the wheel slip caused by the slope. Hence, having larger $k_{\mathrm{p},2}$ and $k_{\mathrm{i},2}$ relative to $k_{\mathrm{p},3}$ is advantageous in dealing with a side slope.

The above gain discrepancies are not much better when using three distinct real poles as not all gains can be mapped by three real poles. However, the discrepancies can be made smaller by using a pair of complex poles. Without loss of generality, let the poles be a and $b \pm cj$. Then, the desired characteristic polynomial is

$$(s-a)(s-b+cj)(s-b-cj) = s^3 - (a+2b)s^2 + (2ab+b^2+c^2)s - a(b^2+c^2). \quad (4.3)$$

Comparing 4.1 with 4.3, we get

$$\begin{aligned} k_{\mathrm{i},2} &= -d\frac{a(b^2+c^2)}{v_{\mathrm{d}}^2} \\ k_{\mathrm{p},2} &= d\frac{2ab+b^2+c^2}{v_{\mathrm{d}}^2} \\ k_{\mathrm{p},3} &= -d\frac{a+2b}{v_{\mathrm{d}}} \end{aligned}$$

and

$$\begin{aligned} \frac{k_{\mathrm{p},3}}{k_{\mathrm{p},2}} &= -\frac{(a+2b)v_{\mathrm{d}}}{2ab+b^2+c^2} \\ \frac{k_{\mathrm{p},3}}{k_{\mathrm{i},2}} &= \frac{(a+2b)v_{\mathrm{d}}}{a(b^2+c^2)}. \end{aligned}$$

Thus, $\frac{k_{\mathrm{p},3}}{k_{\mathrm{p},2}}$ and $\frac{k_{\mathrm{p},3}}{k_{\mathrm{i},2}}$ can be reduced by increasing c, the imaginary part of the complex pole. Though a larger c helps with the speed at which the follower overcomes a side

slope, it may also lead to oscillatory steering behaviour.

Using the above approach, we were able to improve the follower's tracking ability in the presence of a side slope. In addition, we found that using complex poles also helped the follower reduce the longitudinal error to zero faster during startup since complex poles result in a larger longitudinal integral gain relative to the proportional gain. A larger integral gain was helpful because our longitudinal gains, in general, were quite small. Hence, our best experimental trials used complex longitudinal and lateral poles.

4.4.2 Constant Bearing Offset

During the trials, we also had problems with the follower veering to one side during startup. The main cause was eventually discovered to be the camera not being perfectly aligned or calibrated with the front of the vehicle as shown in Figure 4.12. Hence, there was a constant bearing offset, ϕ_o, between the actual bearing and measured bearing to the target. Consequently, the delayed leader's path estimate was off to one side, causing the follower to steer towards the incorrect path. Accounting for the constant bearing offset through simple calibration helped reduce the lateral error during startup.

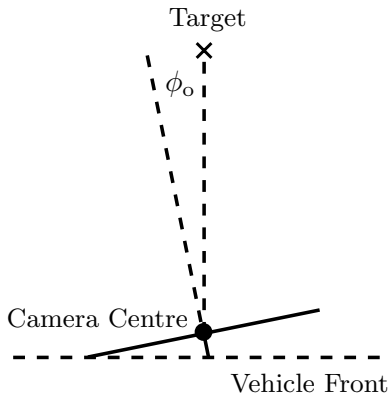

Figure 4.12: Camera off-aligned with front of vehicle leads to a constant bearing offset, ϕ_o, to the camera centre.

4.4.3 One Follower

Using only on-board sensors, we completed 10 laps of the test track with one follower for comparisons with the November 2008 trials. The parameters used for this test run are given in Table 4.4, and the results are shown in Table 4.5. With a mean speed of 2.8 m/s, the follower was able to track the leader with a lateral error of 0.12 ± 0.28 m and a maximum absolute lateral error of 1.32 m. Clearly, these results are much better than the results obtained using the first-version decoupled controller.

Table 4.4: Parameters for one-follower decoupled-controller trial using only on-board sensors.

Description	**Symbol**	**Value(s)**
Time delay	τ	6 s
Look-ahead time	l	2 s
Longitudinal pole locations		$-0.05 \pm 0.05j$
Lateral pole locations		-0.26, $-0.2 \pm 0.2j$

Figure 4.13 shows plots for a typical lap, which again highlights the improvement over the previous results shown in Figure 4.10. The follower no longer turns wide during the hairpin, and there is only a minimal increase in lateral errors during the U-turn and the hairpin compared with the rest of the path. The longitudinal error is also much better during these turns after the speed limit during sharp turns was removed. However, the longitudinal error still did not seem to go to zero. This is likely caused by

Table 4.5: Test results for 10 laps around 1.3 km test track with one follower using decoupled controller with only on-board sensors.

Description	**Symbol**	**Value**
Mean Follower Speed	v	2.8 m/s
Maximum Follower Speed	$\max_t v$	4.2 m/s
Minimum Following Distance		8.7 m
Mean Following Distance		17.1 m
Maximum Following Distance		23.8 m
Mean Lateral Error±Standard Deviation	$\frac{1}{t_\mathrm{f}} \int_0^{t_\mathrm{f}} \varepsilon_2(q) dq$	0.12 ± 0.28 m
Maximum Absolute Lateral Error	$\max_t \lvert\varepsilon_2(t)\rvert$	1.32 m

the low longitudinal gains and the constant range error with the camera, as mentioned in Section 3.2.

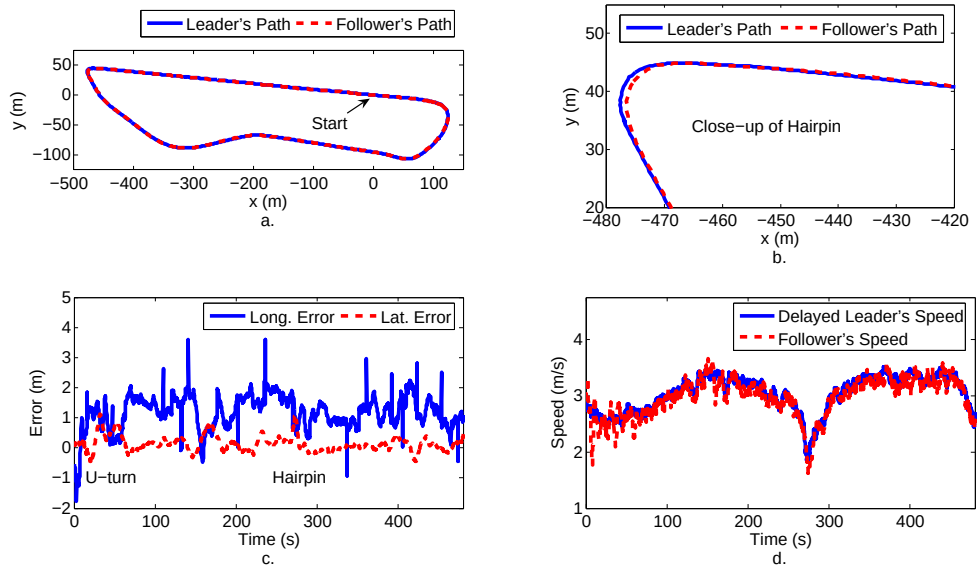

Figure 4.13: Typical lap for one follower using decoupled controller with only on-board sensors: (a) Leader's and follower's paths. (b) Close-up of hairpin turn. (c) Longitudinal and lateral tracking errors. (d) Delayed leader's and follower's speeds.

The estimated delayed leader's and follower's paths are shown in Figure 4.14, along with DGPS and gyro measurements of follower's heading. Not surprisingly, due to the unbounded error growth with dead reckoning, the estimated paths are not exactly the same as the real paths shown in Figure 4.13. As expected with using the magnetometer, the gyro's heading did not drift from the DGPS heading, which is shown in Figure 4.14d.

4.4.4 One Follower, Magnetometer Off

Magnetometers may be unreliable in the presence of electronic devices that locally disturb the earth's magnetic field [23]. Although our heading gyro with the magnetometer on did not suffer from reliability issues during the field trials, it would be preferable not to use the magnetometer at all. We were able to get our vehicle-following system to work with the magnetometer off with one of our two follower MATS vehicles. However, with

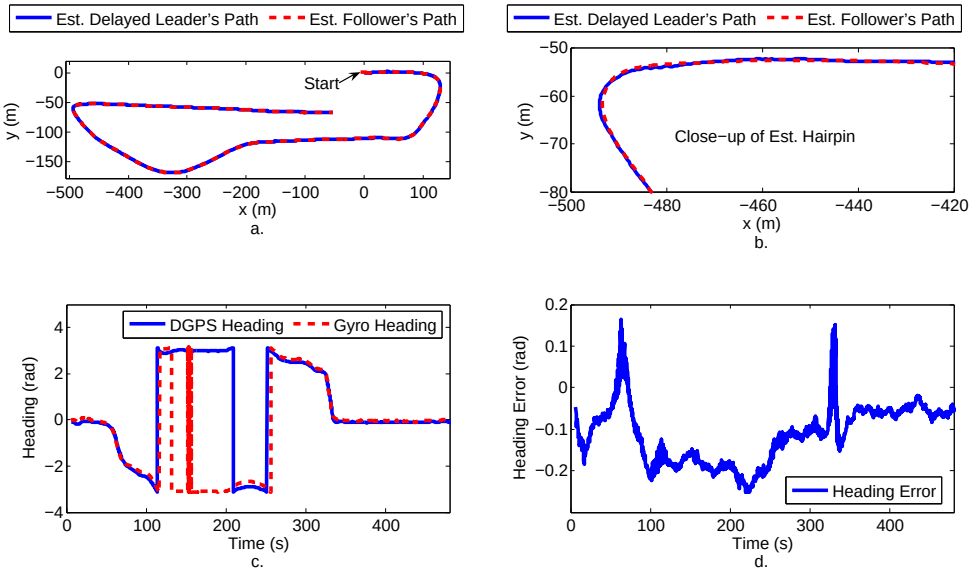

Figure 4.14: Typical lap for one follower using decoupled controller with only on-board sensors: (a) Estimated delayed leader's and follower's paths. (b) Close-up of hairpin turn. (c) DGPS and gyro measurements of follower's heading. (d) Heading error between DGPS and gyro. Note that the gyro heading does not drift from the DGPS heading as time increases.

the other follower, the heading measurement would rapidly drift while the vehicle was idling, causing the follower to veer off the road after its leader started moving. At this time, we are still unsure why the heading measurement would drift while idling in one follower, but not the other.

In an effort to reduce system failures due to dust, we reduced the time delay to 5 s to reduce the inter-vehicle distance. Because we still had the look-ahead time at 2 s, we had to reduce the smoother and line-fitting window sizes to 6 s. Using the parameters shown in Table 4.6, we completed 3 laps of the 1.3 km test track using one follower with its heading gyro's magnetometer off. The results, shown in Table 4.7, were essentially the same as the trial with the magnetometer on. The large mean lateral error can be attributed to not accounting for the camera's constant bearing offset.

Figure 4.15 shows plots for a typical lap of the magnetometer-off case, which again are very similar to the magnetometer-on case. The estimated delayed leader's and follower's paths are shown in Figure 4.16, along with DGPS and gyro measurements of follower's

Table 4.6: Parameters for one-follower decoupled-controller trial using only on-board sensors with magnetometer off.

Description	**Symbol**	**Value(s)**
Time delay	τ	5 s
Look-ahead time	l	2 s
Longitudinal pole locations		$-0.05 \pm 0.05j$
Lateral pole locations		-0.26, $-0.2 \pm 0.2j$

Table 4.7: Test results for 3 laps around 1.3 km test track with one follower using decoupled controller with only on-board sensors and magnetometer off.

Description	**Symbol**	**Value**
Mean Follower Speed	v	3.1 m/s
Maximum Follower Speed	$\max_t v$	4.1 m/s
Minimum Following Distance		5.5 m
Mean Following Distance		16.3 m
Maximum Following Distance		20.7 m
Mean Lateral Error±Standard Deviation	$\frac{1}{t_\mathrm{f}} \int_0^{t_\mathrm{f}} \varepsilon_2(q)dq$	0.23 ± 0.21 m
Maximum Absolute Lateral Error	$\max_t \lvert\varepsilon_2(t)\rvert$	0.96 m

heading. The estimated paths are a little worse than with the magnetometer on, which can be attributed to the gyro's heading drifting from the DGPS heading, as shown in Figure 4.16d.

4.4.5 One Follower, DGPS Localization with Filtered Heading

For comparison with using only on-board sensors, we conducted a trial run with one follower using DGPS to obtain the follower's position and heading. To prevent jagged delayed-leader path estimates around sharp turns, we filtered the DGPS heading with a Kalman filter. The parameters of Table 4.6 were also used for this trial, and the results are given in Table 4.8. As is evident from the large standard deviation in the lateral error and the large maximum absolute lateral error, our vehicle-following system works worse using DGPS than using only on-board sensors.

Figure 4.17 shows plots for a typical lap of the DGPS case, which highlights the poor

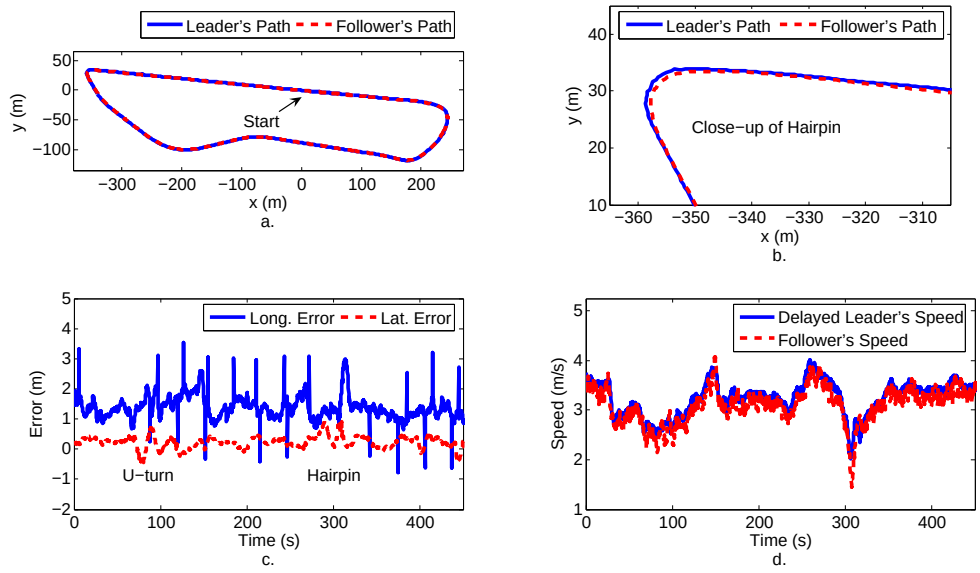

Figure 4.15: Typical lap for one follower using decoupled controller with only on-board sensors and magnetometer turned off: (a) Leader's and follower's paths. (b) Close-up of hairpin turn. (c) Longitudinal and lateral tracking errors. (d) Delayed leader's and follower's speeds.

performance. In Figure 4.17b, the follower can be seen going wide of the leader's path during the hairpin, resulting in a large lateral error shown in Figure 4.17c. The lateral errors are also quite large during the U-turn. The large lateral errors during these turns can be attributed to the lag in the DGPS heading. Although filtering smooths out the jagged heading during sharp turns, it only adds to the lag. This lag causes the delayed leader's path estimate to be wide of the leader's path, as shown in Figure 4.18a.

Table 4.8: Test results for 3 laps around 1.3 km test track with one follower using decoupled controller with on-board sensors and DGPS.

Description	**Symbol**	**Value**
Mean Follower Speed	v	3.0 m/s
Maximum Follower Speed	$\max_t v$	4.1 m/s
Minimum Following Distance		4.5 m
Mean Following Distance		15.5 m
Maximum Following Distance		20.3 m
Mean Lateral Error±Standard Deviation	$\frac{1}{t_f}\int_0^{t_f} \varepsilon_2(q)dq$	0.26 ± 0.45 m
Maximum Absolute Lateral Error	$\max_t \lvert\varepsilon_2(t)\rvert$	1.67 m

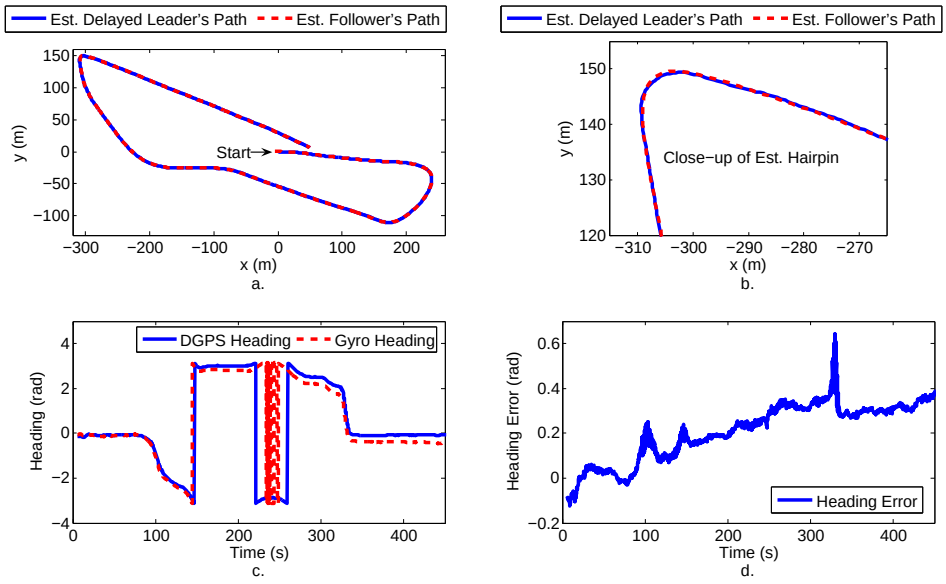

Figure 4.16: Typical lap for one follower using decoupled controller with only on-board sensors and magnetometer turned off: (a) Estimated delayed leader's and follower's paths. (b) Close-up of hairpin turn. (c) DGPS and gyro measurements of follower's heading. (d) Heading error between DGPS and gyro. Note that the gyro heading drifts from the DGPS heading as time increases.

4.4.6 Two Followers

The goal for our project was to conduct trials with two autonomous followers using only on-board sensors. We were able to accomplish this goal by completing over 13.5 laps of the test track with two followers. Both vehicles had their magnetometers on and used the parameters shown in Table 4.6. The results for the trial are shown in Table 4.9 and, not surprisingly, the lateral errors for follower 1 are very similar to the errors of the one-follower magnetometer-on case, shown in Table 4.5, (-0.02 ± 0.23 m with maximum absolute error of 1.13 m compared to 0.12 ± 0.28 m with maximum absolute error of 1.32 m). For follower 2, its lateral error with respect to the manually-driven lead vehicle was amplified to 0.24 ± 0.41 m. The large mean lateral error was mainly due to not properly accounting for the constant bearing offset. Although follower 2's maximum lateral error was also increased, the lateral error of 2.77 m is misleading because that occurred during startup, which we were still having difficulties with at the time when

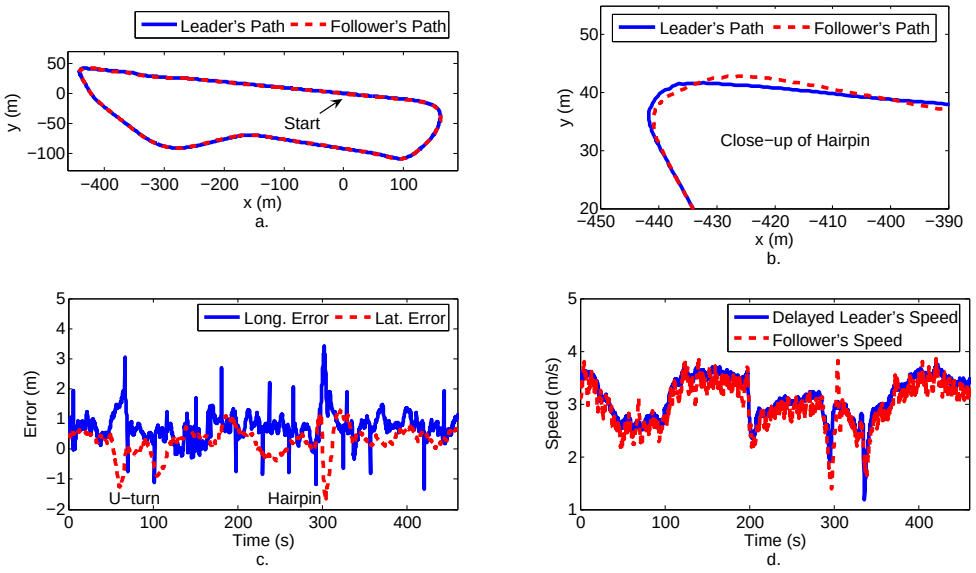

Figure 4.17: Typical lap for one follower using decoupled controller with on-board sensors and DGPS: (a) Leader's and follower's paths. (b) Close-up of hairpin turn. (c) Longitudinal and lateral tracking errors. (d) Delayed leader's and follower's speeds.

this trial was conducted. Follower 2's maximum lateral error after startup was around 2 m.

Figure 4.19 shows plots for a typical lap. Similar to one-follower trials, both followers did the hairpin quite well. In fact, the followers had more difficulty with the U-turn, as is evident from the lateral errors shown in Figure 4.19d. It is also evident that the lateral errors of follower 2 are amplified by the lateral errors of follower 1. However, for most of the 13.5-lap traverse, the lateral errors for both vehicles stayed within 1 m.

To fix the large mean lateral error for follower 2, we added an offset of 0.027 rad to its bearing measurements. We also added a bearing offset of 0.01 rad for follower 1 after more tuning to improve its startup. With this setup, we conducted another two-follower trial with the same parameters as before. Although the trial lasted only 1.5 laps before dust caused follower 2's camera to fail, the results, shown in Table 4.10, suggest the fix was successful since both vehicles' mean lateral errors are close to zero and the standard deviations are similar to the results shown in Table 4.9.

Table 4.9: Test results for 13.5 laps around 1.3 km test track with two followers using decoupled controller with only on-board sensors.

Description	**Symbol**	**Value**
Follower 1:		
Mean Follower Speed	v	2.8 m/s
Maximum Follower Speed	$\max_t v$	4.2 m/s
Minimum Following Distance		7.6 m
Mean Following Distance		14.2 m
Maximum Following Distance		19.3 m
Mean Lateral Error±Standard Deviation	$\frac{1}{t_\mathrm{f}} \int_0^{t_\mathrm{f}} \varepsilon_2(q)dq$	-0.02 ± 0.23 m
Maximum Absolute Lateral Error	$\max_t \lvert\varepsilon_2(t)\rvert$	1.13 m
Follower 2:		
Mean Follower Speed	v	2.7 m/s
Maximum Follower Speed	$\max_t v$	4.2 m/s
Minimum Following Distance		7.2 m
Mean Following Distance		14.1 m
Maximum Following Distance		19.6 m
Mean Lateral Error±Standard Deviation	$\frac{1}{t_\mathrm{f}} \int_0^{t_\mathrm{f}} \varepsilon_2(q)dq$	0.24 ± 0.41 m
Maximum Absolute Lateral Error	$\max_t \lvert\varepsilon_2(t)\rvert$	2.77 m

Table 4.10: Test results for 1.5 laps around 1.3 km test track with two followers using decoupled controller with only on-board sensors. Followers 1 and 2 had bearing offsets of 0.01 rad and 0.027 rad, respectively.

Description	**Symbol**	**Value**
Follower 1:		
Mean Follower Speed	v	2.8 m/s
Maximum Follower Speed	$\max_t v$	3.6 m/s
Minimum Following Distance		8.4 m
Mean Following Distance		14.3 m
Maximum Following Distance		18.1 m
Mean Lateral Error±Standard Deviation	$\frac{1}{t_\mathrm{f}} \int_0^{t_\mathrm{f}} \varepsilon_2(q)dq$	-0.07 ± 0.18 m
Maximum Absolute Lateral Error	$\max_t \lvert\varepsilon_2(t)\rvert$	0.84 m
Follower 2:		
Mean Follower Speed	v	2.6 m/s
Maximum Follower Speed	$\max_t v$	3.5 m/s
Minimum Following Distance		7.5 m
Mean Following Distance		13.6 m
Maximum Following Distance		17.1 m
Mean Lateral Error±Standard Deviation	$\frac{1}{t_\mathrm{f}} \int_0^{t_\mathrm{f}} \varepsilon_2(q)dq$	0.01 ± 0.34 m
Maximum Absolute Lateral Error	$\max_t \lvert\varepsilon_2(t)\rvert$	1.05 m

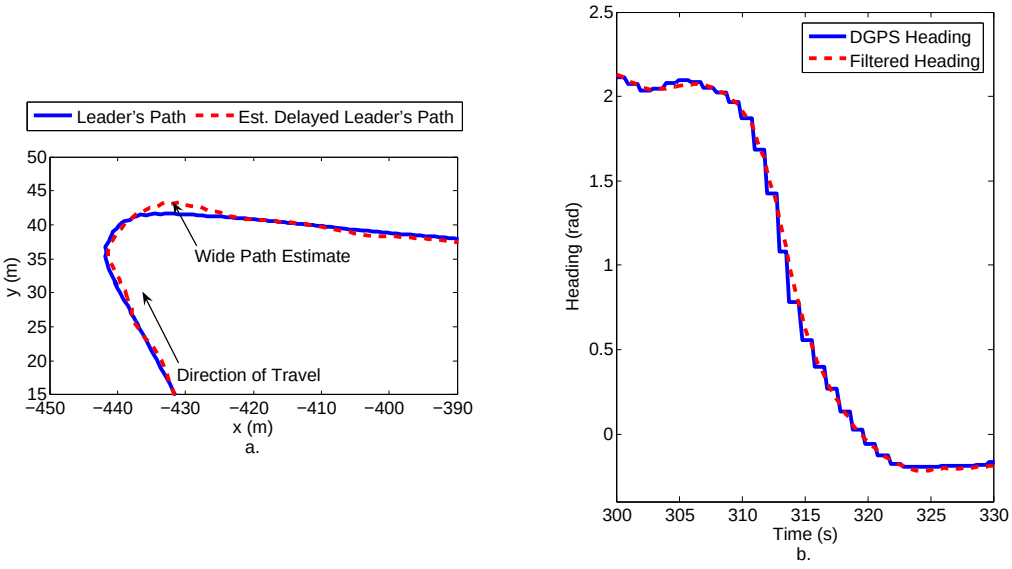

Figure 4.18: Path estimation with filtered DGPS heading: (a) Leader's path compared with estimated delayed leader's path during hairpin. (b) Follower's DGPS and filtered headings during hairpin.

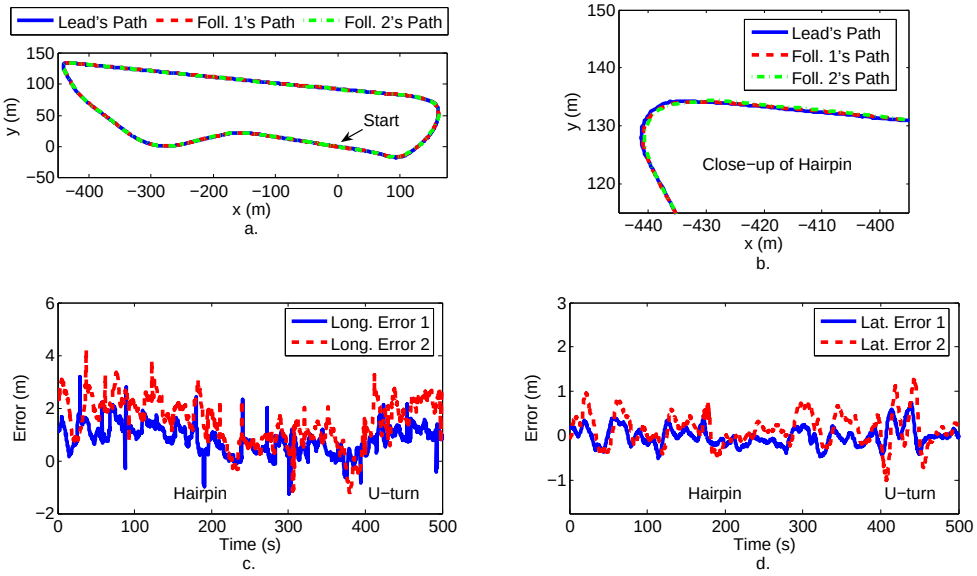

Figure 4.19: Typical lap for two followers using decoupled controller with only on-board sensors: (a) Lead's and followers' paths. (b) Close-up of hairpin turn. (c) Longitudinal tracking errors. (d) Lateral tracking errors.

Chapter 5

System Limitations

From the experiments, natural questions arise about the maximum speed and number of followers that our vehicle-following system can support. These questions include

- Using the experimental settings, how many followers can we have before one follower goes off the road?
- Ignoring camera limitations, how big would the lateral errors be for the current system if the lead vehicle were traveling at an operational speed (e.g., 25 m/s on straightaways and 8 m/s on turns)?
- What improvements can be made to the current system so that at least one follower can track at the operational speed without going off the road?

We explored these questions by performing more simulations in which we assumed the variances of the sensor noises were constant across the tested speeds and inter-vehicle distances. We again used the same noise-variance values shown in Table 3.3.

5.1 Maximum Number of Followers in Experimental Conditions

For the experiments, the followers were traveling at around 2 m/s on turns and up to 4.2 m/s on straightaways. To simulate these conditions, we conducted two simulation cases: one where the lead vehicle travels at a constant 2 m/s for 200 s, but makes a 90-degree left turn around the 100 s mark, and the other where the lead vehicle simply travels straight at 4.2 m/s for 200 s. Each case was repeated 30 times with nine followers and each follower used the same decoupled-controller parameter values as the ones used in most of the experiments, shown in Table 4.6.

Since the test track is about 7 m wide and the MATS vehicle is about 1.5 m wide, a lateral error of more than 2.75 m would mean that a follower is off the road. Using 2.75 m as the threshold, we examined the lateral errors for all the followers and recorded which follower was the first to exceed that threshold.

5.1.1 Results for Turn

Figure 5.1 shows a typical trial for the 90-degree-turn case. The lead vehicle's path, along with paths of the followers 4 and 8, is shown in Figure 5.1a. A close-up of the turn is shown in Figure 5.1b, and the lateral errors of followers 1, 4, and 8 are shown in Figure 5.1c. A histogram of the maximum number of followers before one exceeds 2.75 m in lateral error is shown in Figure 5.1d. The results suggest that at least five followers will be able to make a 90-degree turn without going off the road. As is evident from Figure 5.1e, the average maximum lateral error increases with the follower number.

5.1.2 Results for Straightaway

Figure 5.2 shows a typical trial for the straightaway case. The lead vehicle's path, along with paths of the followers 5 and 9, is shown in Figure 5.2a. A close-up of the paths

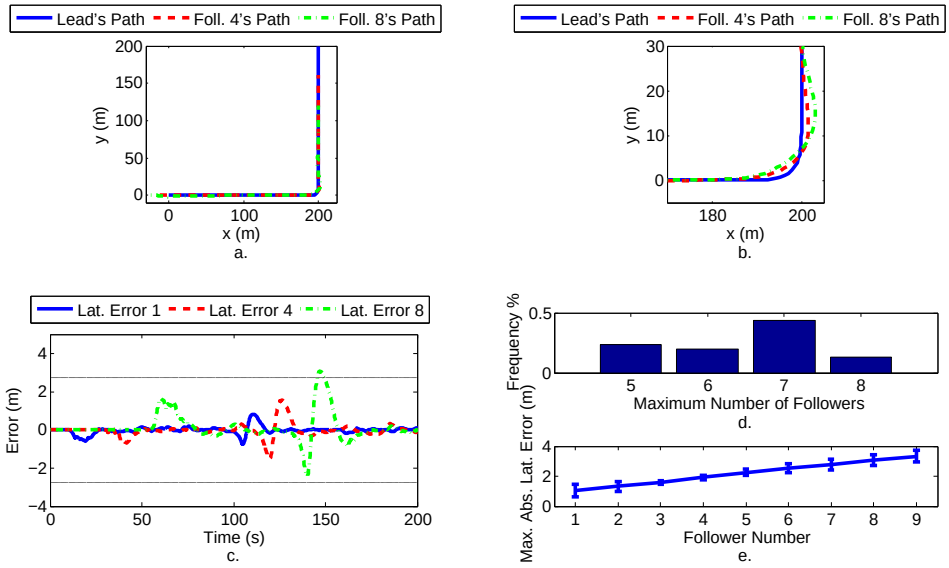

Figure 5.1: Typical trial for 90-degree-turn case at 2 m/s: (a) Paths for lead vehicle and followers 4 and 8. (b) Close-up of 90-degree left turn. (c) Lateral tracking errors for followers 1, 4, and 8. (d) Histogram of the maximum number of followers before one exceeds 2.75 m in lateral error. (e) Average maximum lateral error with one-standard-deviation error bars versus follower number.

is shown in Figure 5.2b, and the lateral errors of followers 1, 5, and 9 are shown in Figure 5.2c. A histogram of the maximum number of followers before one exceeds 2.75 m in lateral error is shown in Figure 5.2d. In nearly all of the trials, all nine followers were able to stay within the 2.75 m lateral-error threshold. Hence, the bottleneck for the experimental conditions is the 90-degree-turn case since less followers were able to make the turn before one goes off the road. Similar to Figure 5.1e, Figure 5.2e shows the average maximum lateral error increasing with the follower number, but the increase is not as large.

5.2 Current System Implementation Tested at an Operational Speed

We consider an operational speed for a convoy to be 25 m/s on straightaways and 8 m/s on turns. Using these objectives, we conducted two simulation test cases, similar to

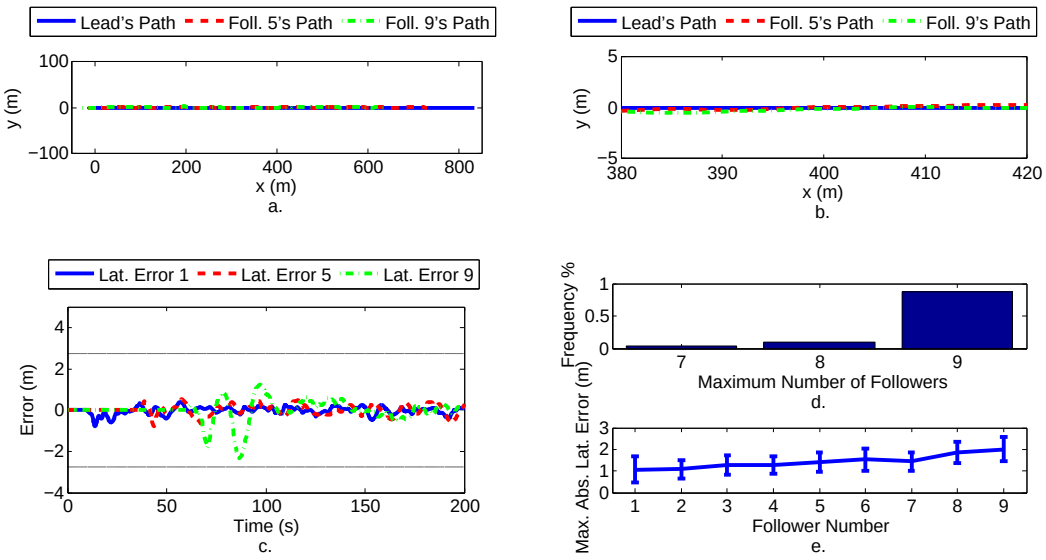

Figure 5.2: Typical trial for straightaway case at 4.2 m/s: (a) Paths for lead vehicle and followers 5 and 9. (b) Close-up of paths. (c) Lateral tracking errors for followers 1, 5, and 9. (d) Histogram of the maximum number of followers before one exceeds 2.75 m in lateral error. (e) Average maximum lateral error with one-standard-deviation error bars versus follower number.

Section 5.1, with two followers. In the first case, the lead vehicle makes the 90-degree left turn at a constant 8 m/s, while in the second case, the lead vehicle travels straight at a constant 25 m/s. Again, 30 trials were repeated for each case, and the maximum lateral errors for both followers are presented below.

5.2.1 Results for Turn

Figure 5.3 shows a typical trial for the 90-degree-turn case. As expected, the maximum lateral errors for both followers occurred during the turn. A close-up of the vehicle paths during the turn is shown in Figure 5.3b, and the lateral tracking errors for the trial is shown in Figure 5.3c. From these figures, it seems the followers are turning a little early (meaning the look-ahead time is too big) since the lateral errors are more negative than positive during the turn. Histograms of the maximum lateral errors for both followers are shown in Figure 5.3d and Figure 5.3e, respectively. Follower 1 averaged a maximum lateral error of 3.21 ± 0.33 m, and follower 2 averaged a maximum lateral

error of 5.15 ± 0.32 m. Clearly, with the current setup, both followers would not be able to make a 90-degree turn at 8 m/s without going off the road.

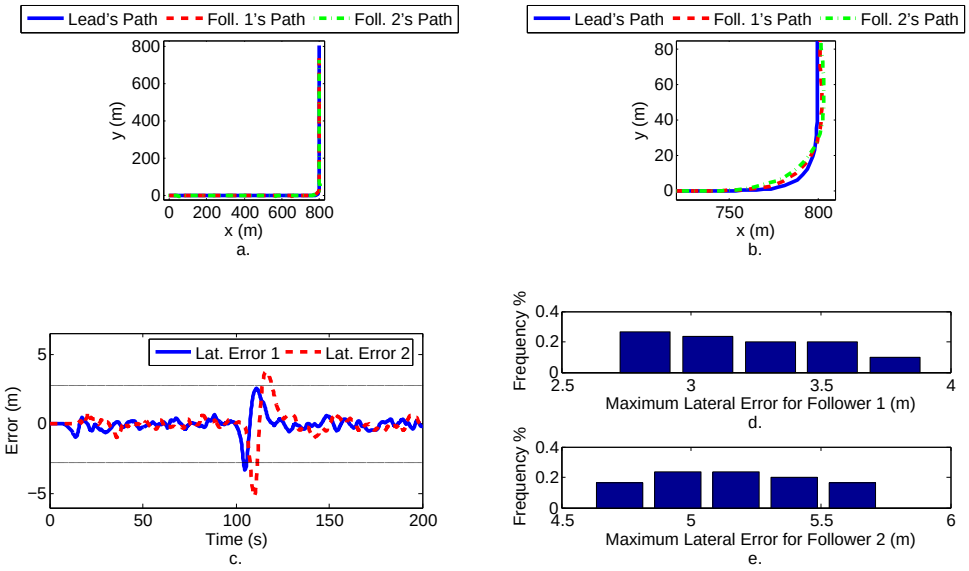

Figure 5.3: Typical trial for 90-degree-turn case at 8 m/s: (a) Paths for lead vehicle and followers 1 and 2. (b) Close-up of 90-degree left turn. (c) Lateral tracking errors for followers 1 and 2. (d) Histogram of maximum lateral errors for follower 1. (e) Histogram of maximum lateral errors for follower 2.

5.2.2 Results for Straightaway

Figure 5.4 shows a typical trial for the straightaway case. A close-up of the three vehicles' paths is shown in Figure 5.4b, and the lateral errors of both followers are shown in Figure 5.4c. Histograms of the maximum lateral errors for both followers are shown in Figure 5.4d and Figure 5.4e, respectively. Follower 1 averaged a maximum lateral error of 3.03 ± 0.53 m, and follower 2 averaged a maximum lateral error of 3.78 ± 0.55 m. Again, the lateral errors averaged greater than 2.75 m, but are smaller than the 90-degree-turn case.

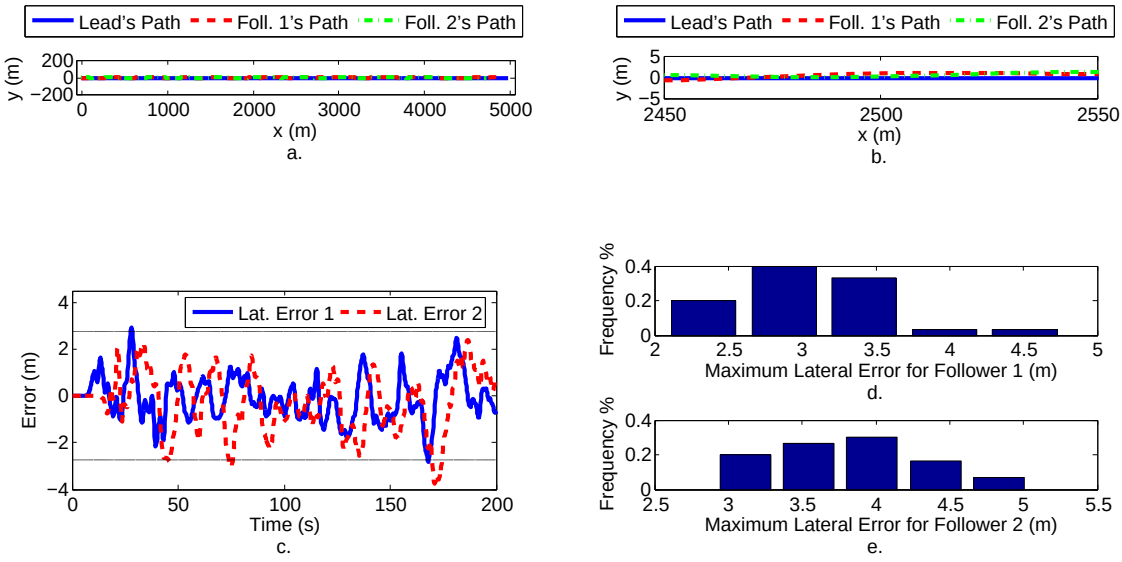

Figure 5.4: Typical trial for straightaway case at 25 m/s: (a) Paths for lead vehicle and followers 1 and 2. (b) Close-up of paths. (c) Lateral tracking errors for followers 1 and 2. (d) Histogram of maximum lateral errors for follower 1. (e) Histogram of maximum lateral errors for follower 2.

5.3 Improvements to Track at an Operational Speed

The main reason for our system's poor performance during high speeds seems to be the large heading gyro noise that is added to the simulations. This large noise creates poor path estimates that are exacerbated at high speeds because the inter-vehicle distance is increased. This is evident from the lateral errors of the followers in the two straightaway test cases above; with the same noise conditions, nearly all nine followers had lateral errors less than 2.75 m when the lead vehicle was going 4.2 m/s, but follower 1 and follower 2 had average maximum lateral errors larger than 2.75 m when the lead vehicle was going 25 m/s.

In an effort to reduce the inter-vehicle distance, the constant time delay can be reduced. However, a smaller time delay would require smaller smoother and line-fitting windows since the window sizes need to be less than twice the time delay. This is a problem with a system that runs at 4 Hz as smaller windows means fewer data points, thus increasing the possibility of bad estimates. An example is shown in Figure 5.5 where

the window sizes are all set to 2 s. As the result of having more data points, the heading estimates at 10 Hz are noticeably better than the estimates at 4 Hz under the same noise conditions. The heading errors at 10 Hz and 4 Hz have variances of 0.0011 rad^2 and 0.0029 rad^2, respectively.

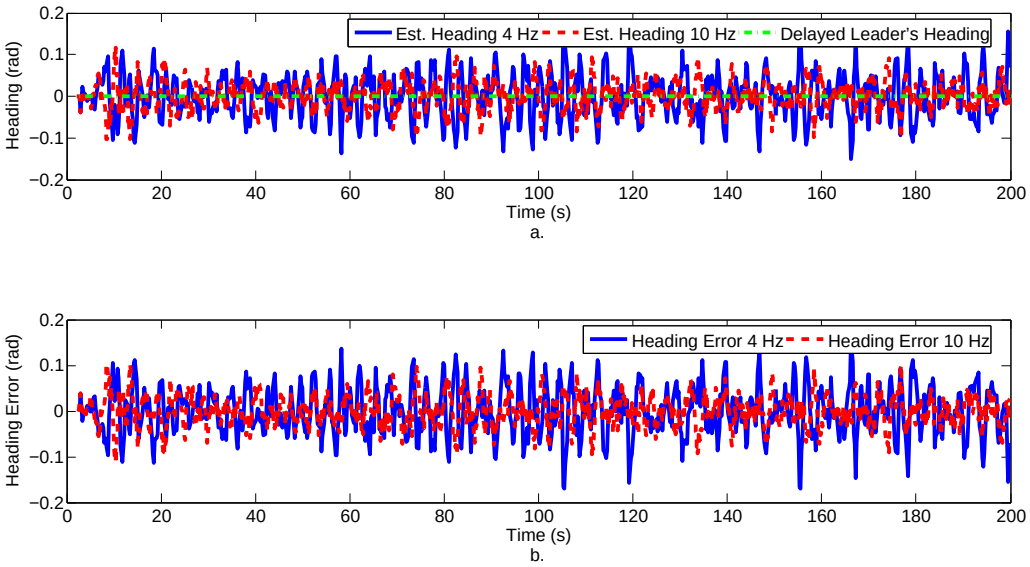

Figure 5.5: Heading estimates with window sizes all set to 2 s and the lead vehicle traveling straight at 25 m/s: (a) Heading estimates at 4 Hz and 10 Hz, along with the delayed leader's actual heading. (b) Errors in the heading estimates at 4 Hz and 10 Hz.

To get at least one follower to track consistently within a lateral error of 2.75 m at the operational speeds, we also had to reduce the variance of the simulated heading gyro noise to 0.0003 rad^2, a noise level with a 1-degree standard deviation. This noise level may be reasonable given that the stated accuracy for the heading gyro employed is 2 degrees [29]. In addition, we reduced the look-ahead time to 1.7 s as the followers seemed to be turning too early in Figure 5.3c. The specific changes that were made to the simulation to have at least one follower track at operation speeds are summarized below:

- Reduced the constant time delay, τ, from 5 s to 2.7 s.
- Reduced the look-ahead time, l, from 2 s to 1.7 s.
- Reduced the windowing sizes, n, from 6 s to 2 s.

- Reduced the heading gyro noise variance, σ_θ^2, from 0.0055 rad^2 to 0.0003 rad^2
- Increased the system operating rate, $\frac{1}{T}$, from 4 Hz to 10 Hz.

With the above setup, we again conducted 30 trials each of the straightaway and 90-degree-turn cases and recorded the maximum lateral errors for followers 1 and 2.

5.3.1 Results for Turn

Figure 5.6 shows a typical trial for the 90-degree-turn case. A close-up of the vehicle paths during the turn is shown in Figure 5.6b, and the lateral tracking errors for trial is shown in Figure 5.6c. Histograms of the maximum lateral errors for both followers are shown in Figure 5.6d and Figure 5.6e, respectively. Follower 1 averaged a maximum lateral error of 1.33 ± 0.08 m, and follower 2 averaged a maximum lateral error of 2.35 ± 0.10 m. Although both followers stayed within the 2.75 m threshold for all 30 trials, it is evident from the large increase in maximum lateral error from follower 1 to follower 2 that more improvements are required so that more followers can be added.

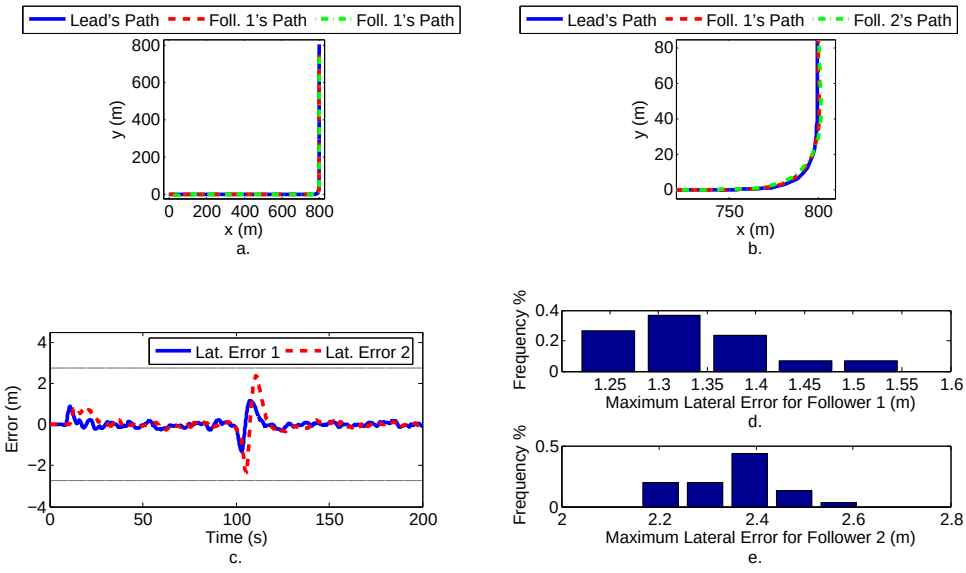

Figure 5.6: Typical trial for 90-degree-turn case at 8 m/s after improvements are made: (a) Paths for lead vehicle and followers 1 and 2. (b) Close-up of 90-degree left turn. (c) Lateral tracking errors for followers 1 and 2. (d) Histogram of maximum lateral errors for follower 1. (e) Histogram of maximum lateral errors for follower 2.

5.3.2 Results for Straightaway

Figure 5.7 shows a typical trial for the straightaway case. The lead vehicle's path, along with paths of the followers 1 and 2, is shown in Figure 5.7a. A close-up of the paths is shown in Figure 5.7b, and the lateral errors of both followers are shown in Figure 5.7c. Histograms of the maximum lateral errors for both followers are shown in Figure 5.7d and Figure 5.7e, respectively. Follower 1 averaged a maximum lateral error of 1.64 ± 0.68 m, and follower 2 averaged a maximum lateral error of 2.14 ± 0.81 m. Both followers had lateral errors greater than 2.75 m in 3 of the 30 trials. Again, these results supports the need for more improvements so that more followers can track successfully at an operational speed. These improvements are discuss in Section 6.1.

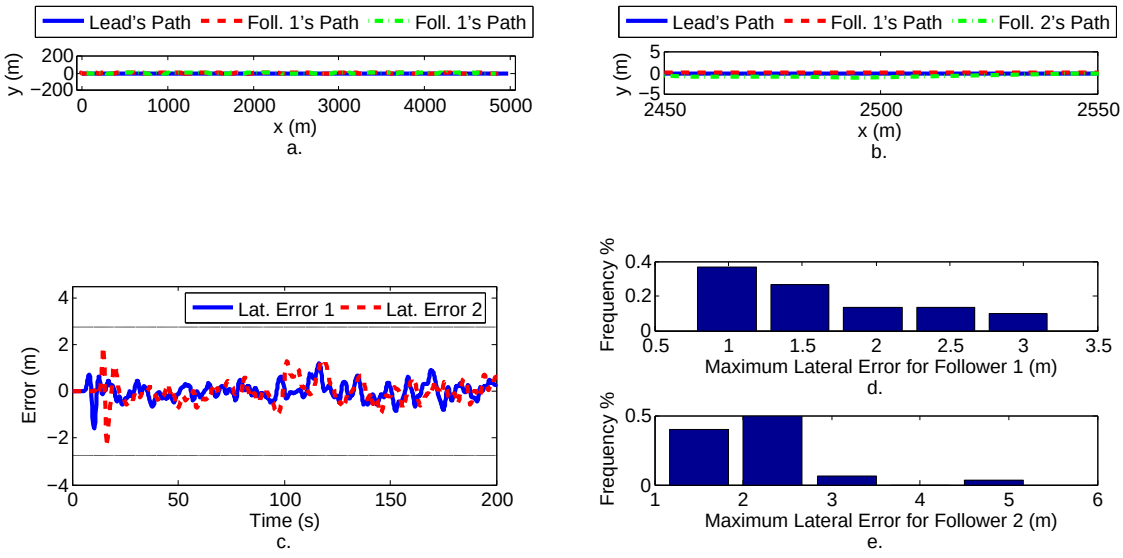

Figure 5.7: Typical trial for straightaway case at 25 m/s after improvements are made: (a) Paths for lead vehicle and followers 1 and 2. (b) Close-up of paths. (c) Lateral tracking errors for followers 1 and 2. (d) Histogram of maximum lateral errors for follower 1. (e) Histogram of maximum lateral errors for follower 2.

Chapter 6

Summary

This thesis details the design and experimental validation of a distributed vehicle-following system for vision-based convoying. The goal is to allow a convoy of full-sized autonomous vehicles with large inter-vehicle spacing to follow the lead vehicle's trajectory without cutting corners on turns. The vehicle-following system must also use only on-board sensors, avoiding the use of GPS, inter-vehicle communication, and road markers/magnets. The sensors include a pan/tilt/zoom camera to measure the range and bearing to the vehicle ahead, a gyro to measure the vehicle's heading, and wheel encoders to measure the vehicle's speed.

In the design, we took a novel approach to vehicle following by introducing the constant-time-delay concept. This approach creates a delayed leader and provides future delayed-leader camera measurements. These future measurements allow for the use of smoothers to estimate the range and bearing to the delayed leader and the use of line-fitting windows to estimate the delayed leader's speed and heading. In addition, vehicle following with a constant time delay causes the following distance to vary with the leader's speed. This means the following distance will be larger when the leader speeds up on easy portions of the road, e.g., paved roads and straightaways, and smaller when the leader slows down on difficult portions, e.g., rough terrain and turns. The smaller

following distance allows for more accurate camera measurements, which will help the tracking during those difficult portions.

To model a follower vehicle, we used the bicycle model and took advantage of the fact that our experimental vehicle had a speed-and-steering control system. As a result, we were able to treat the vehicle dynamics as unity gains and to design controllers based solely on the vehicle kinematics. With the objective of tracking a constant-velocity delayed leader, we designed two controllers: the point-ahead controller and the decoupled controller. The point-ahead controller proved difficult to tune since its speed and steering commands are coupled. The decoupled controller has decoupled speed and steering controls, allowing for more intuitive tuning and, as a result, worked much better than the point-ahead controller. Lateral gain scheduling and a look-ahead feature were also added to the decoupled controller to achieve better performance.

The inputs to the controllers are estimated by a nonlinear observer. The observer consists of dead reckoning to estimate the follower's position, smoothers to smooth the range and bearing measurements, and line-fitting windows to estimate the delayed leader's speed and heading. To test the performance of the nonlinear observer and controllers, a simulation environment was created in Simulink. The simulation environment consists of a manually-controlled lead vehicle and identical follower vehicles that autonomously track its immediate leader based on modeled sensor measurements. The vehicle kinematics were modeled using the bicycle model, while the dynamics were modeled with transfer functions fitted to experimental vehicle data. Experimental data was also used to model noise on the sensor measurements.

Experimental trials were conducted at the DRDC Suffield Experimental Proving Ground during November 17$^{\text{th}}$–28$^{\text{th}}$, 2008, and May 25$^{\text{th}}$–June 4$^{\text{th}}$, 2009. The first set of trials had to rely on DGPS for the follower's position and heading since the heading gyro had not yet been installed on the MATS vehicle. In addition, the decoupled controller was still in development and did not use lateral gain scheduling for these trials. The best

trial was a 10-lap traverse of the 1.3 km test track with one follower using the decoupled controller. In the trial, the follower averaged a speed of 2.2 m/s and a lateral error of 0.07 ± 0.46 m.

For the May/June 2009 trials, a heading gyro was added to the MATS vehicle, allowing the follower to better estimate its position. As a result, the follower was able to track the leader without DGPS. Trials were conducted around the test track with one and two followers with speeds of about 2.8 m/s. In the former, the follower averaged a lateral error of 0.12 ± 0.28 m over a 10-lap traverse of the test track, while in the latter, followers 1 and 2 averaged lateral errors of -0.02 ± 0.23 m and 0.24 ± 0.41 m, respectively, over a 13.5-lap traverse.

6.1 Future Work

There are many areas for future work in order to achieve autonomous convoying at operational speeds. As mentioned in Chapter 4, the camera system is susceptible to failure caused by dust or lighting changes. Hence, more testing is required to find a sensor to overcome these challenges. The work in [27] by Lv and Luo suggests radar may be the solution. We would also like the ability to tune each follower vehicle faster and to port the vehicle-following system across vehicles with different throttle and steering dynamics. The current process of running numerous trials to manually tune controller gains and adjust for camera misalignments is very time consuming. Developing an adaptive algorithm that can automatically adjust parameters during trials based on performance measures, such as tracking errors, should help the tuning process.

From Chapter 5, it is evident that our design has limitations at higher speeds in the presence of sensor noise. To obtain better path estimates, more research should be done to take advantage of the future delayed-leader data. Currently, we are tracking a point, the delayed leader, on a trajectory; perhaps, fitting a curve to the path and developing

a path tracker to take advantage of the future path will provide better performance. In addition, we currently do not employ a sophisticated method for outlier rejection. This task may be handled using methods like random sample consensus (RANSAC) [10] and iteratively reweighted least squares [31].

Other areas of development include adding obstacle avoidance and the ability to follow a 'missing' leader. With the constant-time-delay approach, there is a possibility that an object moves into the path previously occupied by a leader vehicle. This situation is shown in Figure 6.1 where the object is an oncoming vehicle. To avoid a collision, the follower must have the capability to detect the oncoming vehicle and diverge its path accordingly. A missing leader occurs when the leader goes out of sight for a large period of time, e.g., around a large building. This scenario would cause our current implementation to fail. Ideally, we would want the follower to move to the last known position of its leader and interpolate a new path if the leader is once again in view.

Figure 6.1: Oncoming vehicle may move into the path previously occupied by the leader vehicle.

Appendix A

Proof of a Necessary Condition for Tracking Delayed Leader using Dead Reckoning

One necessary condition for our design to work is that the uncertainty in the input to the controller must be bounded. This may not be obvious since the follower's position is estimated through dead reckoning. However, proofs of the uncertainty in both the point-ahead and decoupled controllers' inputs being bounded are given below. The proofs use the properties of complex numbers to simplify the computation.

A.1 Preliminaries

Recall bicycle kinematics for the follower vehicle:

$$\dot{x} = v\cos\theta$$

$$\dot{y} = v\sin\theta$$

$$\dot{\theta} = \frac{v}{d}\tan\gamma =: \omega,$$

where ω is the follower's turning rate.

Recall for a complex number

$$c = a + jb,$$

the magnitude of c is

$$|c| = \sqrt{a^2 + b^2}.$$

Also recall Euler's formula:

$$\mathrm{e}^{j\theta} = \cos\theta + j\sin\theta.$$

Thus,

$$\left|\mathrm{e}^{j\theta}\right| = 1.$$

A.2 Definitions

We define the space L_∞ of functions $u(t)$, $t \geq 0$, that are bounded. Thus, for each u in L_∞, there exists b such that for all $t \geq 0$, $|u(t)| \leq b$. Denote the least such b to be $\|u\|_\infty$, the L_∞-norm of u.

We also define the following sensor measurements using the common practice of assuming the measured signal is the actual signal plus additive noise:

- Measured follower speed by the wheel encoders:

$$v_m(t) := v(t) + n_{\mathrm{v}}(t), \tag{A.1}$$

  where $n_{\mathrm{v}}(t)$ is noise, and similarly for the 'n' terms to follow.

- Measured follower turning rate by the heading gyro:

$$\omega_m(t) := \omega(t) + n_\omega(t).$$

- Measured range to leader from camera:

$$\rho_m(t) := \rho(t) + n_\rho(t). \tag{A.2}$$

- Measured bearing to leader from camera:

$$\phi_m(t) := \phi(t) + n_\phi(t).$$

The follower's heading is estimated by the gyro through integrating the turning rate:

$$\hat{\theta}(t) = \int_0^t \omega_m(q)\, dq.$$

For simplicity, we assume the delayed leader's estimated heading is a nonlinear function f representing the effects the nonlinear observer:

$$\hat{\theta}_{\mathrm{d}}(t) = f(\dots).$$

Finally, we define the follower's position as

$$z := x + jy.$$

Hence,

$$\begin{aligned}
\dot{z} &= \dot{x} + j\dot{y} \\
&= v(\cos\theta + j\sin\theta) \\
&= v\mathrm{e}^{j\theta}.
\end{aligned}$$

Based on the follower's position definition and the vehicle kinematics, the follower's

position can be calculated as

$$z(t) = \int_0^t v(q)\mathrm{e}^{j\theta(q)}\,dq. \tag{A.3}$$

Using the speed and turning rate measurements, we estimate the follower's position as

$$\hat{z}(t) = \int_0^t v_m(q)\mathrm{e}^{j\hat{\theta}(q)}\,dq. \tag{A.4}$$

From geometry, the delayed leader's position can be calculated as

$$z_\mathrm{d}(t) = z(t-\tau) + \rho(t-\tau)\mathrm{e}^{j\phi(t-\tau)}\mathrm{e}^{j\theta(t-\tau)}. \tag{A.5}$$

Using the range and bearing measurements, we estimate the delayed leader's position as

$$\hat{z}_\mathrm{d}(t) = \hat{z}(t-\tau) + \rho_m(t-\tau)\mathrm{e}^{j\phi_m(t-\tau)}\mathrm{e}^{j\hat{\theta}(t-\tau)}. \tag{A.6}$$

A.3 Proof for Point-ahead Controller

The input into the point-ahead controller is the difference between the estimated points ahead, $\hat{\mathbf{p}}_\mathrm{d} - \hat{\mathbf{p}}$. As a complex number, the follower's actual point ahead is

$$p(t) = z(t) + \kappa r(t), \tag{A.7}$$

where $r(t) = \mathrm{e}^{j\theta(t)}$ is complex equivalent of the unit heading vector. Similarly, the follower's estimated point ahead is

$$\hat{p}(t) = \hat{z}(t) + \kappa \hat{r}(t), \tag{A.8}$$

where $\hat{r}(t) = \mathrm{e}^{j\hat{\theta}(t)}$. For the delayed leader, its actual point ahead is

$$p_{\mathrm{d}}(t) = z_{\mathrm{d}}(t) + \kappa r_{\mathrm{d}}(t), \tag{A.9}$$

where $r_{\mathrm{d}}(t) = \mathrm{e}^{j\theta_{\mathrm{d}}(t)}$, and its estimated point ahead is

$$\hat{p}_{\mathrm{d}}(t) = \hat{z}_{\mathrm{d}}(t) + \kappa \hat{r}_{\mathrm{d}}(t), \tag{A.10}$$

where $\hat{r}_{\mathrm{d}}(t) = \mathrm{e}^{j\hat{\theta}_{\mathrm{d}}(t)}$. Defining

$$\epsilon(t) := p_{\mathrm{d}}(t) - p(t)$$

and

$$\hat{\epsilon}(t) := \hat{p}_{\mathrm{d}}(t) - \hat{p}(t),$$

we let

$$\delta_{\epsilon}(t) := \left|\epsilon(t) - \hat{\epsilon}(t)\right|.$$

Thus, to show that the uncertainty in the input to the point-ahead controller is bounded, we need to show that $\delta_{\epsilon}(t)$ is bounded. This is proven in Theorem 1, but to assist in the proof, we introduce two lemmas:

Lemma 1. *If v and ρ belong to L_∞, so does ϵ and, moreover, $\|\epsilon\|_\infty \leq \tau \|v\|_\infty + \|\rho\|_\infty + 2\kappa$.*

Proof. We have for any t

$$
\begin{aligned}
|\epsilon(t)| &= |z_{\mathrm{d}}(t) + \kappa r_{\mathrm{d}}(t) - z(t) - \kappa r(t)| && \text{by (A.7), (A.9)} \\
&\leq |z_{\mathrm{d}}(t) - z(t)| + \kappa \, |r_{\mathrm{d}}(t) - r(t)| \\
&= \left|z(t-\tau) + \rho(t-\tau)\mathrm{e}^{j\phi(t-\tau)}\mathrm{e}^{j\theta(t-\tau)} - z(t)\right| + \kappa \left|\mathrm{e}^{j\theta_{\mathrm{d}}(t)} - \mathrm{e}^{j\theta(t)}\right| && \text{by (A.5)} \\
&\leq \left|-\int_{t-\tau}^{t} v(q)\mathrm{e}^{j\theta(q)}\, dq + \rho(t-\tau)\right| + \kappa \left(\left|\mathrm{e}^{j\theta_{\mathrm{d}}(t)}\right| + \left|\mathrm{e}^{j\theta(t)}\right|\right) && \text{by (A.3)} \\
&\leq \left|\int_{t-\tau}^{t} v(q)\mathrm{e}^{j\theta(q)}\, dq\right| + \left|\rho(t-\tau)\mathrm{e}^{j\phi(t-\tau)}\mathrm{e}^{j\theta(t-\tau)}\right| + 2\kappa \\
&= \left|\int_{t-\tau}^{t} v(q)\mathrm{e}^{j\theta(q)}\, dq\right| + |\rho(t-\tau)| + 2\kappa \\
&\leq \int_{t-\tau}^{t} \left|v(q)\mathrm{e}^{j\theta(q)}\right| \, dq + |\rho(t-\tau)| + 2\kappa \\
&= \int_{t-\tau}^{t} |v(q)| \, dq + |\rho(t-\tau)| + 2\kappa \\
&\leq \tau \|v\|_\infty + \|\rho\|_\infty + 2\kappa && \text{by } L_\infty \text{ assum.}
\end{aligned}
$$

Since the right-hand side is independent of t,

$$\|\epsilon\|_\infty \leq \tau \|v\|_\infty + \|\rho\|_\infty + 2\kappa.$$

□

Lemma 2. *If v, n_{v}, ρ, and n_ρ belong to L_∞, so does $\hat{\epsilon}$ and, moreover, $\|\hat{\epsilon}\|_\infty \leq \tau \|v\|_\infty + \tau \|n_{\mathrm{v}}\|_\infty + \|\rho\|_\infty + \|n_\rho\|_\infty + 2\kappa$.*

Proof. We have for any t

$$
\begin{aligned}
|\hat{\epsilon}(t)| &= |(\hat{z}_{\mathrm{d}}(t) + \kappa \hat{r}_{\mathrm{d}}(t) - \hat{z}(t)) - \kappa \hat{r}(t)| && \text{by (A.8), (A.10)} \\
&\leq |\hat{z}_{\mathrm{d}}(t) - \hat{z}(t)| + \kappa \, |\hat{r}_{\mathrm{d}}(t) - \hat{r}(t)| \\
&= \left| \hat{z}(t-\tau) + \rho_m(t-\tau) \mathrm{e}^{j\phi_m(t-\tau)} \mathrm{e}^{j\hat{\theta}(t-\tau)} - \hat{z}(t) \right| + \kappa \left| \mathrm{e}^{j\hat{\theta}_{\mathrm{d}}(t)} - \mathrm{e}^{j\hat{\theta}(t)} \right| && \text{by (A.6)} \\
&\leq \left| - \int_{t-\tau}^{t} v_m(q) \mathrm{e}^{j\hat{\theta}(q)} \, dq + \rho_m(t-\tau) \right| + \kappa \left(\left| \mathrm{e}^{j\hat{\theta}_{\mathrm{d}}(t)} \right| + \left| \mathrm{e}^{j\hat{\theta}(t)} \right| \right) && \text{by (A.4)} \\
&\leq \left| \int_{t-\tau}^{t} v_m(q) \mathrm{e}^{j\hat{\theta}(q)} \, dq \right| + |\rho_m(t-\tau)| + 2\kappa \\
&\leq \int_{t-\tau}^{t} \left| v_m(q) \mathrm{e}^{j\hat{\theta}(q)} \right| \, dq + |\rho(t-\tau) + n_\rho(t-\tau)| + 2\kappa && \text{by (A.2)} \\
&\leq \int_{t-\tau}^{t} |v_m(q)| \, dq + |\rho(t-\tau)| + |n_\rho(t-\tau)| + 2\kappa \\
&= \int_{t-\tau}^{t} |v(q) + n_{\mathrm{v}}(q)| \, dq + |\rho(t-\tau)| + |n_\rho(t-\tau)| + 2\kappa && \text{by (A.1)} \\
&\leq \int_{t-\tau}^{t} |v(q)| \, dq + \int_{t-\tau}^{t} |n_{\mathrm{v}}(q)| \, dq + |\rho(t-\tau)| + |n_\rho(t-\tau)| + 2\kappa \\
&\leq \tau \|v\|_\infty + \tau \|n_{\mathrm{v}}\|_\infty + \|\rho\|_\infty + \|n_\rho\|_\infty + 2\kappa && \text{by } L_\infty \text{ assum.}
\end{aligned}
$$

Since the right-hand side is independent of t,

$$\|\hat{\epsilon}\|_\infty \leq \tau \|v\|_\infty + \tau \|n_{\mathrm{v}}\|_\infty + \|\rho\|_\infty + \|n_\rho\|_\infty + 2\kappa.$$

□

Theorem 1. *If v, n_{v}, ρ, and n_ρ belong to L_∞, so does δ_ϵ and, moreover, $\|\delta_\epsilon\|_\infty \leq 2\tau \|v\|_\infty + \tau \|n_{\mathrm{v}}\|_\infty + 2 \|\rho\|_\infty + \|n_\rho\|_\infty + 4\kappa$.*

Proof. We have for any t

$$\begin{aligned}
\delta_\epsilon(t) &= |\varepsilon(t) - \hat{\varepsilon}(t)| \\
&\leq |\varepsilon(t)| + |\hat{\varepsilon}(t)| \\
&\leq \|\varepsilon\|_\infty + \|\hat{\varepsilon}\|_\infty && \text{by } L_\infty \text{ assum.} \\
&\leq 2\tau \|v\|_\infty + \tau \|n_{\mathrm{v}}\|_\infty + 2 \|\rho\|_\infty + \|n_\rho\|_\infty + 4\kappa && \text{by Lemmas 1 and 2}
\end{aligned}$$

Since the right-hand side is independent of t,

$$\|\delta_\epsilon\|_\infty \leq 2\tau \|v\|_\infty + \tau \|n_{\mathrm{v}}\|_\infty + 2 \|\rho\|_\infty + \|n_\rho\|_\infty + 4\kappa.$$

□

As proven by Theorem 1, if the follower's speed, range to the leader, and noises on the speed and range measurements are bounded (which are reasonable assumptions), then the uncertainty in the input into the point-ahead controller is bounded.

A.4 Proof for Decoupled Controller

The input into the decoupled controller is the estimated tracking error in the delayed leader's frame. As a complex number, the actual tracking error in the delayed leader's frame is

$$\varepsilon(t) = (z_{\mathrm{d}}(t) - z(t))\mathrm{e}^{-j\theta_{\mathrm{d}}(t)}.$$

Similarly, the estimated tracking error in the delayed leader's frame, as a complex number, is

$$\hat{\varepsilon}(t) = (\hat{z}_{\mathrm{d}}(t) - \hat{z}(t))\mathrm{e}^{-j\hat{\theta}_{\mathrm{d}}(t)}.$$

Define the difference as

$$\delta_\varepsilon(t) := |\varepsilon(t) - \hat{\varepsilon}(t)| .$$

Thus, to show that the uncertainty in the input to the decoupled controller is bounded, we need to show that $\delta_\varepsilon(t)$ is bounded. This is proven in Theorem 2, but to assist in the proof, we introduce two lemmas:

Lemma 3. *If v and ρ belong to L_∞, then so does ε and, moreover, $\|\varepsilon\|_\infty \leq \tau \|v\|_\infty + \|\rho\|_\infty$.*

Proof. We have for any t

$$\begin{aligned} |\varepsilon(t)| &= \left|(z_{\mathrm{d}}(t) - z(t))\mathrm{e}^{-j\theta_{\mathrm{d}}(t)}\right| \\ &= |z_{\mathrm{d}}(t) - z(t)| \\ &\leq \tau \|v\|_\infty + \|\rho\|_\infty && \text{by Lemma 1} \end{aligned}$$

Since the right-hand side is independent of t,

$$\|\varepsilon\|_\infty \leq \tau \|v\|_\infty + \|\rho\|_\infty .$$

□

Lemma 4. *If v, n_{v}, ρ, and n_ρ belong to L_∞, so does $\hat{\varepsilon}$ and, moreover, $\|\hat{\varepsilon}\|_\infty \leq \tau \|v\|_\infty + \tau \|n_{\mathrm{v}}\|_\infty + \|\rho\|_\infty + \|n_\rho\|_\infty$.*

Proof. We have any t

$$\begin{aligned} |\hat{\varepsilon}(t)| &= \left|(\hat{z}_{\mathrm{d}}(t) - \hat{z}(t))\mathrm{e}^{-j\hat{\theta}_{\mathrm{d}}(t)}\right| \\ &= |\hat{z}_{\mathrm{d}}(t) - \hat{z}(t)| \\ &\leq \tau \|v\|_\infty + \tau \|n_{\mathrm{v}}\|_\infty + \|\rho\|_\infty + \|n_\rho\|_\infty && \text{by Lemma 2} \end{aligned}$$

Since the right-hand side is independent of t,

$$\|\hat{\varepsilon}\|_\infty \leq \tau \|v\|_\infty + \tau \|n_\mathrm{v}\|_\infty + \|\rho\|_\infty + \|n_\rho\|_\infty .$$

□

Theorem 2. *If v, n_v, ρ, and n_ρ belong to L_∞, so does δ_ε, and, moreover, $\|\delta_\varepsilon\|_\infty \leq 2\tau \|v\|_\infty + \tau \|n_\mathrm{v}\|_\infty + 2 \|\rho\|_\infty + \|n_\rho\|_\infty$.*

Proof. We have for any t

$$\begin{aligned}
\delta_\varepsilon(t) &= |\varepsilon(t) - \hat{\varepsilon}(t)| \\
&\leq |\varepsilon(t)| + |\hat{\varepsilon}(t)| \\
&\leq \|\varepsilon\|_\infty + \|\hat{\varepsilon}\|_\infty && \text{by } L_\infty \text{ assum.} \\
&\leq 2\tau \|v\|_\infty + \tau \|n_\mathrm{v}\|_\infty + 2 \|\rho\|_\infty + \|n_\rho\|_\infty && \text{by Lemmas 3 and 4}
\end{aligned}$$

Since the right-hand side is independent of t,

$$\|\delta_\varepsilon\|_\infty \leq 2\tau \|v\|_\infty + \tau \|n_\mathrm{v}\|_\infty + 2 \|\rho\|_\infty + \|n_\rho\|_\infty .$$

□

As proven by Theorem 2, if the follower's speed, range to the leader, and noises on the speed and range measurements are bounded (which are reasonable assumptions), then the uncertainty in the input into the decoupled controller is bounded.

Appendix B

Glossary

Constant time delay The time delay in seconds used to define a leader's delayed position, which is the reference point for its autonomous follower.

Dead reckoning The process of integrating sensor measurements using the vehicle kinematics to estimate a follower's position.

Decoupled controller The controller designed by linearizing the vehicle model about a constant-velocity trajectory, thus decoupling the model into longitudinal and lateral components.

Delayed leader A leader delayed by the constant time delay; the delayed leader is the reference vehicle for an autonomous follower.

Follower An autonomous vehicle that tracks the delayed position of the vehicle ahead of it.

Future delayed-leader positions Leader positions that are ahead in time of the current delayed-leader position.

Ground truth A vehicle's actual position, heading, and speed. In our field trials, we treated the DGPS measurements as ground truth.

Lead vehicle The manually-driven first vehicle of a convoy.

Leader Any vehicle in a convoy that has an autonomous follower; the leader may be autonomous itself or be the manually-driven first vehicle of the convoy.

Line-fitting window A method used to fit a line to a window of delayed-leader positions; the slope of the line is used estimate the delayed leader's speed and heading.

Localization The process of obtaining position and heading estimates relative to some reference point.

Nonlinear observer In our vehicle-following system, the nonlinear observer consists of dead reckoning to estimate the follower's position, smoothers to estimate range and bearing measurements, and line-fitting windows to estimate the delayed leader's speed and heading.

Point-ahead controller The controller designed by linearizing the vehicle model about a point ahead.

Smoother A method using cubic splines to smooth a window of range or bearing measurements.

Bibliography

[1] P. Avanzini, E. Royer, B. Thuilot, and P. Martinet. A Global Decentralized Control Strategy for Urban Vehicle Platooning using Monocular Vision and a Laser Rangefinder. In *International Conference on Control, Automation, Robotics and Vision*, pages 291–296, 2008.

[2] S. Benhimane, E. Malis, P. Rives, and J. R. Azinheira. Vision-based Control for Car Platooning using Homography Decomposition. In *Proceedings of the IEEE International Conference on Robotics and Automation*, pages 2161–2166, 2005.

[3] J. Bom, B. Thuilot, F. Marmoiton, and P. Martinet. A Global Control Strategy for Urban Vehicles Platooning Relying on Nonlinear Decoupling Laws. In *IEEE/RSJ International Conference on Intelligent Robots and Systems*, pages 2875–2880, 2005.

[4] J. Bom, B. Thuilot, F. Marmoiton, and P. Martinet. Nonlinear Control for Urban Vehicles Platooning, Relying upon a Unique Kinematic GPS. In *Proceedings of the IEEE International Conference on Robotics and Automation*, pages 4138–4143, 2005.

[5] J. Borenstein. Internal Correction of Dead-Reckoning Errors With a Dual-Drive Compliant Linkage Mobile Robot. *Journal of Robotic Systems*, 12(4):257–273, 1995.

[6] C. Constable and R. Parker. Deconvolution of Long-Core Palaeomagnetic Measurements–Spline Therapy for the Linear Problem. *Geophysical Journal International*, 104(3):453–468, 1991.

[7] P. Daviet and M. Parent. Platooning for Small Public Urban Vehicles. In *International Symposium on Experimental Robotics*, pages 345–354, 1995.

[8] P. Daviet and M. Parent. Longitudinal and Lateral Servoing of Vehicles in a Platoon. In *Proceedings of the IEEE Intelligent Vehicles Symposium*, pages 41–46, 1996.

[9] J. Davis, A. Animashaun, E. Schoenherr, and K. McDowell. Evaluation of Semi-Autonomous Convoy Driving. *Journal of Field Robotics*, 25(11–12):880–897, 2008.

[10] M. A. Fischler and R. C. Bolles. Random Sample Consensus: A Paradigm for Model Fitting with Applications to Image Analysis and Automated Cartography. *Communications of the ACM*, 24(6):381–395, 1981.

[11] B. A. Francis. Distributed Control of Autonomous Mobile Robots. ECE1635 Course Notes, 2007. Electrical and Computer Engineering Department, University of Toronto.

[12] U. Franke, F. Bottiger, Z. Zomotor, and D. Seeberger. Truck Platooning in Mixed Traffic. In *Proceedings of the Intelligent Vehicles Symposium*, pages 1–6, 1995.

[13] H. Fritz. Longitudinal and Lateral Control of Heavy Duty Trucks for Automated Vehicle Following in Mixed Traffic: Experimental Results from the CHAUFFEUR Project. In *Proceedings of the IEEE International Conference on Control Applications*, volume 2, pages 1348–1352, 1999.

[14] S. K. Gehrig and F. J. Stein. A Trajectory-based Approach for the Lateral Control of Car Following Systems. In *IEEE International Conference on Systems, Man, and Cybernetics*, volume 4, pages 3596–3601, 1998.

[15] J. L. Giesbrecht. A Pan/Tilt/Zoom Tracking System for Unmanned Ground Vehicles. Master's thesis, University of Calgary, 2008.

[16] J. L. Giesbrecht, H. K. Goi, T. D. Barfoot, and B. A. Francis. A Vision-based Robotic Follower Vehicle. In *Proceedings of the SPIE Unmanned Systems Technology XI*, volume 7332, 2009.

[17] N. C. Griswold, N. D. Kehtarnavaz, and K. M. Miller. A Transportable Neural Network Controller for Autonomous Vehicle Following. In *Proceedings of the Intelligent Vehicles Symposium*, pages 195–200, 1994.

[18] J. J. Jaczkowski. Robotic Follower Experimentation Results: Ready for FCS Increment I. In *Proceedings of the SPIE Unmanned Ground Vehicle Technology V*, volume 5083, pages 311–321, 2003.

[19] S. Kato, S. Tsugawa, K. Tokuda, T. Matsui, and H. Fujii. Vehicle Control Algorithms for Cooperative Driving with Automated Vehicles and Intervehicle Communications. *IEEE Transactions on Intelligent Transportation Systems*, 3(3):155–161, 2002.

[20] N. Kehtarnavaz, N. Griswold, K. Miller, and P. Lescoe. A Transportable Neural-Network Approach to Autonomous Vehicle Following. *IEEE Transactions on Vehiculuar Technology*, 47(2):694–702, 1998.

[21] N. Kehtarnavaz, N. C. Griswold, and J. S. Lee. Visual Control of an Autonomous Vehicle (BART)—The Vehicle-Following Problem. *IEEE Transactions on Vehicular Technology*, 40(3):654–662, 1991.

[22] N. Kehtarnavaz, E. Nakamura, N. Griswold, and J. Yen. Autonomous Vehicle Following by a Fuzzy Logic Controller. In *Proceedings of the First International Joint Conference of the North American Fuzzy Information Processing Society Biannual Conference*, pages 333–337, 1994.

[23] M. Kourogi and T. Kurata. Personal Positioning based on Walking Locomotion Analysis with Self-Contained Sensors and a Wearable Camera. In *Proceedings of the*

Second IEEE and ACM International Symposium on Mixed and Augmented Reality, pages 103–112, 2003.

[24] P. Lancaster and K. Salkauskas. *Curve and Surface Fitting: An Introduction*. Academic Press, San Diego, 1986.

[25] G. Lu and M. Tomizuka. A Laser Scanning Radar Based Autonomous Lateral Vehicle Following Control Scheme for Automated Highways. In *Proceedings of the American Control Conference*, volume 1, pages 30–35, 2003.

[26] G. Lu and M. Tomizuka. A Practical Solution to the String Stability Problem in Autonomous Vehicle Following. In *Proceedings of the American Control Conference*, volume 1, pages 780–785, 2004.

[27] J. Lv and J. Luo. Millimeter-Wave Radar Application in Tracking Maneuvering Target. In *International Conference on Radar*, pages 1–4, 2006.

[28] J. Marshall, T. Barfoot, and J. Larsson. Autonomous Underground Tramming for Center-Articulated Vehicles. *Journal of Field Robotics*, 25(6–7):400–421, 2008.

[29] MicroStrain, 310 Hurricane Lane, Unit 4. Williston, Vermont, USA. *Detailed Specifications for 3DM-GX1*, August 2009.

[30] T. C. Ng, J. Ibanez-Guzman, and M. D. Adams. Autonomous Vehicle-Following Systems: A Virtual Trailer Link Model. In *IEEE/RSJ International Conference on Intelligent Robots and Systems*, pages 3057–3062, 2005.

[31] D. P. O'Leary. Robust Regression Computation using Iteratively Reweighted Least Squares. *SIAM Journal on Matrix Analysis and Applications*, 11(3):466–480, 1981.

[32] I. Papadimitriou, G. Lu, and M. Tomizuka. Autonomous Lateral Following Considerations for Vehicle Platoons. In *Proceedings of the IEEE/ASME International Conference on Advanced Intelligent Mechatronics*, volume 1, pages 401–406, 2003.

[33] H. Schneiderman, M. Nashman, and R. Lumia. Model-based Vision for Car Following. In *Proceedings of SPIE Conference on Sensor Fusion VI*, volume 2059, pages 420–431, 1993.

[34] H. Schneiderman, M. Nashman, A. J. Wavering, and R. Lumia. Vision-based Robotic Convoy Driving. *Machine Vision and Applications*, 8(6):359–364, 1995.

[35] R. Sukthankar. RACCOON: A Real-time Autonomous Car Chaser Operating Optimally at Night. In *Proceedings of the IEEE Intelligent Vehicles Symposium*, pages 37–42, 1993.

[36] D. Swaroop and J. K. Hedrick. Constant Spacing Strategies for Platooning in Automated Highway Systems. *Journal of Dynamic Systems, Measurement, and Control*, 121(3):462–470, 1999.

[37] D. Swaroop and K. R. Rajagopal. A Review of Constant Time Headway Policy for Automatic Vehicle Following. In *Proceedings of the IEEE Intelligent Transportation Systems*, pages 65–69, 2001.

[38] H. Tan, R. Rajamani, and W. Zhang. Demonstration of an Automated Highway Platoon System. In *Proceedings of the American Control Conference*, volume 3, pages 1823–1827, 1998.

[39] N. A. Teanby. Constrained Smoothing of Noisy Data using Splines in Tension. *Mathematical Geology*, 39(4):419–434, 2007.

[40] C. Thorpe, T. Jochem, and D. Pomerleau. The 1997 Automated Highway Free Agent Demonstration. In *IEEE Conference on Intelligent Transportation System*, pages 496–501, 1997.

[41] B. Thuilot, J. Bom, F. Marmoiton, and P. Martinet. Accurate Automatic Guidance of an Urban Electric Vehicle Relying on a Kinematic GPS Sensor. In *IFAC/EURON Symposium on Intelligent Autonomous Vehicles*, 2004.

[42] L. Vasseur, O. Lecointe, J. Dento, N. Cherfaoui, V. Marion, and J. G. Morillon. Leader-Follower Function for Autonomous Military Convoys. In *Proceedings of SPIE Unmanned Ground Vehicle Technology VI*, volume 5422, pages 326–337, 2004.

[43] D. Wang, M. Pham, C. B. Low, and C. Tan. Development and Implementation of a Fault-Tolerant Vehicle-Following Controller for a Four-Wheel-Steering Vehicle. In *IEEE/RSJ International Conference on Intelligent Robots and Systems*, pages 13–18, 2006.

[44] M. G. Wing, A. Eklund, and L. D. Kellogg. Consumer-Grade Global Positioning System (GPS) Accuracy and Reliability. *Journal of Forestry*, 105(4):169–173, 2005.